THE UNIVERSITY OF CHICAGO

A SEARCH FOR PRIMORDIAL BLACK HOLES AND A STUDY OF SPECTRAL VARIATION IN MARKARIAN 421 USING THE WHIPPLE 10-M TELESCOPE

A DISSERTATION SUBMITTED TO
THE FACULTY OF THE DIVISION OF THE PHYSICAL SCIENCES
IN CANDIDACY FOR THE DEGREE OF
DOCTOR OF PHILOSOPHY

DEPARTMENT OF PHYSICS

BY
ERIC T. LINTON

CHICAGO, ILLINOIS
MARCH 2006

TABLE OF CONTENTS

LIST OF FIGURES

LIST OF TABLES

ACKNOWLEDGMENTS

First I would like to thank my advisor, Simon Swordy, for helping me to grow into a much better scientist during my time here. I would also like to thank the other members of my thesis committee: Dietrich Mueller, Philippe Guyot-Sionnest, and Sav Sethi for their suggestions which have made this a stronger thesis. Thanks as well to all the memebers of the VERITAS collaboration for their help along the way — in particular to Jo Jo, who showed me the ropes when I first started here, and to Brian, who has helped me keep my sanity down the home stretch.

Sandy Heinz and Nobuko McNeill have my thanks for helping me through all the paper work and other red tape that I never would have survived otherwise. I am also indebted to Valeri Galtsev for fixing hydra every time I broke it.

In addition, I want to acknowledge all my friends who have helped me to keep a smile on my face despite exams, psychotic computers, and the sun setting at 4:30 in the afternoon. In particular, I am thankful for my friends at Hyde Park Alliance Church and the Graduate Christian Fellowship for helping me not to forget what is really important; the guys on the rugby team for teaching me what is perhaps the most beautiful game on earth; and the members of the Prime Number of the Day Club for helping me take the first baby steps toward realizing my oft scoffed at dream of providing free prime numbers for every man, woman, and child on earth.

Finally, I would like to thanks the people who have been the greatest support to me in graduate school — my family. Brian and John, you have been the best brothers anyone could hope for. Jenn, you only joined the family recently, but I am glad that you did. Mom and Dad, I will always be in debt to you for being such great role models and teaching me what is most important in life. Thanks be to God for guiding me through this entire experience (Phil. 4:13).

For my parents

ABSTRACT

The development of ground based atmospheric Čerenkov telescopes has opened up astronomy to the world of TeV photons and allowed for the study of a wide range of high energy physical processes. In this work two different examples are explored. The first is a search through 5.5 years of archival data from the Whipple 10-m telescope for TeV gamma-ray bursts on 1-s, 3-s, and 5-s timescales. The motivation for this search is that such a signal might be expected from the evaporation of primordial black holes (PBHs) in the local region of our galaxy. Based on a null result from this direct search for PBH evaporations, an upper limit of 1.08×10^6 pc^{-3} yr^{-1} (99% CL) on the evaporation rate is set, assuming the Standard Model of particle physics. This is more than a factor of two better than the previous limit at this energy range and includes longer time scales than have previously been explored.

The second topic covered in this work is a study of TeV observations of the blazar Markarian 421 made by the Whipple 10-m telescope during its 2003-2004 season. This work is the first to study this full data set. One result has been to confirm that the relationship between spectral shape and flux for month-scale flares is stable over the period of years. However, for data averaged over sub-month scales, this relationship fails to fit the data, indicating that a different mechanism is responsible for flares on the shorter time scales. Another interesting fact to come from this study is that, given the most recent constraints on the extra galactic background light, absorption by this photon field is insufficient to completely account for the cutoff observed in the spectrum of Markarian 421 at a few TeV. This finding provides further support for an intrinsic cause for this cutoff.

CHAPTER 1

INTRODUCTION

The field of TeV gamma-ray astronomy is relatively young, having taken off with the introduction of the imaging technique which allowed for the detection of the Crab Nebula in 1989 (1). Since then the number of sources has steadily been increasing. With the development of multiple telescope arrays, such as VERITAS and HESS, the rate of new source discovery and scientific advancement has increased dramatically.

One of the attractions in this field of study is that TeV energies are not easily achievable, meaning that any sources of such energetic photons must be employing some truly interesting mechanisms. Despite the strict energy requirements, there is a relatively large variety of sources. They range from well established sources with masses estimated to be about 10^8 times that of the sun to hypothetical sources with a mass that is only a small fraction of the earth's. Through this wide range of sources, many interesting areas of physics can be studied.

This thesis begins in chapter 2 with an overview of the basic equipment and analysis techniques used in TeV gamma-ray astronomy. In particular, it describes the Whipple 10-m telescope which is the source of the data used in this work. Chapter 3 discusses a search for primordial black holes which has resulted in a new upper limit on their local evaporation rate. Finally, measurements of the energy spectrum of the blazar Markarian 421 and their implications are covered in chapter 4.

CHAPTER 2

TEV GAMMA-RAY ASTRONOMY

2.1 The Imaging Atmospheric Čerenkov Technique

The motivation for ground-based gamma-ray telescopes derives from the fact that the higher one goes in energy, the smaller the flux of photons. Typically, sources have a spectrum that is steeper than a power law with index 2.0, which implies a decrease by a factor of over $1,000$ in flux for a ten-fold increase in energy. Satellite experiments, such as EGRET (2), have proven successful at probing the MeV to GeV gamma-ray sky, but to go higher in energy would require detectors with much larger surface areas in order to detect the much smaller flux of particles. Such an endeavor would be very costly for an experiment meant to be launched into space, but can be done relatively cheaply on the ground.

The opacity of the earth's atmosphere to gamma rays is one of the reasons satellites were initially used for gamma-ray astronomy. Although at first glance this might seem to be a decided disadvantage for doing TeV gamma-ray astronomy from the ground, it has been utilized to be one of the greatest strengths of this field. The fact that gamma rays interact in the atmosphere has allowed astronomers to use the atmosphere itself as the detector, thus allowing for instruments with very large collection areas.

When a gamma-ray enters the atmosphere it will interact via pair production to create an electron-positron pair. These particles will in turn produce more photons through bremsstrahlung, which can again pair-produce, starting an electromagnetic cascade. Many of the electrons and positrons created in this process will be traveling fast enough to produce Čerenkov light, which can then be detected by telescopes on the ground. Since a detector anywhere within the Čerenkov light pool has the potential to detect the event, the collection area for such experiments is determined by the size of the light pools rather than the physical size of the detectors (Fig. 2.1). Ground-based telescopes typically have collection areas on the order of 10^4 m^2 as compared to satellite experiments, which are limited to areas of about 1 m^2.

The primary background for these atmospheric Čerenkov telescopes (ACTs) are cosmic rays, which also produce Čerenkov flashes on the same timescale as those initiated by gamma rays. However, hadron-initiated showers tend not to be as clean as the photon showers due to the production of pions that create sub-showers. This fact has been successfully exploited to discriminate between cosmic rays and gamma rays, as will be discussed below in section 2.4.

2.2 The Whipple 10-m Telescope

The Whipple 10-m telescope, located in southern Arizona at an elevation of 2, 300 m, has been used for gamma-ray astronomy since 1968 (Fig. 2.2). It has a 10 m diameter reflector consisting of 249 identical, spherical mirrors each with a focal length of 7.3 m. These mirrors are arranged on a spherical support structure with a radius of curvature of 7.3 m. This design, known as the Davies-Cotton design (3), is used for several reasons. First, the production of many relatively small mirrors is much easier, and consequently cheaper, than the production of a single large mirror. The off-axis aberrations are also less than with a parabolic design. The major disadvantage of this approach is that the arrival time of photons in the focal plane can vary by up to 6 ns. Thus, while the optical quality of the images is not affected, some of the timing information is lost.

While the mirror design has remained largely unchanged over the history of the telescope, the camera has undergone a considerable evolution. This work covers two

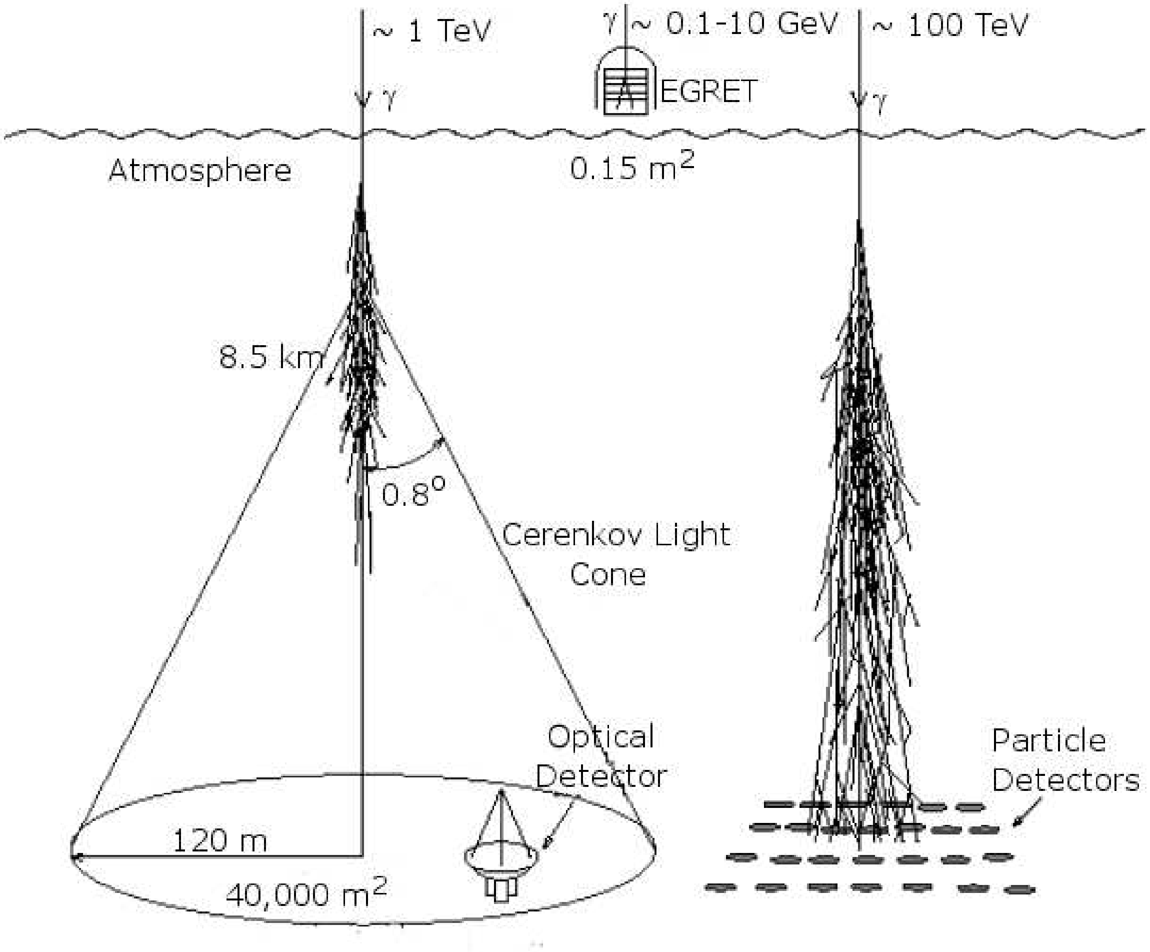

Figure 2.1 In the atmospheric Čerenkov technique, the atmosphere itself is used as the detector, so the size of the Čerenkov light pool on the ground determines the experiment's collection area. Thus, ground-based telescopes have collection areas on the order of 10^4 m^2 as opposed to satellite experiments which are limited in size to about 1 m^2. Higher energy events in which the shower particles themselves are able to reach the ground are best measured using particle detector arrays, as illustrated on the right.

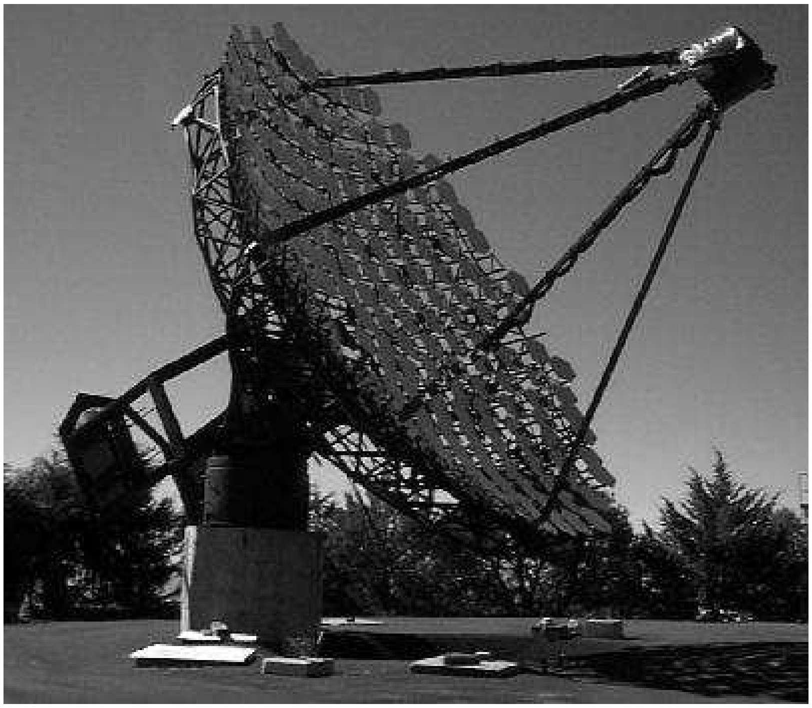

Figure 2.2 The Whipple 10-m telescope, located on Mt. Hopkins at the Whipple Observatory in southern Arizona.

different camera configurations. The first was installed in 1997 and consisted of 331 photomultiplier tubes (PMTs) with an inter-tube spacing of 0.25°. The total field of view (FOV) of this camera was 4.8°. In the summer of 1999, a new camera was installed that was composed of 379 PMTs with an inter-tube spacing of 0.12°. This gave it a finer angular resolution at the expense of reducing the FOV to about 2.3°.

Before 1999, the camera was triggered if any three of the PMTs had a signal ≥ 65 photoelectrons within an effective resolving time of 8 ns. In 1999 a more sophisticated triggering system, known as the pattern selection trigger, was installed (4). This upgraded system requires the three PMTs contributing to the trigger to be adjacent to one another. By reducing the number of triggers from night-sky noise, the pattern trigger allows the camera to be run at the lower trigger threshold of about 7 photoelectrons while still keeping the count rate at a manageable level of about 20 Hz. The lower trigger threshold effectively lowers the energy threshold of the telescope.

2.3 Observations

Due to the faintness of the Čerenkov flashes that we wish to observe, the telescope can only be run at night when the moon is not in the sky. The duty cycle is further reduced by the heavy rains that come during the summers in southern Arizona. Consequently, no observations are made for about two months every year. This time is used to perform maintenance and make upgrades on the telescope.

Observations with the Whipple telescope are typically made with a source zenith angle less than 35°. Data are taken in two modes of observation: ON/OFF and TRACKING. In the ON/OFF mode a source is tracked continuously for 28 minutes and then a region offset in right ascension by 30 minutes is tracked in order to obtain a sample of background data covering the same region of the sky, in terms of azimuth and elevation, as the on-source data. In TRACKING mode the background is estimated from the on-source data itself, removing the need for off-source data and thereby increasing the on-source time at the expense of increasing the systematic uncertainty (see section 2.4).

Before and during observations, two different types of calibration data are taken. At the beginning of each night, a one-minute run using a fast Optitron nitrogen arc lamp to uniformly illuminate the camera is taken to facilitate the calculation of the relative gains of the PMTs. In addition, the camera is artificially triggered during each run at a rate of about 1 Hz. This allows for the measurement of the output of each PMT with no input signal present, which is also known as the "pedestal."

2.4 Data Analysis

Data analysis proceeds in several stages, which will be described in more detail below. If the data were taken in ON/OFF mode, it first undergoes a process of "padding" to make sure the on-source and off-source data are well matched. Then the image is cleaned in order to remove pixels that are likely to be the result of night-sky noise. Finally, various parameters are fit to each shower image and compared to predetermined selection criteria in order to select those showers which are most likely to have been initiated by gamma-ray primaries.

For data taken in ON/OFF mode, a bias can be introduced in the analysis if one of the fields is considerably brighter than the other because it, for instance, contains more stars. This effect is compensated for by a process known as software padding in which noise is added to the data in the less noisy field (5). On a PMT by PMT basis, the variance in the pedestal values are compared and noise is added to the less noisy PMT signal to compensate for the difference.

Image cleaning is done using two different trigger levels that are set relative to the standard deviation in the pedestal values for each PMT. The higher level, referred to as the "picture" level, is set at 4.25 times the pedestal standard deviation, and the lower level, referred to as the "boundary" level, is set at 2.25 times the pedestal standard deviation. In order for the signal from a PMT to be included in a particular image it must either be above the picture threshold, or be adjacent to a PMT that is above the picture threshold and itself be above the boundary threshold.

Once the images have been padded and cleaned, they are ready to be separated into gamma-ray-like events and non-gamma-ray-like events. The most commonly used technique for gamma-ray selection utilizes the fact that the images in the camera produced by gamma-ray showers are compact ellipses, while hadron showers tend to produce larger, messier images. Therefore, an ellipse is fit to each shower image by calculating the zeroth, first, and second moments of each and using these moments to compute various other parameters related to that ellipse (6). These parameters are summarized in table 2.1 and depicted schematically in Fig. 2.3.

Table 2.1 A summary of some of the most commonly used fit parameters in gamma-ray selection.

Parameter	**Description**
Width	The RMS spread of light along the minor axis of the image.
Length	The RMS spread of light along the major axis of the image.
Distance	The distance from the image centroid to the center of the FOV.
α	The angle between the major axis of the ellipse and a line joining the centroid of the ellipse to the center of the FOV.
Size	The sum of the digital counts from all PMTs contributing to the image.
MaxN	The number of digital counts in the N^{th} brightest PMT.

The *Width* and *Length* parameters both relate directly to the angular spread of the image in the focal plane, and so are useful for selecting the more compact images

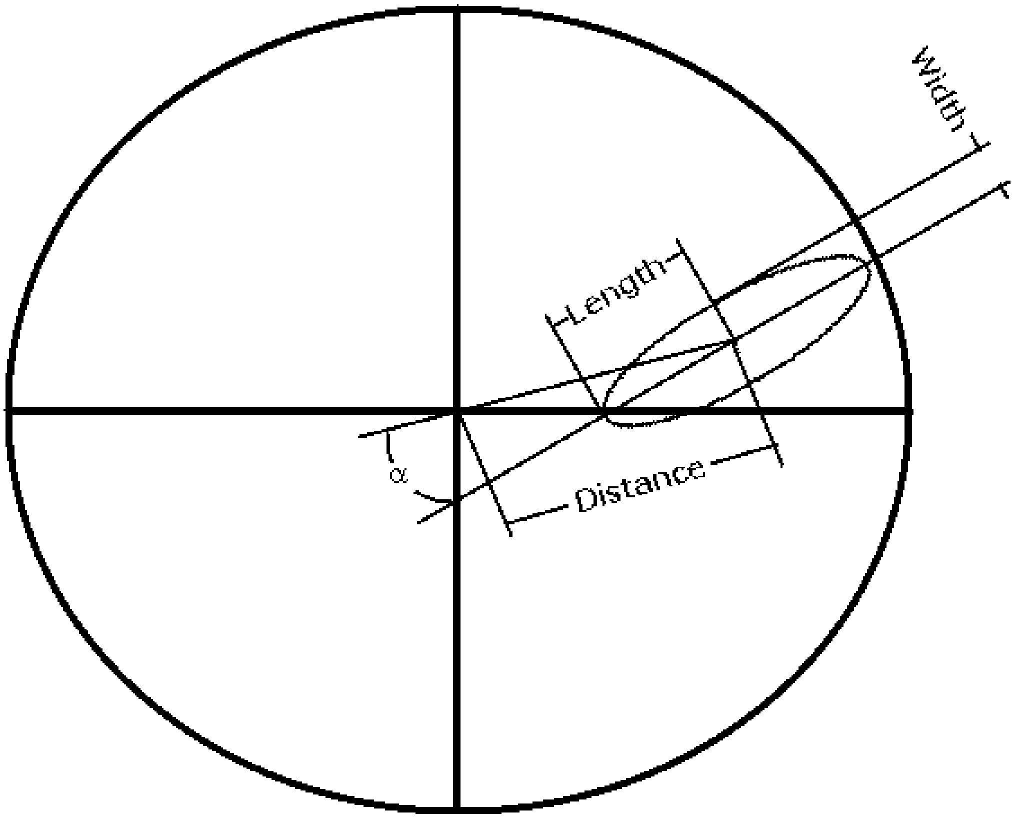

Figure 2.3 A pictorial representation of an ellipse fit to a shower image and the corresponding image parameters.

characteristic of gamma-ray showers. The α parameter is very useful when the source is known to be at the center of the FOV, since the major axis of the image represents the projection of the shower trajectory onto the image plane. Consequently, the arrival direction of the shower should lie along the extension of the image's major axis, producing small values of α for events originating from the center of the FOV. The *Distance* cut is used to remove events occurring near the edge of the FOV that could easily be misidentified due to truncation. It is also used to remove events near the center of the camera since these images contain less structure and are consequently harder to correctly identify. The $Size$ and $MaxN$ parameters are useful for rejecting noise events, which usually have weaker signals. Various selection criteria can be applied to these parameters depending on the purpose of the analysis. These shall be discussed in later sections as they are used.

For data taken in the ON/OFF mode, background subtraction is done by simply subtracting the number of gamma-ray like events in the off-source FOV from the number of gamma-ray like events in the on-source FOV, weighting for the relative observation times. For TRACKING data the diffuse nature of the background is used to separate it from the peaked signal of a point source. Events caused by gamma-rays from a source at the center of the FOV should all have a small value of the paramater α, so images that pass all the other selection criteria and have $0^\circ \leq \alpha \leq 15^\circ$ are taken as the signal. The number of background events included in this signal is estimated by counting the number of events with $20^\circ < \alpha < 65^\circ$ and scaling by a factor known as the "tracking ratio." This "tracking ratio" is estimated by looking at the ratio of the number of events in these two α ranges averaged over many off-source runs. It varies somewhat from season due to various systematic effects that are not fully understood, but always has a value close to one third.

CHAPTER 3

TEV GAMMA-RAY BURST SEARCH

3.1 Scientific Motivation

3.1.1 Overview of Primordial Black Holes

The concept of an object so dense that nothing can escape its gravitational pull is perhaps one of the most intriguing to have been suggested by modern physics. As the possibility of the existence of black holes became more accepted, people began asking the question of what implications this might have for the rest of our physical theories. One problem that arose from these speculations was that the second law of thermodynamics no longer seemed to be valid since one now had the possibility of removing entropy from causal contact with the rest of the universe by hiding it within the event horizon of a black hole.

In 1973 Beckenstein proposed a solution by equating the surface area of a black hole with its entropy (7). One of his motivations for this was the fact that, like entropy, it had been shown that the surface area of a black hole can never decrease, but only increase (8). This solution provided some explanation but encountered problems due to the fact that it seemed difficult to consider this newly defined black hole entropy as a real entropy. Namely, if one can define an entropy for an object, then the laws of thermodynamics state one should also be able to define a temperature, and if there is a temperature, there should be black body radiation. Without such radiation, the second law of thermodynamics would still be violated if, for instance, a black hole were placed in a radiation field with a lower temperature than itself (9).

In 1974 this problem was resolved when Stephen Hawking showed that when quantum mechanical effects near the event horizon of a black hole are taken into account, black holes will indeed radiate as black bodies with a temperature $T_{BH} = \hbar c^3/8\pi GM$ (10). One can picture the emission process by considering a virtual pair of particles with zero net energy appearing near the event horizon of a black hole. Normally the particle with negative energy, since it is classically forbidden, must annihilate with its positive energy partner. If, however, it falls into the black hole, it will be in a region where it can continue existing as a real particle (9). The positive energy partner is then free to escape and will appear to an outside observer as if it was emitted from the black hole (Fig. 3.1).

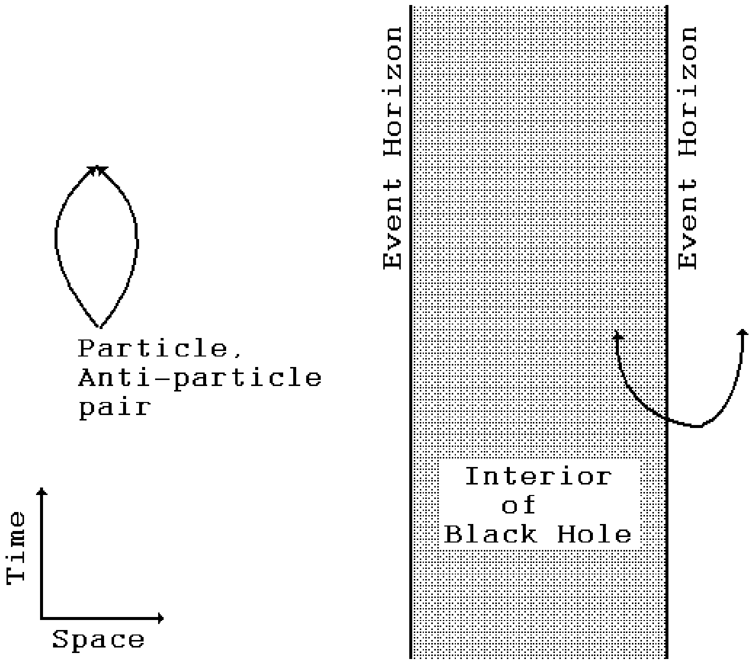

Figure 3.1 An illustration of one of the ways of visualizing Hawking radiation. The negative energy partner of the virtual particle-antiparticle pair on the right falls into the event horizon, allowing the positive energy particle to escape to infinity.

For black holes formed from stellar collapse, these emissions have little observational effect since they will have masses on the order of or greater than the sun's mass, implying a temperature that is less than 10^{-7} K. However, density perturbations formed in the early universe could also have collapsed into black holes of much smaller masses. Such black holes are referred to as primordial black holes (PBHs) and could potentially produce enough radiation to be observed.

PBHs lose mass at a rate of

$$\frac{dM}{dt} = -\frac{\alpha[E(M)]}{M^2} \tag{3.1}$$

due to Hawking radiation (11). The increase in the evaporation rate as the mass decreases leads to a runaway process that, depending on the physics governing the final stages of evaporation, could result in a violent explosion. The factor $\alpha[E(M)]$ depends on the degrees of freedom available to the radiated particles at a temperature, E, determined my the black hole's mass, M. Consequently, the exact fate of a PBH as its mass drops toward zero is an open question since the value of $\alpha(E)$ is unknown for energies above those available to current accelerators.

Although PBHs will produce fluxes of cosmic-rays and neutrinos that are comparable to the gamma-ray flux, the larger diffuse backgrounds for the former two mean that the gamma-ray signal will be the easier to detect (11). The detection of any such signal would have profound implications. First, it would confirm Hawking's prediction that black holes do indeed radiate energy. It would also give us insight into the conditions of the early universe under which the PBHs formed and into the particle physics that determines the emissions during the final seconds of a PBH's lifetime. These implications will be discussed in more detail in section 3.1.4.

3.1.2 Calculations of PBH Emissions

In this section we calculate the expected gamma-ray emissions from a PBH. We will work in units where $G = c = \hbar = 1$. For an uncharged, non-rotating black hole, the number of emitted particles per unit time and energy is

$$\frac{d^2N}{dtdE} = \frac{\Gamma_s(ME)}{2\pi}\left[\exp(8\pi ME) - (-1)^{2s}\right]^{-1} \tag{3.2}$$

for each particle species, angular momentum state, and spin. Here, M is the black hole mass, s is the particle's spin, and $\Gamma_s(ME)$ is the absorption probability for a particle of spin s and energy E on a black hole of mass M (12). For small values of ME, analytic solutions for $\Gamma_s(ME)$ can be found. These are given by (13)

$$\Gamma_{1/2}(ME) = (ME)^2, \text{and} \tag{3.3}$$

$$\Gamma_1(ME) = \frac{64}{9}(ME)^4. \tag{3.4}$$

Exact solutions can be found following the methods of Teukolsky and Press (14). The absorption probability is given by

$$\Gamma_s = \frac{dE_{hole}/dt}{dE_{in}/dt}, \tag{3.5}$$

where E_{hole} is the energy flowing into the black hole at the event horizon and E_{in} is the inward flow of energy an infinite distance from the black hole. The difficulty that arises in solving the differential equations that determine these quantities lies in the fact that working in a coordinate system that produces well behaved solutions on the event horizon produces divergent solutions at infinity, and vice versa. Consequently, Teukolsky and Press have derived a series of coordinate transformations that allow one to change coordinates mid-calculation. Thus, one can start integrating at the event horizon using coordinates that are well behaved there and then at some moderate radius switch to coordinates that are well behaved at larger radii.

The coordinates used in this work are the Kerr "ingoing" coordinates, which are the same as spherical coordinates, but replacing the time, t, with ν such that

$$d\nu = dt + \frac{rdr}{r-2M}. \tag{3.6}$$

In these coordinates, the Schwarzschild metric becomes

$$ds^2 = \left(1 - \frac{2M}{r}\right) d\nu^2 - 2d\nu dr - r^2 d\theta^2 - r^2 \sin^2 d\phi^2, \tag{3.7}$$

which, unlike with regular spherical coordinates, is well behaved at the event horizon, $r_h = 2M$. Two different tetrads are used — one near the event horizon and one at large distances. For large radii, Kinnersley's tetrad (15) is used, with $[\nu, r, \theta, \phi]$ components

$$\begin{aligned} \mathbf{l}^\mu &= \left[\frac{r}{r-2M}, 1 - \frac{r}{r-2M}, 0, 0\right] && (3.8) \\ \mathbf{n}^\mu &= \left[\frac{1}{2}, \frac{-3r^2 + 4M^2 - 4rM}{2r(r-2M)}, 0, 0\right] && (3.9) \\ \mathbf{m}^\mu &= \left[0, -\frac{r}{r-2m}, \frac{1}{\sqrt{2}r}, \frac{i}{\sqrt{2}r \sin\theta}\right]. && (3.10) \end{aligned}$$

Near the event horizon a different tetrad is used, which can be obtained from Kinnersley's tetrad via the transformation

$$\begin{aligned} \mathbf{l}^\dagger &= -2\frac{r}{r-2M}\mathbf{n} && (3.11) \\ \mathbf{n}^\dagger &= -\frac{r-2M}{2r}\mathbf{l} && (3.12) \\ \mathbf{m}^\dagger &= \mathbf{m}^*, && (3.13) \end{aligned}$$

where the "$*$" denotes complex conjugation. Using these two different tetrads, we obtain two different differential equations for the radial part of the field:

$$r(r-2M)\frac{d^2R_s}{dr^2}+2[(s+1)(r-M)-iEr^2]\frac{dR_s}{dr}-\frac{4iEsr(r-M)}{r-2m}R_s \\ +2(2s-1)iErR_s-\lambda R_s=0,\text{ and} \tag{3.14}$$

$$r(r-2M)\frac{d^2\tilde{R}_s}{dr^2}+2[(s+1)(r-M)-iEr^2]\frac{d\tilde{R}_s}{dr}-2(2s+1)iEr\tilde{R}_s-\lambda\tilde{R}_s, \tag{3.15}$$

where $\lambda = l(l+1)-s(s+1)$ for a particle with spin s and total angular momentum l. The variable R_s uses Kinnersley's tetrad and $\tilde{R}_s$ the "daggered" tetrad. To calculate the ratio of the incoming energy flux at the event horizon and at radial infinity, we start by integrating the equation for $\tilde{R}$ at $r=2M$ and proceed to some moderate radius where we change to the R equation. The transformation between these tetrads is done in two steps. First, R_{-s} and its first two derivatives are calculated from $\tilde{R}_s$, and then from these R_s is calculated. For $s=1/2$ start with

$$R_{-1/2}=\frac{1}{\sqrt{2}}\sqrt{r(r-2M)}\tilde{R}_{1/2}, \tag{3.16}$$

and find the first two derivatives of $R_{-1/2}$ by taking derivatives of 3.16 and using 3.15 to write the second derivative of $\tilde{R}_{1/2}$ as a function of the first two. To calculate $R_{1/2}$, we use

$$R_{1/2}=\frac{dR_{-1/2}}{dr}-\frac{2iEr}{r-2M}R_{-1/2} \tag{3.17}$$

and its derivatives, this time using 3.14 to eliminate higher order derivatives. For $s=1$ particles, the corresponding equations are

$$R_{-1}=\frac{1}{2}r(r-2M)\tilde{R}_1,\text{and} \tag{3.18}$$

$$R_1 = \frac{-4iEr}{r-2M}\frac{d\tilde{R}_{-1}}{dr} + \frac{4(1+iEr)}{r(r-2M)}\tilde{R}_{-1} - \frac{4E^2r^2}{(r-2M)^2}\tilde{R}_{-1}. \tag{3.19}$$

In order to test these transformations, the value of r at which this transformation is made is varied from $5M$ to $20M$. No change in the final result is observed. Since Γ_s depends on the ingoing fluxes at $r = 2M$ and $r = \infty$, it is important to understand the asymptotic solutions to equations 3.14 and 3.15 at these limits. These are summarized in table 3.1. The advantages of the above choice of coordinates can now be seen. First, it is easy to set the initial conditions for an ingoing wave on the event horizon. Second, the outgoing wave falls off quicker than the ingoing wave for large r, allowing one to easily pick out the ingoing part simply by integrating out to sufficiently large values of r. Thus, one need not worry about the solution being contaminated by errors in the outgoing wave, which is not well defined on the event horizon.

Table 3.1 Asymptotic values for the ingoing and outgoing parts of R_s and $\tilde{R}_s$ for $r = 2M$ and $r = \infty$. The value r^* is defined by $dr^*/dr = r/(r-2M)$. Y_{out}, Y_{in}, Z_{out}, and Z_{in} are constants.

	Outgoing Wave	Incoming Wave
$lim_{r\to\infty} R$	$Z_{out}\exp(2iEr^*)/r^{2s+1}$	Z_{in}/r
$lim_{r\to 2M} \tilde{R}$	$Y_{out}\exp(2iEr^*)/r(r-2M)$	Y_{in}

All that remains are formulas for dE_{hole}/dt, and dE_{in}/dt. For $s = 1/2$ these are

$$\frac{dE_{hole}}{dt} = 2\pi E|Y_{in}|^2, \text{and} \tag{3.20}$$

$$\frac{dE_{in}}{dt} = 4\pi E|Z_{in}|^2, \tag{3.21}$$

and for $s = 1$ they are

$$\frac{dE_{hole}}{dt} = 256E^2M^6\left(E^2 + \frac{1}{16M^2}\right)|Y_{in}|^2, \text{and} \tag{3.22}$$

$$\frac{dE_{in}}{dt} = \frac{1}{4}|Z_{in}|^2. \tag{3.23}$$

Plots of $\Gamma_{1/2}$ and Γ_1 are given in figure 3.2 using both the exact solutions from equation 3.5 and the approximate solutions from equation 3.3. It can be seen that although the analytic solutions do agree with the numerically integrated solutions for small values of ME, significant discrepancies develop relatively quickly. Thus, it is necessary to use the full solutions for calculating the PBH gamma-ray spectrum rather than the asymptotic ones.

Once Γ_s has been calculated, the derivation of the rate of mass loss of the PBH is straightforward. If we let $d_s(E)$ be the number of degrees of freedom available to outgoing radiation with spin s and energy E, then

$$\frac{dM}{dt} = -\int_0^\infty dE\frac{d_{1/2}(E)\Gamma_{1/2}(ME)}{2\pi}\left[\exp(8\pi ME)+1\right]^{-1} \tag{3.24}$$

$$-\int_0^\infty dE\frac{d_1(E)\Gamma_1(ME)}{2\pi}\left[\exp(8\pi ME)-1\right]^{-1}.$$

If $d_s(E)$ becomes constant above some energy, then equation 3.1 can be approximated as

$$\frac{dM}{dt} = \frac{1}{M^2}\frac{1}{2\pi}\left[d_{1/2}\int_0^\infty dx\Gamma_{1/2}(x)\left[\mathrm{e}^{8\pi x}+1\right]^{-1} - d_1\int_0^\infty dx\Gamma_1(x)\left[\mathrm{e}^{8\pi x}-1\right]^{-1}\right]. \tag{3.25}$$

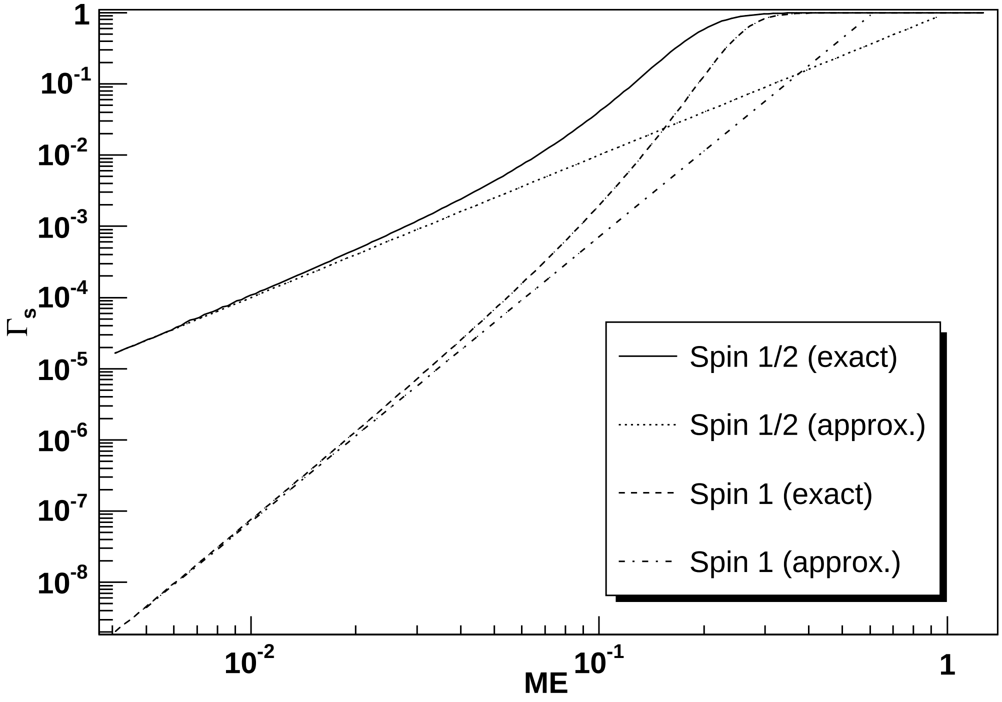

Figure 3.2 Values of $\Gamma_{1/2}$ and Γ_1 from both the analytic approximations and the full integrals versus the dimensionless parameter ME.

We can now compute the function $\alpha(E)$ in equation 3.1. We find that

$$\alpha(E) \approx [3.94 d_{1/2}(E) + 1.64 d_1(E)] \times 10^{-5}, \tag{3.26}$$

where $d_s(E)$ is the number of degrees of freedom (spin, charge, and color) for all particles with spin s and rest mass $> E$. At the lowest temperatures, only massless and near-massless particles such as photons and neutrinos will be emitted. As the black hole evaporates and its temperature increases, more particle species will be produced. Below the QCD confinement scale of about 250 MeV, free quarks and gluons cannot be produced, but sufficiently light hadrons, like the pion, will be emitted instead. Above this temperature, it is believed that quarks and gluons are produced directly rather than composite particles such as hadrons (16). If we assume only the known fundamental Standard Model particles, then above the top quark mass, $d_{1/2} = 90$ and $d_1 = 27$, yielding $\alpha(E > M_{top}) = 3.99 \times 10^{-3}$ (Fig. 3.3).

There are two ways by which PBHs are believed to produce gamma-rays — through the direct emission of photons and through the fragmentation products of other particles. The contribution from direct emission can simply be calculated from equation 3.2. The second method relies on the fact that the quarks and gluons that are emitted will fragment into pions. The neutral pions can then decay, producing two photons each. In this work, an empirical fragmentation function is used (11)

$$\frac{dN_\pi}{dz} = \frac{15}{16} z^{-3/2} (1 - z)^2, \tag{3.27}$$

where $z = E_\pi / E_p$ and E_p is the quark or gluon (parton) energy. For the pion decay,

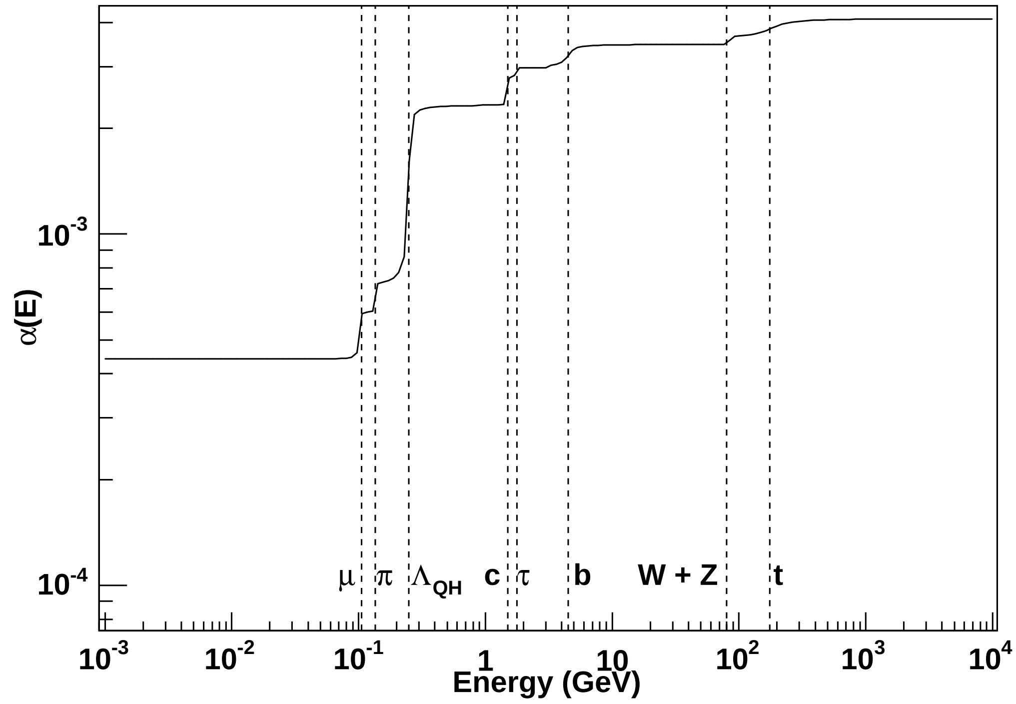

Figure 3.3 The parameter $\alpha(E)$ versus energy including all known Standard Model particles. The energies above which the various particle species are produced are indicated by the dashed lines. Above the QCD confinement scale, Λ_{QH}, quarks and gluons are produced directly rather than hadrons.

a flat photon spectrum is used:

$$\frac{dN_\gamma}{dE_\pi} = \Theta[E - (E_\pi - P_\pi)/2] - \Theta[E - (E_\pi + P_\pi)/2]\frac{1}{P_\pi}. \tag{3.28}$$

Here, P_π is the pion's momentum. These fragmentation emissions dominate over the direct photon emissions since there are 72 quark and 16 gluon degrees of freedom, compared to the 2 photon degrees of freedom.

3.1.3 Particle Physics Models

For most of this work we will only consider known Standard Model particles. In this case, the maximum number of particle degrees of freedom are $d_{1/2}(E) = 90$ and $d_1(E) = 27$. For energies well above the top quark mass of about 175 GeV, $\alpha(E) \approx 3.99 \times 10^{-3}$, as given by equation 3.26. The time over which this approximation is valid can be found by integrating equation 3.26 and finding the maximum time for which the PBH's temperature is above the top mass. For a constant $\alpha(E)$ we have

$$m(\Delta t) = (3\alpha\Delta t)^{1/3} \tag{3.29}$$

for the mass of a PBH a time Δt before total evaporation. Using the fact that the effective temperature of a black hole is $1/8\pi M$, we see that the PBH's temperature will reach the top quark mass approximately 26 hours before total evaporation. Thus in the Standard Model scenario, $\alpha(E)$ can be taken to have the constant value of 3.99×10^{-3} when searching for second-scale bursts.

We now want to calculate the number of gamma-rays produced, both directly and from the fragmentation of quarks and gluons, above an energy threshold E_D over the last Δt seconds of the PBH's life. We start by integrating equation 3.2 over time and using equation 3.1 to convert it into an integral over mass. This yields

$$\frac{dN}{dE} = \frac{1}{2\pi\alpha} E^{-3} \int_0^{M(\Delta t)E} dx x^2 \Gamma_s(x) \left[\exp(8\pi x) - (-1)^{2s}\right]^{-1} \tag{3.30}$$

where the substitution $x = ME$ has been made. Figure 3.4 shows the value of

$$f(x) = x^2 \Gamma_s(x) \left[\exp(8\pi x) - (-1)^{2s}\right]^{-1} \tag{3.31}$$

versus x for both spin 1/2 and spin 1 particles. It can be seen that $f(x)$ acquires its maximum value at $x_{max} = 0.195$ for spin 1/2 particles and at $x_{max} = 0.252$ for spin 1 particles. Following the procedure of (11), we now approximate $f(x)$ as a delta function centered at the maximum x value. This corresponds to an energy

$$Q = \frac{x_{max}}{(3\alpha\Delta t)^{1/3}}. \tag{3.32}$$

Under this approximation, the energy spectrum becomes

$$\frac{dN}{dE} = \frac{C_s}{2\pi\alpha} E^{-3} \Theta(E - Q), \tag{3.33}$$

where $\Theta(x)$ is the usual Heaviside step function and the normalization C_s is defined as

$$C_s = \int_0^{\infty} dx f(x). \tag{3.34}$$

Integrating numerically we find $C_{1/2} = 4.700 \times 10^{-5}$ and $C_1 = 2.541 \times 10^{-5}$.

The calculation of the direct photon emission can be done by integrating equation 3.33 above E_D and multiplying by two for the two helicity states. For the fragmentation photons, equations 3.27 and 3.28 are used to calculate the number of

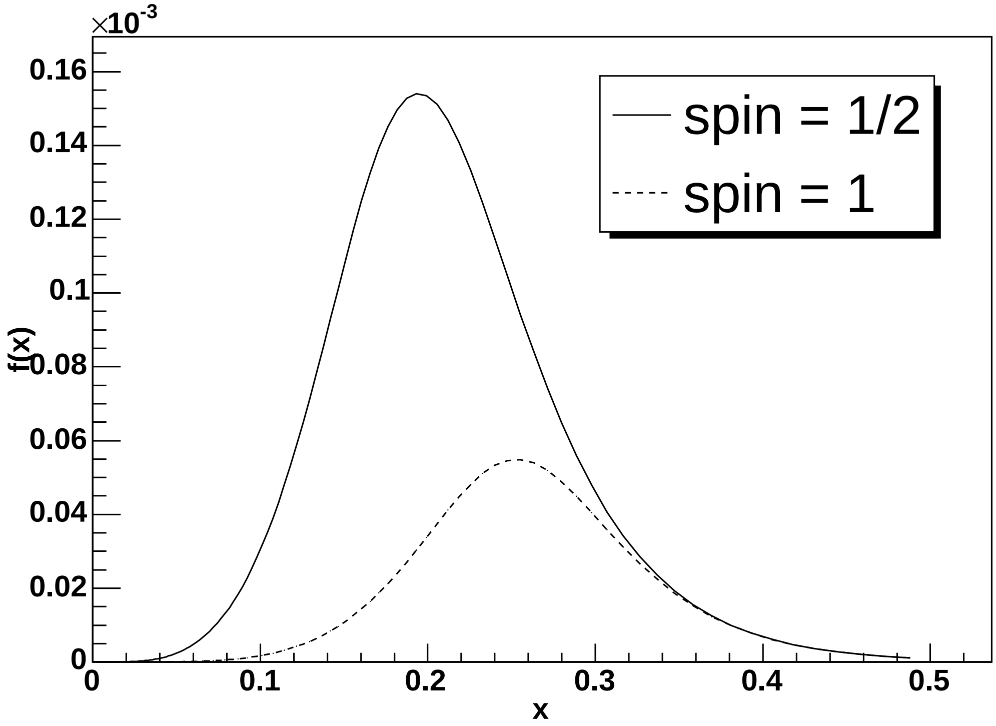

Figure 3.4 The function $f(x)$ versus x for both spin 1/2 and spin 1 particles as defined in equation 3.31.

pions produced from the quarks and gluons, and the number of photons then produced from the pion decay. Equation 3.28 is simplified by using the fact that we are only interested in energies well above the pion mass and can thus treat them as being massless, setting $E_\pi = P_\pi$. One additional simplification is made by using the Q value for $s = 1/2$ for both spin 1/2 and spin 1 particles. Counting 72 quark degrees of freedom and 16 gluon degrees of freedom in addition to the two direct photon emission degrees of freedom, we find

$$N(> E_D) = \frac{3.791 \times 10^{-3}}{2\pi\alpha Q^2} \times \tag{3.35}$$

$$\left[\frac{5}{14}\left(\frac{E_D}{Q}\right)^{3/2} + 3\sqrt{\frac{E_D}{Q}} + \frac{5}{6}\sqrt{\frac{Q}{E_D}} - \frac{5}{3}\frac{E_D}{Q} - \frac{5}{2} + \frac{1}{150}\right]$$

for $E_D < Q$, and

$$N(> E_D) = \frac{3.791 \times 10^{-3}}{2\pi\alpha E_D^2}\left[\frac{1}{42} + \frac{1}{150}\right] \tag{3.36}$$

for $E_D \geq Q$, where the 1/150 term in both equations comes from the direct photon emission. These correspond to equation 16 in reference (11). Figure 3.5 compares equation 3.35 with the results of the full calculation for $\Delta t = 1$ s. The two methods can be seen to be in good agreement.

An example of a more extreme model is the Hagedorn model in which the number of particle degrees of freedom increases exponentially with energy (17; 18). Although not currently favored, an as of yet unknown phase transition at some energy scale, Λ, could produce an exponential increase in particle degrees of freedom over some limited energy range (11). In this model the number of degrees of freedom is given by

$$d(E) = AE^{-5/2}e^{E/\Lambda}. \tag{3.37}$$

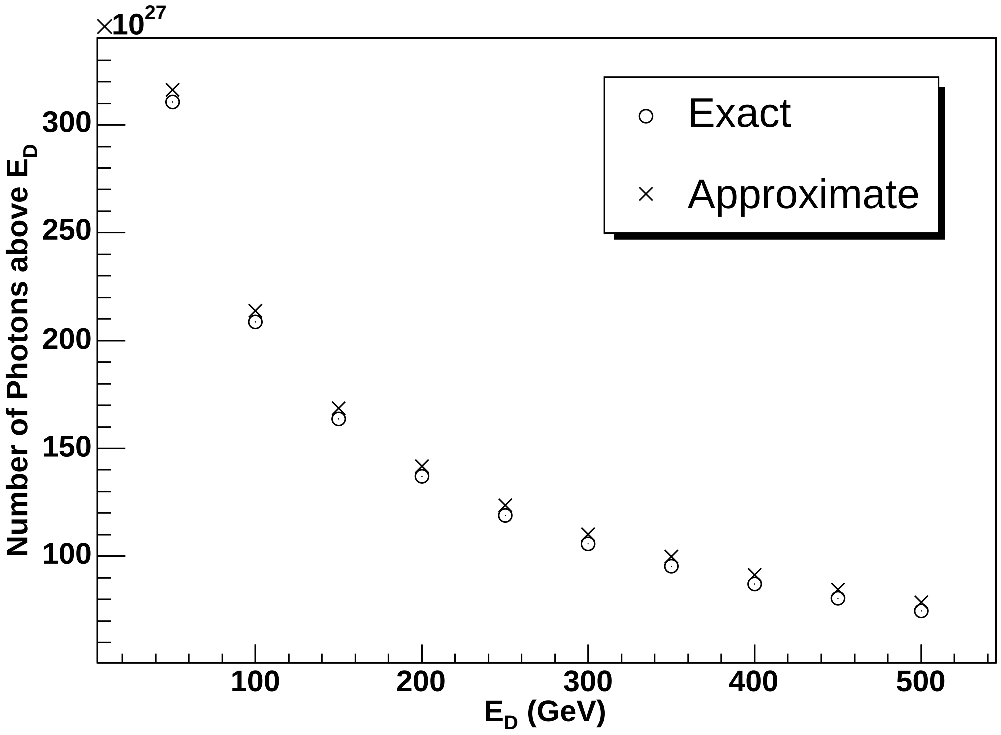

Figure 3.5 The number of photons emitted from a PBH over the last second of its lifetime above the energy E_D calculated using both the approximation in equation 3.35 and the full calculation.

For energies below 2.5Λ, $d(E)$ decreases with increasing energy. For the purposes of this work, the Standard Model is assumed to hold up to this energy at which point the Hagedorn equation is used. The normalization A is chosen such that $d(E)$ is continuous at $E = 2.5\Lambda$.

3.1.4 Implications of PBH Observations

There are many uncertainties in PBH physics, from the production method of the PBHs themselves to the details of the emission of Hawking radiation, that make deriving a precise gamma-ray spectrum difficult. On the other hand, these unknowns mean that the detection of PBHs would provide valuable insight into a number of different areas of physics. Indeed, even the upper limits that have been set on the PBH density have had important implications.

One possible source of PBHs is density fluctuations in the early universe. Thus, a limit on the present-day density of PBHs will serve as a limit on the size of these perturbations. To obtain an estimate of the time probed by such a search, we first calculate the initial mass of PBHs formed during the first few seconds after the big bang that will just finish their evaporation today. Since any extensions to the Standard Model will only affect the final stages of PBH evaporation, we neglect these for this calculation. Integrating equation 3.24 over the age of the universe, approximately $4.3 \times 10^{17} s$, we find the initial mass to be $2.18 \times 10^{19} M_{pl}$, or 4.74×10^{14} g.

The formation time, t_f, for a PBH of a given initial mass, M_i, can be estimated by noting that the initial mass of a PBH is approximately the horizon mass at the time of formation. This is because the minimum radius for a perturbation to collapse into a PBH is the Jeans length, given by $r_J = \sqrt{w} \times r_h$, where w is the pressure of the universe divided by its density, and r_h is the horizon size. The early universe is thought to have been radiation dominated, giving $w = 1/3$. This yields a lower limit on M_i of $M_h/\sqrt{3}$. An upper limit on the perturbation mass can be set at M_h, since perturbations larger than this will no longer be in causal contact with our universe once they collapse (19). So $M_i \approx M_h \approx t_f$. For a PBH just evaporating today $t_f \approx 2.18 \times 10^{19} t_{pl} = 1.17 \times 10^{-24}$ s. Thus PBHs are a probe to a time well before the formation of the cosmic microwave background.

If we let $F_{pbh}(M)$ be the fraction of regions in the early universe of mass M that collapse into PBHs, then it is related to the root-mean-square amplitude of density perturbations entering the horizon at that mass, $\epsilon(M)$, by (20)

$$F_{pbh}(M) \sim \epsilon(M) \text{exp} \left[-\frac{w^2}{2\epsilon(M)^2} \right]. \tag{3.38}$$

As before, w is the equation of state of the universe. If we assume that $\epsilon(M)$ is constant with M then it is possible for the PBHs to have an extended mass spectrum (20). Making this assumption and using the fact that radiation density scales as $(1+z)^4$ while matter density scales as $(1+z)^3$, we can relate the present day PBH density to the initial density by

$$\Omega_{pbh} = F_{pbh} \Omega_R (1+z) \approx 10^{18} F_{pbh} \left(\frac{s}{t} \right)^{1/2}. \tag{3.39}$$

Here t is the formation time of the PBH in seconds, and we use the fact that the microwave background has a density of $\Omega_R \approx 10^{-4}$. Thus, from equations 3.38 and 3.39 we can relate the present day PBH density to the amplitude of density perturbations at a time of about 1.17×10^{-24} s after the big bang.

The detection of PBHs could also yield valuable information about particle physics beyond energies accessible to current accelerators. The existence of a phase transition as described by equation 3.37 above could have a significant impact on the energy spectrum of the final burst of photons from a PBH. Since only on the order of a few to ten detected photons are expected from a given evaporation, it would not be feasible to derive an energy spectrum for such an event. However, multiple experiments with different energy thresholds are carrying out PBH searches (see section 3.4.1). If at least one of these manages to detect PBHs, then the relative densities (actual values or upper limits) set at the different energy ranges would provide information on the energy spectrum.

3.1.5 Other Sources of TeV Bursts

This search for TeV gamma-ray bursts need not be thought of solely as a PBH search. There are other possible sources for such bursts, the detection of any of which would be very interesting. One possibility is a high energy component to MeV gamma-ray bursts (GRBs). The observations of optical counterparts to some GRBs has lead some to conclude that there is a population of seed electrons producing synchrotron radiation. These electrons could inverse Compton scatter some of the MeV photons to TeV energies (21). Another possibility would be the detection of the decay of massive relic particles from the early universe that have clustered within the galactic halo (22). It is also possible that some new, yet unknown source of TeV gamma rays could be discovered through such a search.

3.2 Search Methodology

3.2.1 Overview

In this section we discuss the procedure used for searching for PBHs using the Whipple 10-m telescope. It starts with an explanation of how the observations to be included in the search are selected (section 3.2.2). Section 3.2.3 then gives an overview of a method for reconstructing the arrival direction of gamma-ray events occuring anywhere within the field of view of the camera. The use of this technique to search for bursts of gamma rays is then covered in section 3.2.4. To convert these burst measurements into upper limits on the local PBH evaporation rate, several steps must then be taken: the expected number of bursts from statistical fluctations must be estimated (section 3.2.5), the detector sensitivity must be simulated (section 3.2.6), and the statistical significance of the observed bursts must be calculated (section 3.2.7).

3.2.2 The Data Set

This work uses data taken from January of 1998 through July of 2003 and is divided into three sections based upon when the camera was upgraded (see section 2.2). The first period starts in January 1998 and continues through the spring of 1999, during which time the 331 PMT camera was used. The 379 PMT camera was installed in the summer before the 1999-2000 observing season, which makes up the second period. The upgrade was not fully complete until the fall of 2000, and so the third period begins there and continues through the spring of 2003.

For this search, all data taken in good weather is used. The quality of the weather is judged in two manners. First, the somewhat subjective rating assigned by the local observer for each run is used, and only weather rated “A-” or above is selected. Second, the standard deviation of the camera trigger rate as recorded each minute during every run is examined. If the rates vary too drastically that can be an indication that clouds are passing through the FOV, and so such data are also discarded.

Data taken with a known source within the FOV can still be used since source rates are typically on the order of minutes^{-1} and so would have little effect on a search for second scale bursts. In addition the method used for estimating the background (section 3.2.5) automatically eliminates the effects of steady sources. If a very strong source (such as a blazar in a flaring state) were producing second-scale bursts, this signal may be detected. However, such a result is not observed, and would have been interesting in its own right anyway. In all, over 2,000 hours of data meet the above requirements, as is summarized in table 3.2.

Table 3.2 Hours of data taken per observing season under good enough weather conditions to be used in this work.

Season	Camera	Hours of Data
Spring '98	331 pixel	206
1998-1999	331 pixel	368
1999-2000	379 pixel	335
2000-2001	379 pixel	459
2001-2002	379 pixel	467
2002-2003	379 pixel	356
total	—	2,191

3.2.3 Analysis of Off-axis Sources

The gamma-ray selection criteria discussed in section 2.4 have been optimized for sources located in the center of the FOV. However, by taking advantage of shower properties, this technique can be extended to have considerable sensitivity across the entire FOV of the camera. As mentioned above, the arrival direction of a Čerenkov shower in the image plane lies along the major axis of an ellipse fit to the shower image. Simulations show that the specific arrival direction along this axis can be estimated from parameters of the image's shape (23). The larger the impact parameter of a shower, the more elongated its image in the camera becomes and the farther its centroid appears from its actual arrival direction. We thus introduce a new parameter *Disp* defined by

$$Disp = \xi \left(1 - \frac{Width}{Length}\right), \tag{3.40}$$

which gives an estimate of the angular distance between the image centroid and the arrival direction. The parameter ξ is a fixed coefficient whose value is determined empirically. First, the arrival direction of events produced with a known point source in the center of the FOV are binned in a two-dimensional histogram. Then the events from a corresponding off-source run (sec. 2.3) are binned in the same manner and subtracted from the on-source histogram. A Gaussian is fit to the excess and the standard deviation is taken as a measure of the camera's angular resolution. This procedure is repeated for different values of ξ and the one that produces the best angular resolution is used for future analysis (Fig. 3.6). This determination of the arrival direction has a two-fold degeneracy in that the actual arrival direction can be in either direction along the ellipse's major axis. Distinguishing between these two directions for off-axis images has proven problematical due to image truncation effects, so in this work both directions are given equal weight.

Since there is some uncertainty as to the actual arrival direction of an event relative to the estimated arrival direction, a smoothing function is often used when creating significance maps of sources. Usually this is either a circular step function or a two-dimensional Gaussian. For the purposes of this burst search, a step function will be used to simplify the determination of which events belong to the same burst.

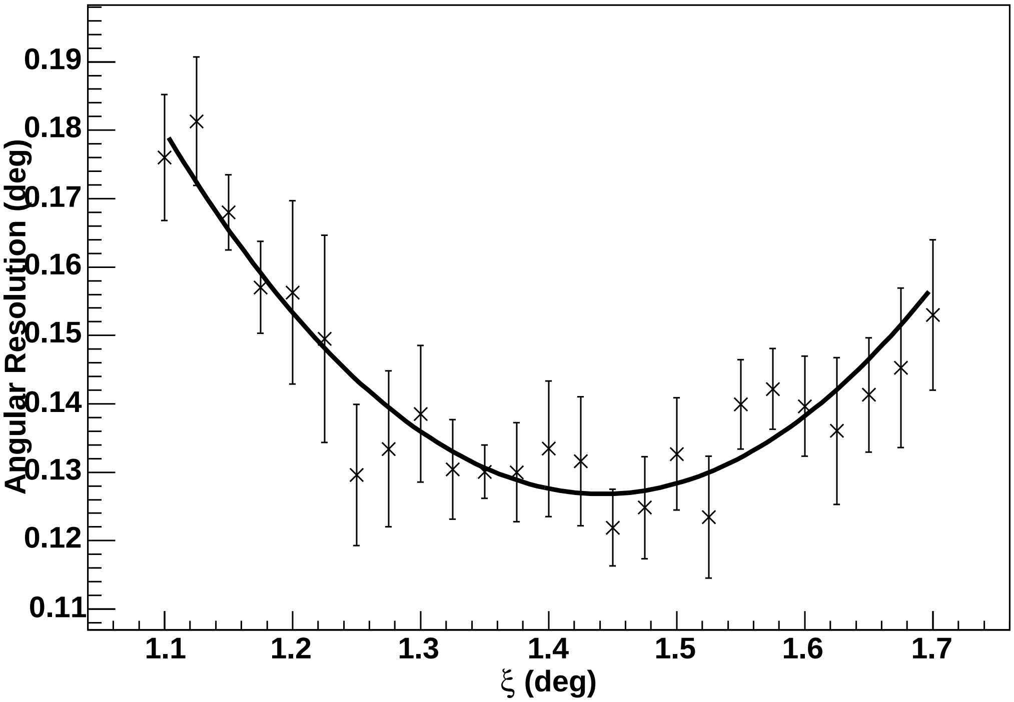

Figure 3.6 Plot of angular resolution versus ξ (see eq. 3.40) using approximately 38 hours of observations made on the Crab Nebula during the 2001/2002 observing season. A parabolic fit to the data is used to determine both the optimal value of ξ and the angular resolution of the camera. Values of 1.44° and 0.13° are obtained for ξ and the angular resolution, respectively.

More details on this will be given in section 3.2.4.

In order to demonstrate that this off-axis analysis technique works, observations of the Crab Nebula are made with the telescope deliberately offset from the true source direction by various fixed amounts. The Crab Nebula is used because it is a bright, steady source of TeV gamma rays, which makes it a useful standard candle. In each case, following the procedure of Lessard, *et. al.* (23), the image of the Crab Nebula is successfully reconstructed with good pointing accuracy (Fig. 3.7).

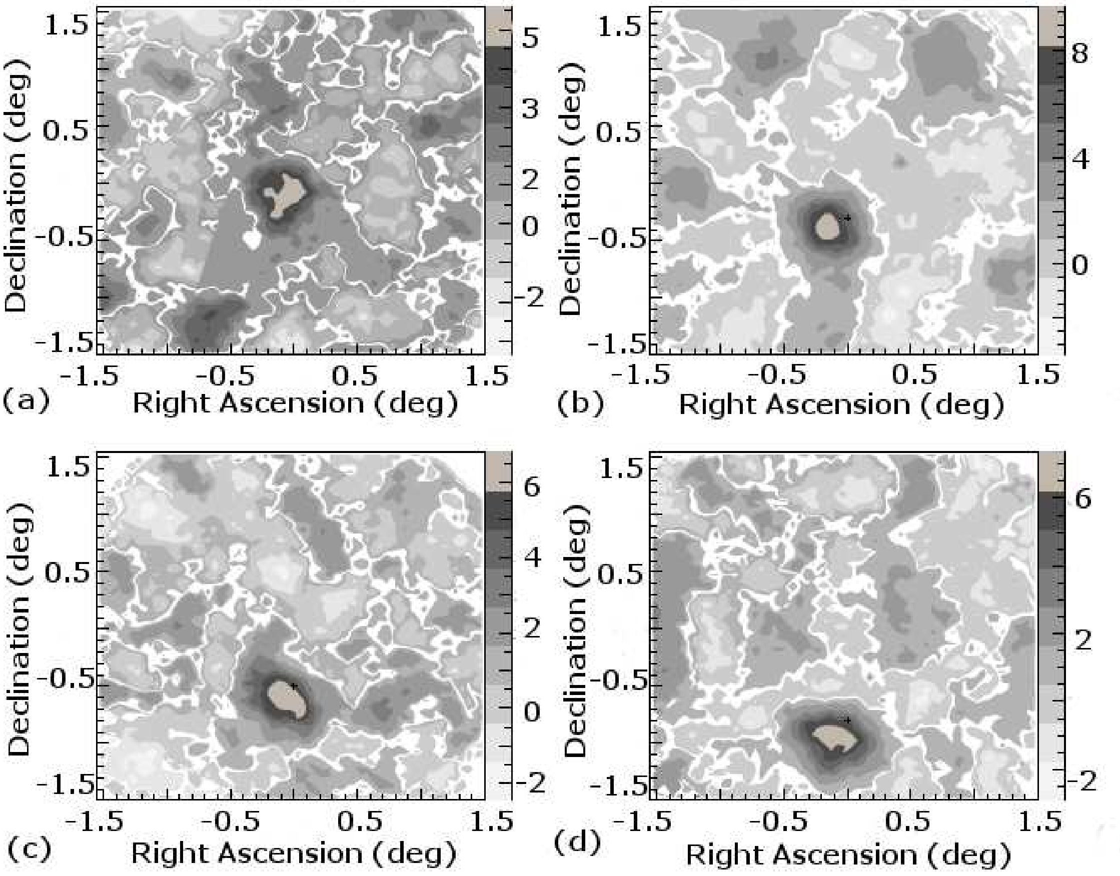

Figure 3.7 Reconstructed images of the Crab Nebula offset by (a) 0.0°, (b) 0.3°, (c) 0.5°, and (d) 0.8° from the telescope's pointing axis. Contours indicate the significance level of the detection at each point within the FOV.

Although sources not at the center of the FOV can still be detected, the farther off-axis a source is, the less likely it is that the shower image will fall within the camera's FOV. Consequently, the collection area of the telescope decreases with increasing offset angle, θ. It will be convenient for future calculations to parameterize the θ dependence of the collection area as $A(\theta) = A_{\circ}a(\theta)$, with $a(0) = 1$.

The most straightforward method for finding $a(\theta)$ is from the gamma-ray rates of the Crab Nebula measured with the telescope deliberately offset from the true source position, but such observations were not made in sufficient quantity for all camera configurations. Consequently, the KASCADE simulation package (24) is used to determine the off-axis sensitivity of the camera. When compared with the available off-axis Crab observations, these results are found to be in reasonable agreement (Fig. 3.8). The energy dependence of $a(\theta)$ is tested by running simulations at various energies. Below about 2 TeV, little variation is found. Above this energy, the contribution to the PBH signal drops off rapidly using the spectrum calculated for the Standard Model in section 3.1.3, so the variations in $a(\theta)$ above this energy are ignored.

3.2.4 Finding Bursts

Calculations assuming the Standard Model of particle physics indicate that detectable fluxes of TeV gamma rays are produced during the last few seconds of a PBH's life (11). A previous work made a search for TeV gamma-ray bursts within a time window, Δt, of 1 s using data taken by the Whipple telescope from 1988 to 1992 (25). Due to difficulties in predicting the background rate, selecting the optimal time window for the search *a priori* is not straightforward. Consequently, in this current work bursts of 1 s, 3 s, and 5 s durations are sought.

In addition to all the events of a burst falling within a given time window, it is

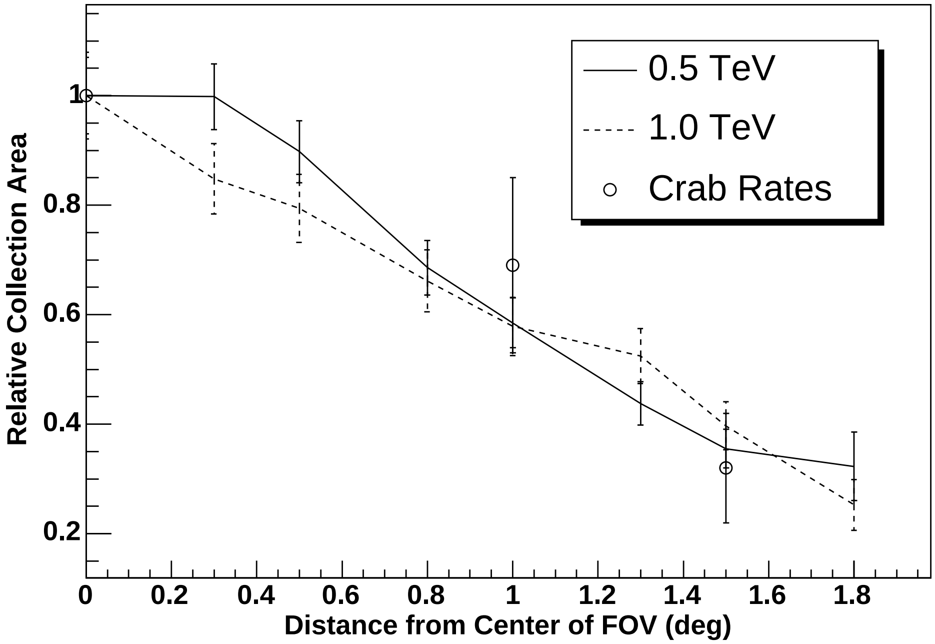

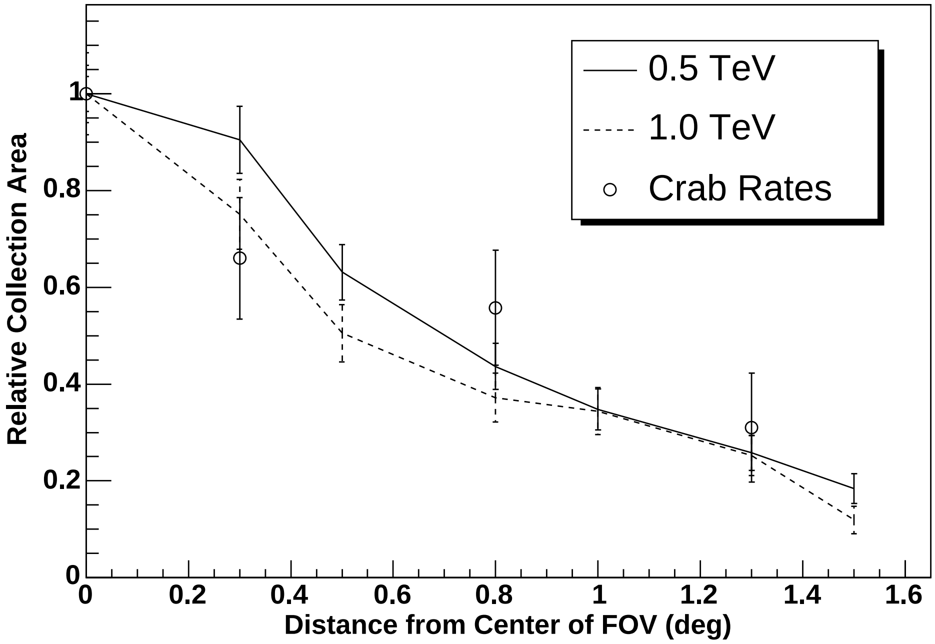

Figure 3.8 Simulated off-axis response for the Whipple camera compared with rates for the Crab Nebula taken with the telescope offset from the true source position. The upper plot is for the 331 PMT camera, with Crab rates from reference (23). The lower plot is for the most recent configuration of the 379 PMT camera.

also required that their arrival directions overlap to within the angular resolution of the camera ($\sigma \approx 0.13°$), as shown in Fig. 3.9. This is equivalent to saying that some circle with a radius equal to the angular resolution, σ, contains all the event arrival directions. With the time constraint added, a burst can then be defined as a group of events falling within a space-time cylinder of height Δt and radius σ. The size of a burst is defined as the number of events within a burst (not to be confused with the *Size* parameter defined in section 2.4).

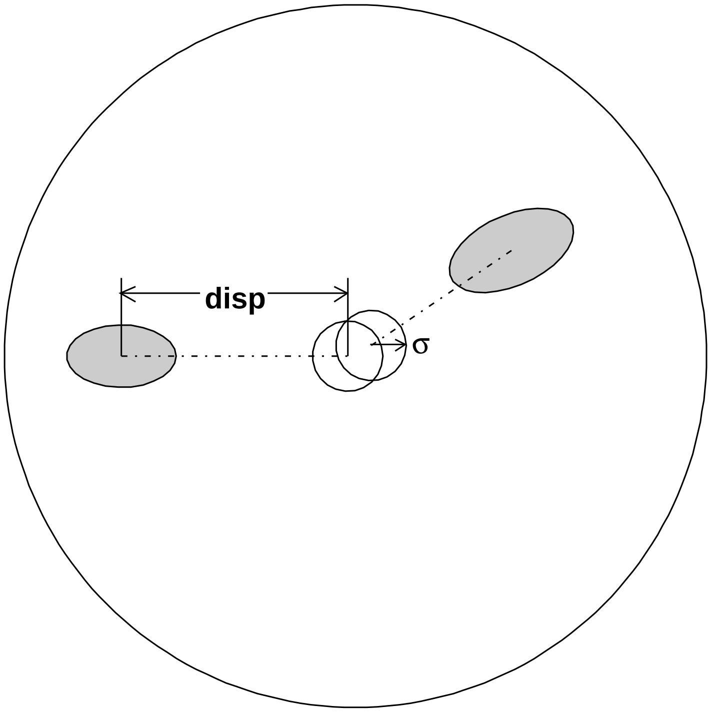

Figure 3.9 The shaded ellipses represent the images of two gamma-ray events in the camera, and the unshaded circles represent the possible arrival directions of the primary particle. In order for two events to be considered part of the same burst, the areas of possible arrival directions must overlap.

Practically, this search is carried out by first selecting the gamma-ray like events and then stepping through them in time. For event i occurring at time t_i, all events occurring between t_i and $t_i + \Delta t$ are then selected. A search is then made for all the possible groups of events within that time-window that can also be fit within a circle of radius σ with each other. Actually, this search can be limited to only those groups of events that contain the i^{th} event, since any bursts that do not contain that event will also be contained in other time windows.

Given a group of n events, we determine whether they fit within the required circle by calculating the minimum radius r of a circle that can contain all n events. If $r < \sigma$, we say those events belong to the same burst. For $n = 2$, r is simply half the distance between the events. For $n = 3$, we have two different cases. If the events form an obtuse triangle, then a circle whose diameter is the longest side of that triangle will contain all three events, so r is half the largest distance between any two events. If the three points form an acute triangle, then the smallest circle that can contain them all is the one that circumscribes the triangle. It turns out that the case of $n > 3$ can be handled by computing r for all possible subsets of three events. The largest such r will be the minimum radius that can contain all n events (see appendix A for a proof of this).

Note that a given event may be found in many different bursts, both within the same time window and within different time windows. To avoid double counting, only a single burst size is kept for each event — the size of the largest burst containing that event. The number of bursts, N, of each size, b, is defined as the total number of events whose largest burst size is b, divided by b. This definition of $N(b)$ has the advantage that the total number of events $N_{tot} = \sum_{b=1}^{\infty} bN(b)$, which is the normalization one would expect for a reasonable definition of the number of bursts of size b. Note that due to the possibility of an event being contained in multiple bursts, in some cases $N(b)$ will not be an integer.

3.2.5 Estimating the Background

Even in the absence of bursting sources, bursts are still observed due to random fluctuations in the rate of background events. To estimate the number of background bursts, the same method as in reference (25) is used. First the time stamps of the data are scrambled, and then the gamma-ray-like events are selected. The same burst search algorithm described above is then used; however, since the times are now essentially random, any real bursts caused by astrophysical phenomena are removed, leaving only the statistically generated bursts. This entire procedure is repeated ten times and the average results are taken as the background.

The difficulty in analytically calculating what the background should be given the event rate is that the camera is inhomogeneous. Different areas of the camera are more sensitive than others which leads to an artificial spacial clustering of events. In addition, clustering may be introduced by any nonuniformities in the sky brightness or by the presence of steady TeV gamma-ray sources. The advantage of the above method for estimating the background is that all these factors are automatically accounted for.

3.2.6 Detector Response

We now wish to be able to compare the number of detected bursts with what would be expected from a population of PBHs. The first step in this process is determining the Whipple 10 m's response to a hypothetical source. One key component to this calculation is the derivation of the effective collection area of the telescope. This is determined by simulating a uniform distribution of gamma rays within a radius r_s of the telescope for each of the Whipple camera configurations at various zenith angles and energies. The value of r_s is varied from 255 m to 500 m depending on the zenith angle of the simulation. Candidate gamma-ray events are then selected using the same criteria as for the real data. The collection area is then just the fraction of events selected multiplied by πr_s^2. Plots of the collection area as a function of energy for different camera configurations and zenith angles are given in Fig.s 3.10 and 3.11 respectively.

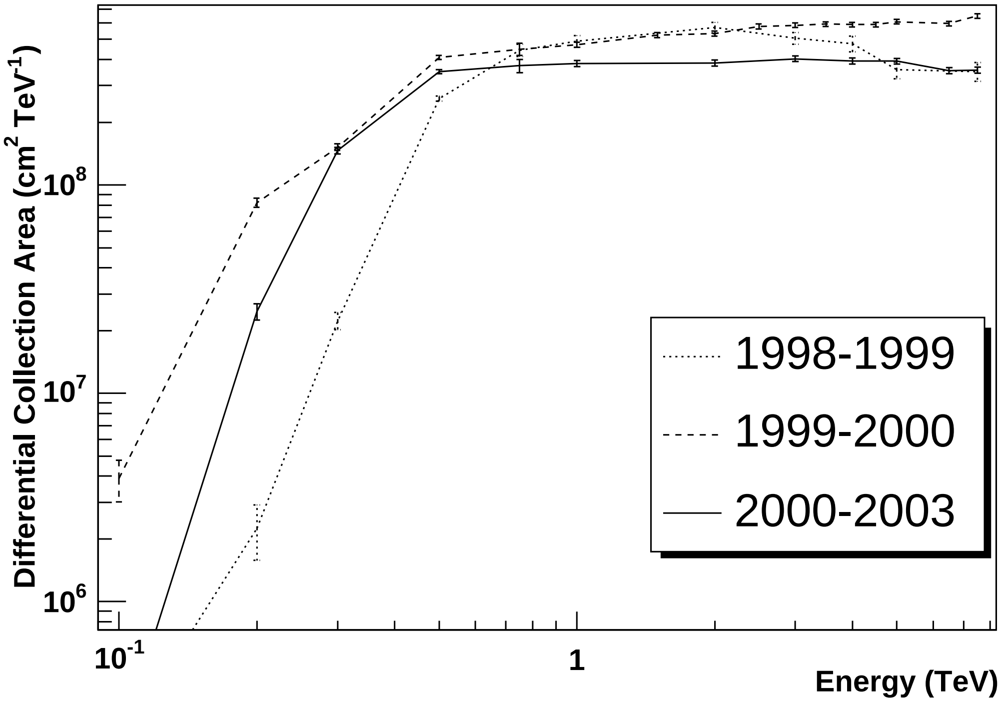

Figure 3.10 Differential collection area, dA/dE, vs. energy for zenith angle = 0° for three different camera configurations.

The zenith angle dependence of the collection area comes from the fact that at larger zenith angles, the amount of atmosphere between the telescope and the initial interaction point of the primary particle is greater. Thus, the Čerenkov light from the shower has more time to spread out before being detected. For lower energy showers, the light becomes too diffuse to trigger the detector, raising the telescope's energy threshold. However, for showers with enough energy to still be detected, the lightpool they produce is larger, increasing the collection area. These effects can be seen in Fig. 3.11. Because of these varying rates, the data are grouped into three zenith angle bins with the first bin consisting of zenith angles less than 20°, the second extending from 20° to 40°, and the third including zenith angles greater than 40°.

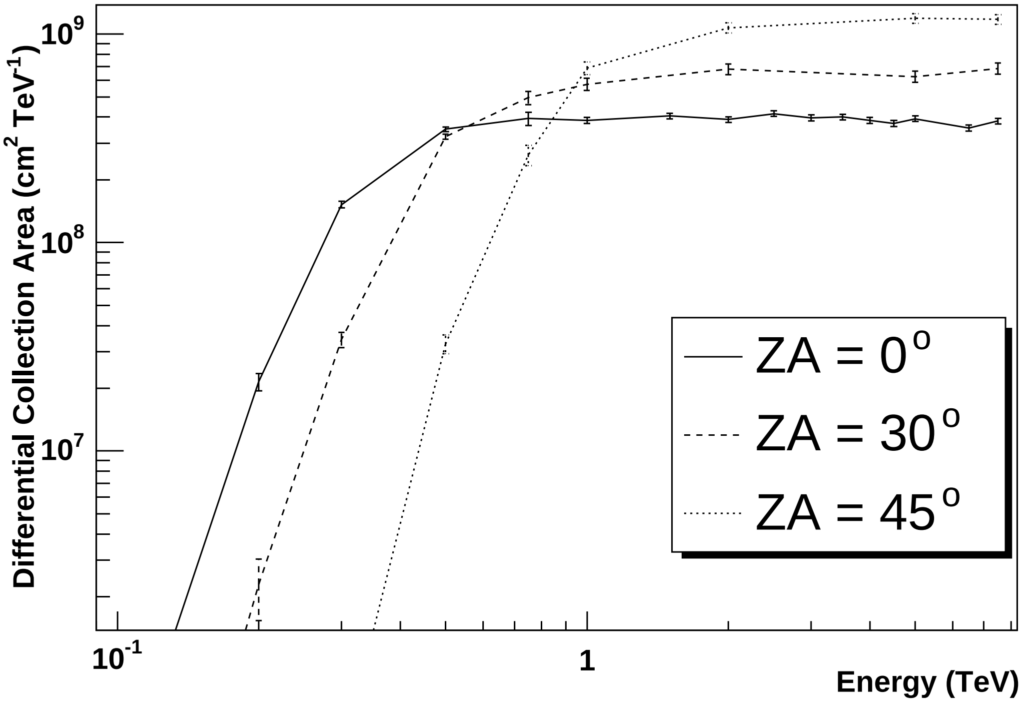

Figure 3.11 Differential collection area, dA/dE, vs. energy for various zenith angles (ZA) using the 2000-2003 camera configuration.

The collection area along with the gamma-ray production rate of a PBH will determine $N_D(r, \theta, \Delta t)$, the expected number of gamma rays to be detected from a PBH at distance r and angle θ from the optical axis of the telescope over the final Δt seconds of the PBH's life. Integrating over time and energy, we have

$$N_D(r, \theta, \Delta t) = \frac{1}{4\pi r^2} \int_0^{\Delta t} dt \int_0^{\infty} dE \frac{d^2N}{dEdt}(E, t) A(E, \theta), \tag{3.41}$$

where $N(E,t)$ is the number of photons produced by a PBH at energy E and time t before total evaporation. This expression can be simplified if we assume that the energy and θ dependence of the collection area can be factored out so that $A(E,\theta) = A_\circ(E)a(\theta)$, where $a(\theta)$ is the same as defined in section 3.2.3, and for $A_\circ(E)$ we use the collection areas calculated above. Thus, we obtain a different result for each camera used and each zenith angle bin. We now have,

$$N_D(r,\theta,\Delta t) = \frac{a(\theta)}{4\pi r^2}\int_0^{\Delta t} dt \int_0^{\infty} dE \frac{d^2N}{dEdt}(E,t)A_\circ(E) \equiv \frac{a(\theta)}{4\pi r^2}I, \tag{3.42}$$

where all the PBH physics has been moved into the factor I. Keeping this factor separate makes it easier to recalculate the expected signal for different PBH evaporation models.

The probability of observing a burst of b events within a time window Δt from a PBH at coordinates r and θ depends only on $N_D(r,\theta,\Delta t)$ and b. Calling this probability $P(b, N_D(r,\theta,\Delta t))$ and integrating over space, we find the total number of bursts of size b:

$$n_s(b,\Delta t) = \rho_{pbh}\tau \int d\Omega \int_0^{\infty} dr r^2 P(b, N_D(r,\theta,\Delta t)), \tag{3.43}$$

where τ is the total observation time. In the previous search (25), $P(b,N_D)$ is taken to be $\Theta(N_D(r,\theta,\Delta t) - b)$, where $\Theta(x)$ is the usual Heaviside step function. That is, all PBHs within a radius, $r(b,\theta,\Delta t)$, are assumed to produce exactly one burst of size b. In this work we set $P(b,N_D) = \exp(-N_D)N_D^b/b!$, since a Poisson distribution should give a more realistic description of the chances of detecting a PBH burst of a given size. A similar approach is used in reference (26). Substituting this back into equation 3.43, we now have for the expected number of PBH signal counts,

$$n_s(b,\Delta t) = \frac{\rho_{pbh}\tau}{8\sqrt{\pi}}\frac{\Gamma(b-3/2)}{b!}I^{3/2}\int_{-1}^{1} d\cos\theta a(\theta)^{3/2}. \tag{3.44}$$

Values of the integral over θ for the various camera configurations can be found in table 3.3. We can now estimate the distance out to which the search in this work is sensitive by setting N_D in equation 3.42 to 1 and solving for r. Using the results of section 3.1.2 and the collection area versus energy curve for the 2000-2003 camera at ZA $= 0°$, we find $I = 4.2$ pc^2. Setting $a(\theta) = 1$ for an on-axis source gives $r = 0.58$ pc, thus justifying the neglect of cosmological redshifting and absorption of gamma rays by extragalactic background light in the above calculations.

Table 3.3 The angular offset dependent part of $n_s(b,\Delta t)$ for the different cameras.

Season	Camera	$\int_{-1}^{1} d\cos\theta a(\theta)^{3/2}$
Spring ‘98 - Spring ‘99	331 pixel	19.18×10^{-5}
1999-2000	379 pixel	8.78×10^{-5}
2000-2003	379 pixel	7.88×10^{-5}

3.2.7 Calculating Significances

In order to determine the significance of any measured excess over the background, a maximum-likelihood analysis is used. We let $M(n_m|x)$ be the probability of measuring n_m bursts given an expected rate of x, and $B(n_b|y)$ be the probability of having a background of n_b bursts given an expected rate of y. The likelihood function is then given by,

$$\begin{aligned}\lambda(n_s|n_m,n_b) &= \int_0^\infty dx \int_0^\infty dy M(n_m|x)B(n_b|y)\delta(x-y-n_s) && (3.45)\\ &= \int_0^\infty dy M(n_m|y+n_s)B(n_b|y). && (3.46)\end{aligned}$$

Assuming Poisson distributions, we have,

$$M(n_m|x) = \exp(-x)\frac{x^{n_m}}{n_m!} \tag{3.47}$$

$$B(n_b|y) = \beta\exp(-\beta y)\frac{(\beta y)^{\beta n_b}}{(\beta n_b)!}, \tag{3.48}$$

where β is the number of repetitions used when averaging the background. The expected distribution of probabilities can be determined by using the standard maximum-likelihood result,

$$\chi^2(n_s) = 2\ln\left(\frac{\lambda_{max}}{\lambda(n_s|n_m, n_b)}\right), \tag{3.49}$$

with λ_{max} being the maximum value of $\lambda(n_s|n_m, n_b)$ for a given n_m and n_b.

A test of these formulas is made by taking about 6 hours of data and generating 500 random data sets by scrambling the times just as has been done for the background. Backgrounds are then determined using the method described above (sec. 3.2.5) and equation 3.45 is used on each set to calculate the probability that $n_s = 0$. Figure 3.12 shows a plot of the distribution $\chi^2(0)$ calculated from different time scramblings of the data compared to the expected χ^2 distribution with one degree of freedom. It can be seen that the two are in good agreement. Thus, upper and lower limits can be set on the signal by finding the value of n_s that gives the χ^2 corresponding to the desired probability. Equation 3.44 can then be used to convert the likelihoods of n_s into likelihoods of ρ_{pbh}.

For larger burst sizes ($b > 7$) no bursts are detected, meaning $n_s = n_b = 0$. In this case equation 3.45 simplifies to

$$\lambda(n_s|n_m = 0, n_b = 0) = \frac{1}{2}\exp(-|n_s|). \tag{3.50}$$

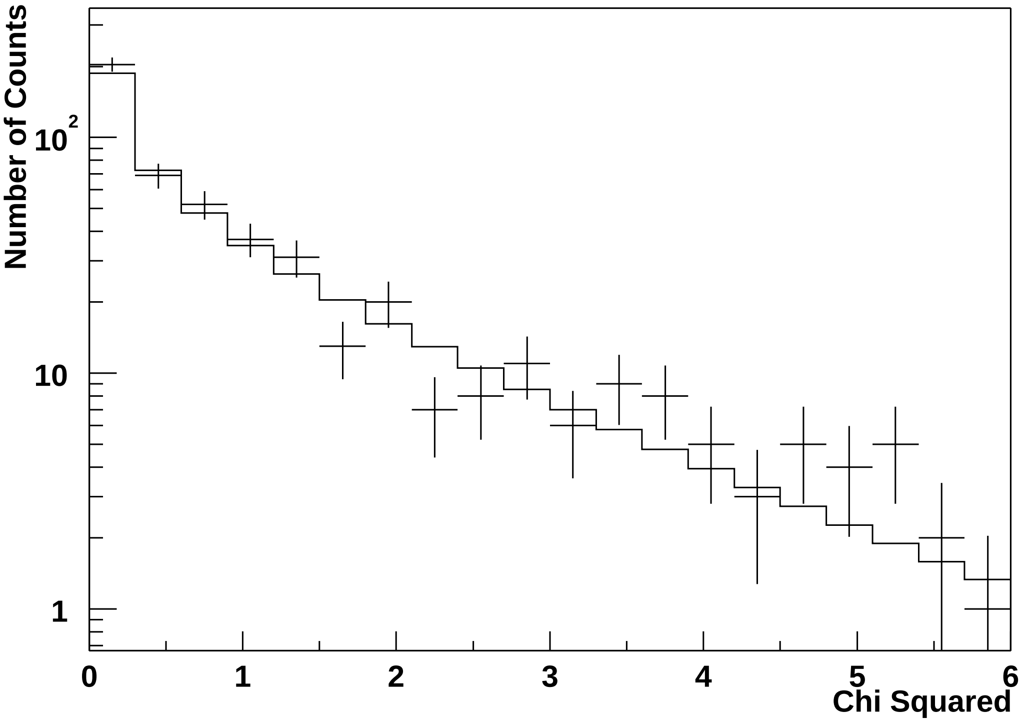

Figure 3.12 Plot of the χ^2 distribution calculated for 500 different time-scrambled signals (crosses) and the theoretical χ^2 distribution (solid line).

When this formula holds, it is possible to sum the log-likelihoods for a given ρ_{pbh} analytically. Using equations 3.44 and 3.50 we have

$$\sum_{b=2}^{b=\infty} \ln\left(\frac{\lambda_{max}}{\lambda(n_s)}\right) = \sum_{b=2}^{b=\infty} |n_s| \tag{3.51}$$

$$= \frac{\rho_{pbh}\tau}{8\sqrt{\pi}} I^{3/2} \int_{-1}^{1} d\cos\theta a(\theta)^{3/2} \sum_{b=2}^{b=\infty} \frac{\Gamma(b-3/2)}{b!}. \tag{3.52}$$

The sum can be computed by using the power-series relation

$$\frac{4\sqrt{\pi}}{3}(1-x)^{3/2} + 2\sqrt{\pi}x - \frac{4}{3}\sqrt{\pi} = \sum_{b=2}^{b=\infty} \frac{\Gamma(b-3/2)}{b!} x^b. \tag{3.53}$$

Setting $x = 1$, we find

$$\sum_{b=2}^{b=\infty} \frac{\Gamma(b-3/2)}{b!} = \frac{2}{3}\sqrt{\pi}. \tag{3.54}$$

In general, bursts will be seen for small values of b, so it is necessary to be able to adjust the lower limit and sum only over those values of b for which there are no measured bursts. This can be done by simply computing the first few terms directly and subtracting them from the above result.

3.3 Results

For Δt's of 1 s, 3 s, and 5 s, the number of candidate bursts of various sizes, $n_m(b)$, is measured. Bursts containing up to seven events are seen, but there is no significant excess over the background (Fig. 3.13). For these bursts, equations 3.45 through 3.48 are used to calculate the likelihoods of the actual number of bursts, $\lambda(n_s)$, and equation 3.44 is used to convert these into likelihoods of PBH densities, $\lambda(\rho_{pbh})$. For larger burst sizes, equations 3.51 and 3.54 are used. The $-\ln(\lambda(\rho_{pbh}))$ for various camera configurations, burst sizes, and elevations are added and equation 3.49 is used to find the 95% and 99% limits on ρ_{pbh} (Fig. 3.14). The log-likeloods from different Δt values are not added together since they are calculated from the same data sets and, consequently, are not independent. The systematic uncertainty in the limits are estimated by adjusting the gain of the telescope in the collection area simulations by 20%. This leads to a systematic uncertainty of about 30%.

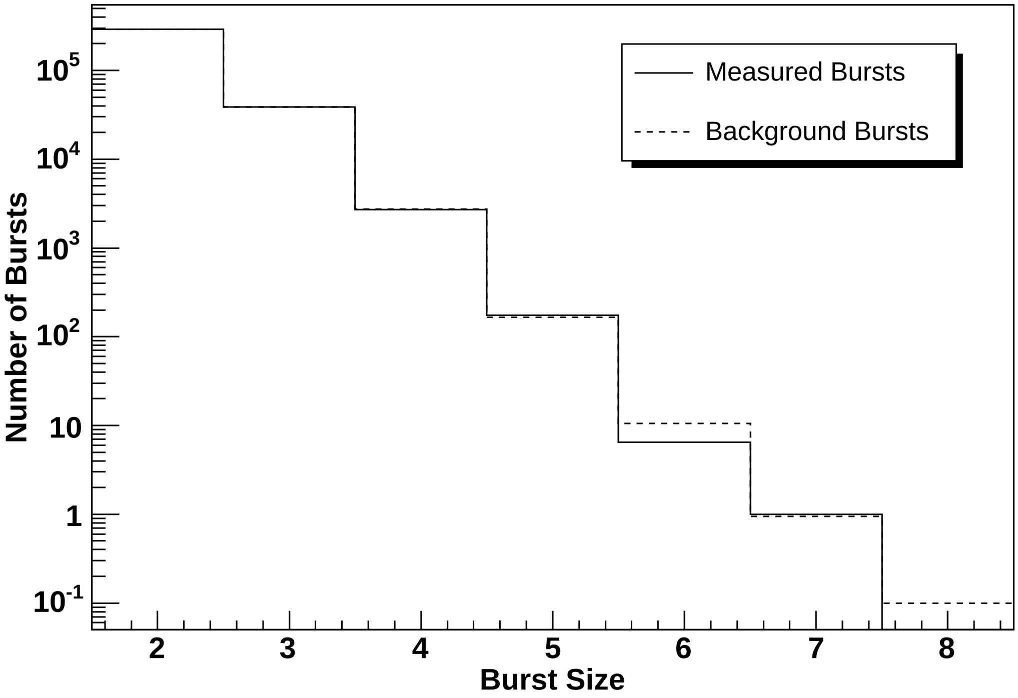

Figure 3.13 Number of bursts versus burst size for both the measured and background data. These data are for the most recent configuration of the 379 PMT camera with ZA < 20° and a time window of 5 s.

The data are consistent with $\rho_{pbh} = 0$, so only upper limits are calculated (Table 3.4). Raw burst rates with no assumed theory are given in appendix B. This information, along with the collection area versus energy data given in appendix C, are sufficient for recalculating the limits assuming a different theoretical model.

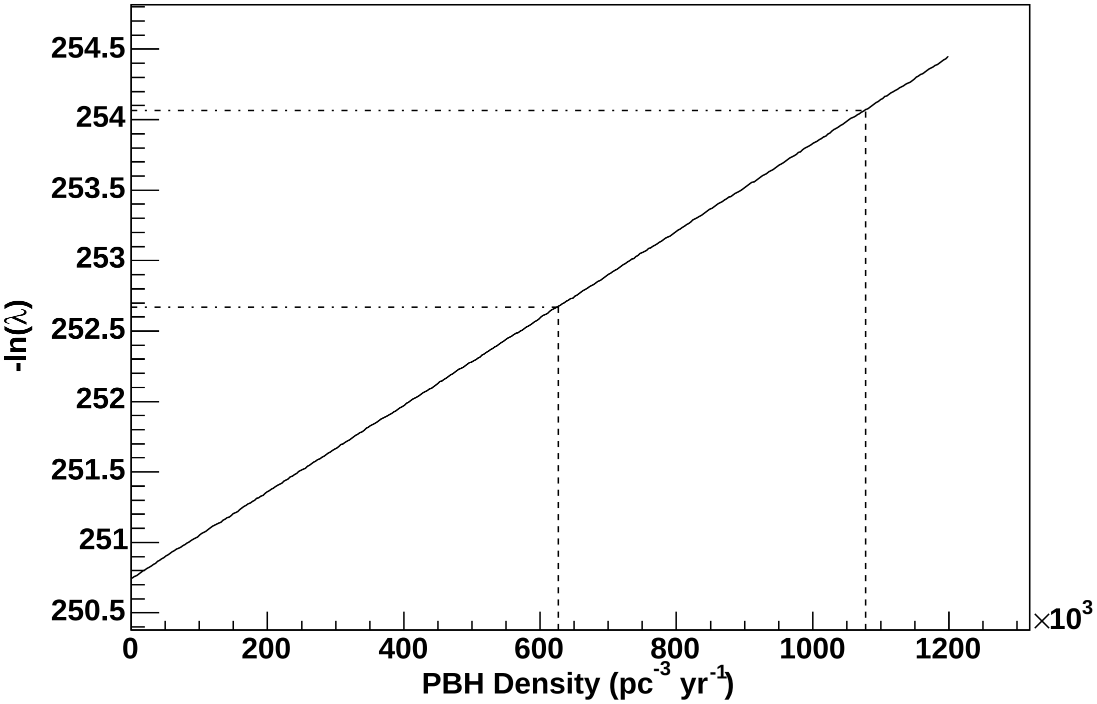

Figure 3.14 Plot of the negative of the log-likelihood of ρ_{pbh} vs. ρ_{pbh} for $\Delta t = 5$s (solid line). The lower (upper) horizontal line corresponds to the 95% (99%) χ^2 limit. The vertical lines indicate the limits on ρ_{pbh} corresponding to the appropriate χ^2 values.

Table 3.4 The 95% and 99% upper and lower limits on ρ_{pbh} in units of $10^6\mathrm{pc}^{-3}\mathrm{yr}^{-1}$.

Δt (s)	95% Upper Limits	99% Upper Limits
1	1.00	1.72
3	0.94	1.59
5	0.63	1.08

3.4 Discussion

3.4.1 Comparison with Previous Results

Five and a half years of Whipple data have been searched for second-scale TeV gamma-ray bursts. No evidence for such bursts has been found, leading to an upper limit on ρ_{pbh} of $1.08 \times 10^6\mathrm{pc}^{-3}\mathrm{yr}^{-1}$ (99% CL). The limit set in this work is more than a factor of two lower than the limit of $2.6 \times 10^6\mathrm{pc}^{-3}\mathrm{yr}^{-1}$ (99% CL) set in the previous search through Whipple data (25). However, that limit was set using gaussian statistics, so no use could be made of the fact that no bursts containing more than four events were seen. Applying the statistical methods described section 3.2.7 to the data in reference (25) yields a limit of $1.84 \times 10^6\mathrm{pc}^{-3}\mathrm{yr}^{-1}$, which is comparable to the $\Delta t = 1$ s limit in this work. Thus, the expansion of the time window to 5 s is key to lowering the limit. Combining the results from this search with the previous Whipple search yields an upper limit of $0.69 \times 10^6\mathrm{pc}^{-3}\mathrm{yr}^{-1}$.

Figure 3.15 places this result within the context of other direct PBH searches. The ACT limits are comparable to those set by the air-shower measurements of the Tibet array at $\sim$ 10 TeV (27) and CYGNUS at $\sim$ 50 TeV (26). However, they explore both a lower energy range and longer time scales, making them a useful complement. One example of how these results at different energy ranges can be used together has already been discussed in section 3.1.4. Namely, the existence of a phase transition

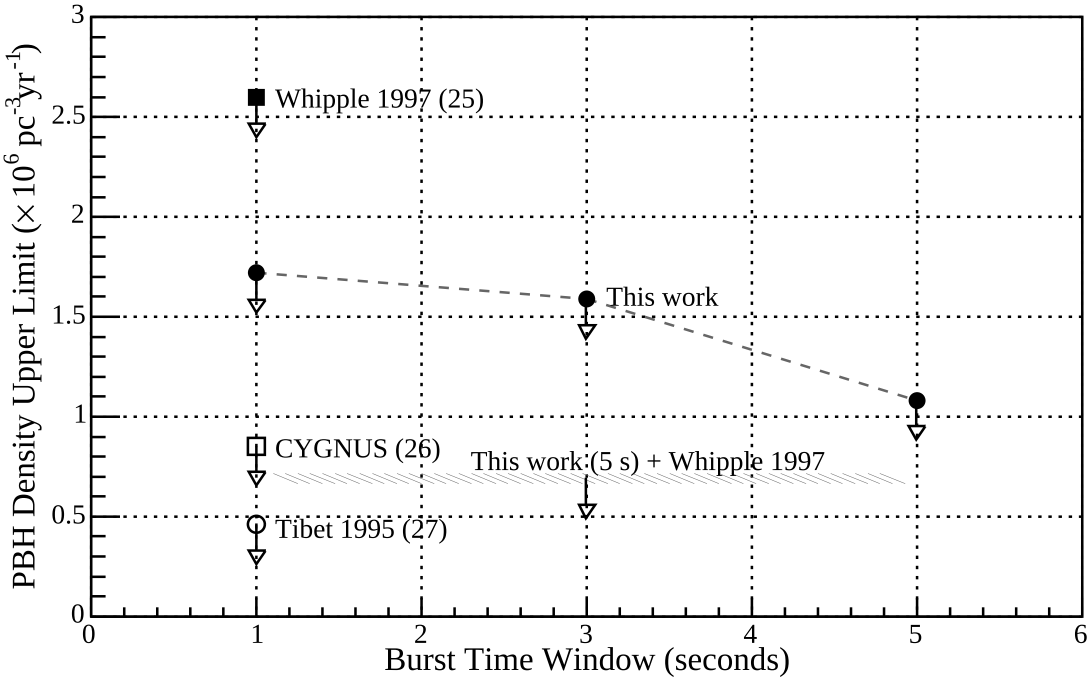

Figure 3.15 Upper limits on PBH density from direct burst-search experiments.

at an energy Λ as defined in equation 3.37 will cause the relative sensitivities of the various experiments to change. Figure 3.16 compares the effects of a hypothetical phase transition at various energies on both the results of this work and the limit set by the Tibet experiment (27). For Λ less than about 1 TeV, the Whipple limits are more stringent than the Tibet limit despite the fact that they are higher when assuming only the Standard Model particles.

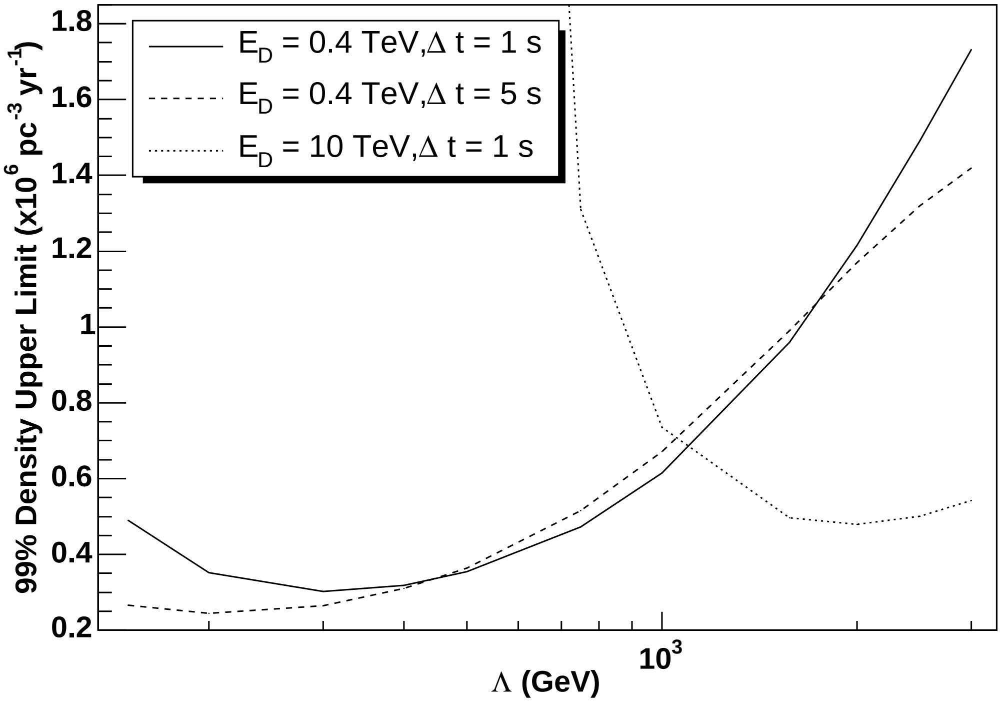

Figure 3.16 The 99% confidence upper limits on the PBH density as a function of the energy scale, Λ, of a hypothetical phase transition in the spectrum of particle species. Hypothetical results are given for the $\Delta t = 1$ s and $\Delta t = 5$ s results of this work, and the 10 TeV threshold limit of reference (27).

Limits have also been placed on the PBH density by indirect approaches. For instance, measurements of the extragalactic, diffuse MeV gamma-ray background by the EGRET experiment have been used to set a limit on the fraction of the critical density comprised by PBHs of $\Omega_{pbh} < 3.3 \times 10^{-9}$ (28). This is done by integrating the expected signal from a uniform distribution of PBHs over their lifetimes and demanding that it lie below the observed background minus the portion that has already been accounted for by other sources. Since the universe is fairly transparent to photons at these energies, this approach is sensitive to the cosmological, rather than local, distribution of PBHs, which is why the limit is quoted in terms of Ω_{pbh}.

To convert between these two limits, a number of assumptions must be made. The first is an assumption as to the initial mass spectrum of PBHs. Since those PBHs just finishing their evaporation today all started with similar initial masses, the end result depends only weakly on the assumed spectrum. Under the assumption that the amplitude of primordial density fluctuations is independent of mass (see section 3.1.4) we find (20)

$$\frac{dn}{dM_f} = AM^{-\beta}, \tag{3.55}$$

with

$$\beta = \frac{1+3w}{1+w} + 1. \tag{3.56}$$

Letting $w = 1/3$ for a radiation dominated universe at the time of the PBH formation, we have $\beta = 2.5$. Next, we integrate over the number of PBHs that will evaporate within a time Δt at the present time to find the number of evaporations per unit time, per unit volume:

$$R = \frac{\zeta}{\Delta t}\left(\frac{at_f}{at_o}\right)^3 A \int_{m_f(t_o)}^{m_f(t_o+\Delta t)} dm m^{-\beta}. \tag{3.57}$$

Here $a(t_f)$ and $a(t_0)$ are the scale factor of the universe at the time when the PBHs formed and today, respectively. The function $m_f(t)$ represents the formation mass of a PBH that is just evaporating at time t. Recall, $m(t_o)$ was found to be 4.74×10^{14} g in section 3.1.4. The greatest theoretical uncertainty comes from the parameter ζ, which is ratio of the local PBH density to the average PBH density. If PBH clustering in galaxies follows dark matter clustering, then ζ will be about 8×10^5 (29). However, recent work shows that PBHs could have initially formed strongly clustered, resulting in ζ as high as 10^{22} (30). Given that Δt is so much less than the total PBH lifetime, equation 3.1 becomes

$$m_f(t_o + \Delta t) \approx m_f(t_o) + \frac{\alpha_f \Delta t}{m_f(t_o)^3}. \tag{3.58}$$

In this equation, α_f is defined as $\alpha[m_f(t_o)]$. Note, the second term in equation 3.58 is much smaller than the first, so the integral in equation 3.57 can be expanded to first order to get

$$R = \left(\frac{a(t_f)}{a(t_o)}\right)^3 A \frac{\alpha_f}{m_f(t_o)^{\beta+2}}. \tag{3.59}$$

The normalization A can be found using the fact that as a PBH evaporates, its mass remains roughly constant throughout most of its life and undergoes a very rapid decrease during the final stages of evaporation. Thus, we can make the approximation that the present mass of all PBHs with an initial mass greater than $m_f(t_o)$ is the same as the initial mass. Letting ρ_c be the critical density of the universe,

$$\Omega_{pbh} = \frac{1}{\rho_c} \left(\frac{a(t_f)}{a(t_o)}\right)^3 \int_{m_f(t_o)}^{\infty} dm A m^{1-\beta}. \tag{3.60}$$

We can now relate R directly to Ω_{pbh}:

$$R = \frac{(\beta - 2)\rho_c \alpha_f \zeta}{m_f(t_o)^4} \Omega_{pbh}. \tag{3.61}$$

Depending on the value of ζ, the EGRET limit on the PBH evaporation rate could lie anywhere in the range of 2×10^{-2} pc^{-3} s^{-1} to 2×10^{14} pc^{-3} s^{-1}. Due to this large uncertainty, the upper limits of these two experiments cannot really be compared in a sensible way. If, however, one of the local PBH searches should actually succeed in measuring the PBH evaporation rate, this could be combined with the EGRET upper limit to place a lower bound on ζ.

Another indirect limit on the PBH density has been set by noting the absence of antiprotons below the kinematic production threshold in interstellar collisions in data from the BESS balloon experiment (29). Their limit of $\rho_{pbh} < 2.00 \times 10^{-2}\text{pc}^{-3}\text{yr}^{-1}(90\%\text{CL})$ is dependent on a number of theoretical assumptions. For instance, since anti-protons carry charge, they are susceptible to galactic magnetic fields. Thus, the calculation of the expected signal involves detailed simulations of how the particles travel through the galaxy, which are unnecessary when dealing with photons.

One of the fundamental differences between these indirect PBH experiments versus the direct searches is that the former can never report a positive detection. For instance, while the density of the diffuse MeV gamma-ray background gives an upper limit to the density of PBHs, it cannot be determined how much, if any, of the background we do see is in fact produced by PBHs. Such a determination would rely on a direct detection of a PBH by other means, such as the search carried out in this work.

3.4.2 VERITAS

New-generation Čerenkov telescopes will be better equipped to constrain the density of PBHs. One example is the Very Energetic Radiation Imaging Telescope Array System (VERITAS) currently under construction in southern Arizona. VERITAS will consist of 4 12-m telescopes, two of which are currently operational. The full array is scheduled for completion in Fall of 2006. Larger collection area, smaller angular resolution, and a lower energy threshold will all aid in searching for PBHs. Another new-generation telescope currently operating is HESS, located in the Khomas Highland of Namibia. HESS has shown that by placing tight cuts on their data, they can drastically reduce the cosmic-ray background triggers to almost zero, keeping the energy threshold at around 800 GeV using two telescopes (31).

These figures of zero background rate and an 800 GeV energy threshold can be used to make an estimate of VERITAS's ability to search for PBHs. Background rejection is made easier in a PBH search than in a general source search since the additional timing and angular-resolution constraints will aid in rejecting background events, so this estimate is somewhat conservative. In addition, when VERITAS begins running with 4 rather than 2 telescopes, its sensitivity will increase.

Using the no-background assumption and assuming zero signal, we can use equation 3.51 to estimate the limits obtainable with VERITAS. We convert the log-likelihoods to χ^2s with equation 3.49 and substitute $\chi^2 = 6.635$ for a 99% upper limit. We then find,

$$\rho_{pbh} = \frac{6\chi^2}{\int_{-1}^{1} d\cos(\theta) a(\theta)^{3/2}} I^{-3/2} \frac{1}{\tau} \approx \frac{39.81}{\int_{-1}^{1} d\cos(\theta) a(\theta)^{3/2}} I^{-3/2} \frac{1}{\tau}. \tag{3.62}$$

Next, a step function for $A_0(E)$ is assumed with a lower energy threshold of 800 GeV and a collection area of 10^9 cm^2, yielding $I = 11.56$ pc^2. An estimate for the integral of $a(\theta)$ is obtained by using $a(\theta)$ for the 2000-2003 camera configuration and rescaling θ by the ratio of the two cameras' FOVs, 3.5°/2.6°. This gives $\int_{-1}^{1} d\cos(\theta) a(\theta)^{3/2} = 15.04 \times 10^{-5}$, making the estimated 99% limit for VERITAS as a function of time

$$\rho_{pbh} \approx 2.12 \times 10^{11}\mathrm{pc}^{-3}\mathrm{yr}^{-1}\frac{1\mathrm{s}}{\tau}. \tag{3.63}$$

The total amount of time that can be spent on observations is limited by several factors. First, IACTs can only take data at night when the moon is not in the sky. In addition, the summer is monsoon season in southern Arizona and observations are not made during these months. Other factors, such as weather, can further reduce the time available for taking data. To get an idea of the fraction of time that is useful for a PBH search, we take the observation time used in this work, $\tau = 2,191$ hrs, and divide by the total time it spans, $t = 48,336$ hrs, to get $\tau/t = 0.045$. Using this factor to convert observation time to total time, equation 3.63 becomes

$$\rho_{pbh} \approx 1.49 \times 10^{5}\mathrm{pc}^{-3}\mathrm{yr}^{-1}\frac{1\mathrm{yr}}{t}. \tag{3.64}$$

Now it is easy to compare the estimated VERITAS performance with the limits set previously by the various other experiments (Fig. 3.17). Assuming no PBHs are detected, after 1 year of observation the VERITAS upper limit will be about a factor of 3 better than the current best air-shower array limit set by Tibet. Over the same 5.5 year period as used in this study, VERITAS will be able to set a limit over 40 times better than the one set with the Whipple telescope.

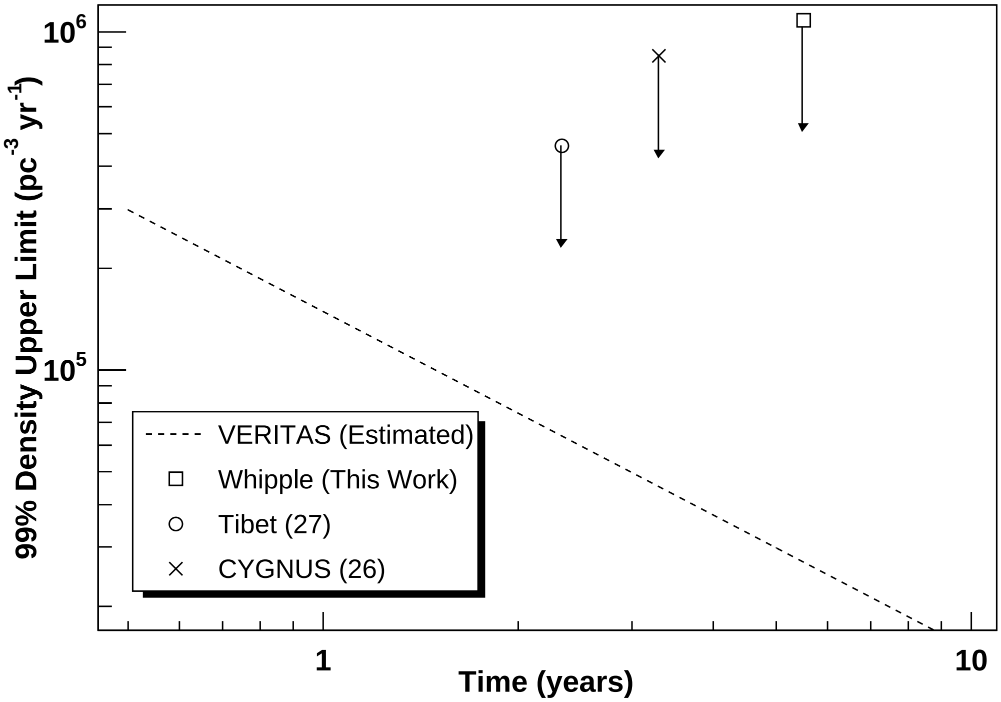

Figure 3.17 Estimated 99% upper limits obtainable with VERITAS versus the lifetime of the experiment. The $\Delta t = 5$ s limit set in this work along with the Tibet and CYGNUS upper limits are also shown.

CHAPTER 4

THE ENERGY SPECTRUM OF MARKARIAN 421

4.1 Markarian 421

4.1.1 General Properties of Active Galactic Nuclei

The active galactic nucleus (AGN) Markarian 421 was first reported as a source of TeV gamma rays in 1992 (32). This detection has since been confirmed (33), and it has now become one of the more important TeV gamma-ray sources due to its relatively close proximity to us ($z = 0.031$) and the strength of its TeV emissions when in an active state.

It is thought that AGN are powered by the accretion of matter onto supermassive black holes located at the center of their respective host galaxies. Using the velocity dispersion of the central stars in the host galaxy, the mass of Markarian 421's black hole has been estimated to be about $10^{8.28\pm0.11}$ solar masses (34). This accretion process produces very bright radiation over a wide band of the electromagnetic spectrum. Markarian 421 has long been known as a strong radio (35), optical (36), and x-ray (37) source, and in 1992 the EGRET experiment aboard the Compton Gamma-Ray Observatory detected MeV gamma rays from it (38).

Jets along the rotation axis of the black holes are believed to be the source of the TeV gamma-ray emissions. Due to this non-spherically-symmetric geometry, one would expect the appearance of an AGN to depend on the angle from which it is viewed. Indeed, it has been proposed that many of the differences between subclasses of AGN are caused by their different orientations relative to our own galaxy (39). Markarian 421 is classified as a blazar, which are characterized by strong polarization and high variability in the optical and a flat spectrum in the radio. In particular, it belongs to the BL Lac class, which have a featureless optical spectrum with very weak emission lines. The lack of spectral features is an indication that the jet of the AGN is aligned along our line of site so that our view is unobscured by the galactic disk.

BL Lacs can be further subdivided into high-energy cutoff and low-energy cutoff BL Lacs (HBLs and LBLs). The broad-band spectra of blazars consist of two peaks (Fig. 4.1). BL Lacs with the first peak in the radio are classified as LBLs, and those with the first peak in the x-rays are classified as HBLs. It is the latter category that have been detected at TeV energies, since the second peak can extend up to gamma-ray energies. The first peak is believed to be a product of electron synchrotron radiation, while the origin of the second is still not known for certain (see section 4.1.3).

4.1.2 Observed Spectral Properties of Markarian 421

One of the most striking features about the TeV gamma-ray emission from Markarian 421 is its rapid variability. Its signal strength can vary from being undetectable to being the brightest source in the sky at these energies. In May of 1996, two particularly rapid flares were observed that have allowed us to place strong limits on the properties of the emission region (40). The first occurred on the 7^{th} and saw the flux increase by a factor of at least 50 with a doubling time of about one hour. The second one on the 15^{th} lasted about 30 minutes with an approximately 20 fold increase in flux. Based on causality arguments, the size scale of the source is limited by the time scale of the most rapid flux variations. This relationship also depends on

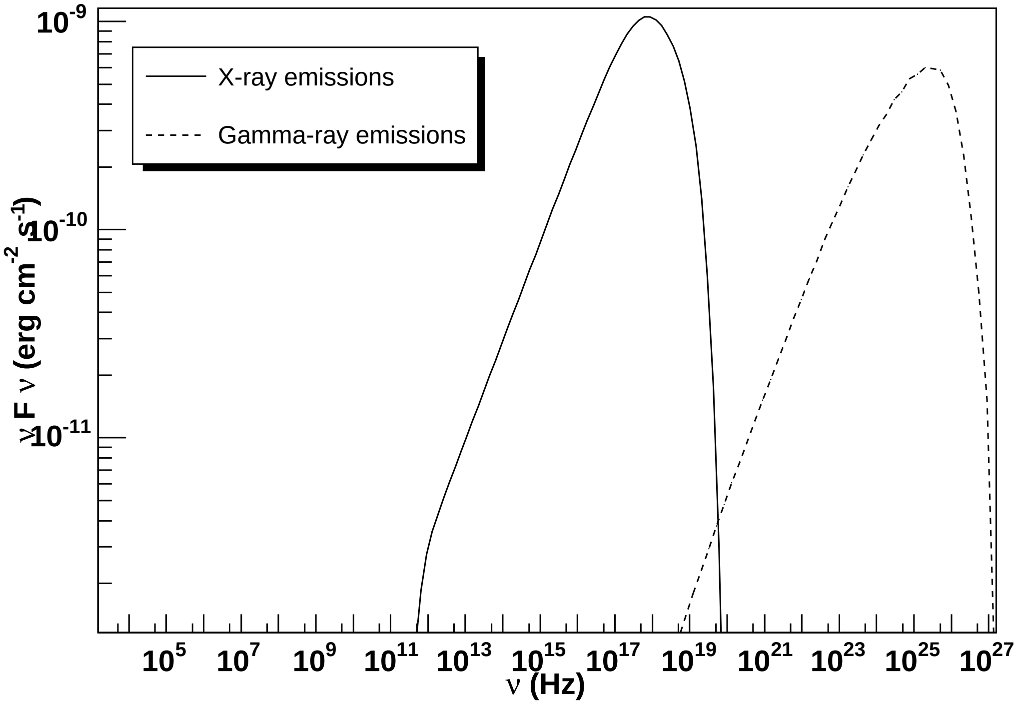

Figure 4.1 The two-peaked structure of the spectra of blazars. This figure shows a calculation using the synchrotron self-Compton model discussed in section 4.1.3.

the speed of the jet, which is characterized by the Doppler factor

$$\delta^{-1} = \gamma(1 - \beta\mathrm{cos}\theta). \tag{4.1}$$

Here, β and γ are the usual velocity and Lorentz factor of the jet, and θ is the angle of the jet to the observer. Taking into account the resulting time dilation effects and the redshift, z, of the source, we can constrain the size of the emission region with respect to the characteristic timescale, T, to be

$$R < cT\delta/(1+z). \tag{4.2}$$

Estimates of δ put it in the range of about 10 to 50. The lower limit comes from the fact that the observed density of photons at lower energies should produce an environment that is too optically thick to allow for the transmission of TeV photons. However, if the source is moving relativistically, then the density will be much lower in the source frame allowing the TeV photons to escape (41). The higher values for δ come from model fits to the energy spectra (see section 4.1.3). Jet components with such high velocities have not been seen at radio wavelengths (42), which means that either the jet is being rapidly decelerated, or the theoretical models need to be modified (43). Even with the higher Doppler factor, setting $T = 1$ hour yields a limit of $R < 50$ light hours, which is surprisingly small for the source of such energetic radiation.

The variability in the flux of TeV gamma rays provides greater information when compared with observations at other wavelengths. A number of studies have been performed comparing the flux of Markarian 421 in wavebands from radio through TeV gamma rays as a function of time (44; 45). The x-ray and TeV gamma-ray fluxes show strong evidence of being correlated with each other. The radio and optical fluxes show much less variability than the higher energy fluxes and do not show signs of strong time correlation.

One interesting feature that has been noticed in the TeV region of Markarian 421's spectrum is the presence of a cutoff around an energy of a few TeV (46). A strong flare in 2001 yielded a sufficiently large enough number of events to determine that the energy spectrum is not adequately described by a simple power law, but that an exponential cutoff must be added as well. Absorption by the extragalactic background light (section 4.1.4) is one possible source of this cutoff, although it is currently disfavored. Observations of the blazar Markarian 501 indicate a significantly higher cutoff energy for that source than for Markarian 421 (47). Since they are found at similar redshifts, external mechanisms are unlikely to be the cause of both cutoffs.

Measurements of the energy spectrum at various points throughout the 2001 season have revealed that it varies significantly as the flux levels change (48). In general, as the flux increases, the spectrum becomes harder. If it can be determined that the position of the energy cutoff is changing, then this would be a clear indication that intrinsic source properties are at least partially responsible for its presence. So far, however, measurements with sufficient precision to make this determination have not been made.

4.1.3 Production Mechanisms of TeV Gamma Rays

The source of the TeV emission from blazars is still debated, but there are some general properties shared by all the models due to the facts we have already learned. For instance, the presence of a relativistic jet is well established, as well as the existence of magnetic fields and a population of electrons to produce the observed x-ray emissions. The identity of the particles responsible for the TeV radiation, however, is still unknown. Existing models are divided into two classes — leptonic and hadronic — based on the particle employed to produce the TeV photons. Some of the general features of these are illustrated in figure 4.2.

Given the population of photons in the presence of highly energetic electrons that must be present to produce the synchrotron radiation, inverse Compton scattering of the photons by the electrons is a natural mechanism for accelerating them to TeV energies. Such models are known as synchrotron self-Compton (SSC) models due to the fact that the same population of electrons and photons are involved in both the synchrotron and inverse Compton emissions (49; 50). One of the main strengths of this model is that it explains the observed time correlation between the x-ray and gamma-ray signals. In addition, it also does a good job of describing the shape of the observed spectra. In the simplest SSC models relatively large Doppler factors of $\delta \approx 50$ are needed to produce adequate fits. This is viewed as a problem by some due to the lack of evidence for such strong Lorentz boosting at other wavelengths (see section 4.1.2), but can be solved by using two separate electron populations of different, but more moderate, Doppler factors (43). Another weakness of the SSC model is the observation of TeV flares with no corresponding x-ray flare in some AGN (51; 52), although several explanations for these within the SSC framework have been put forth.

Despite the general success of the SSC model, there still exist some viable hadronic models that cannot be ruled out as the source of the TeV photons (53; 54). The most promising of these is synchrotron radiation from protons. Two other models of note are that the TeV gamma rays come from the decay of π^0s produced by p-p interactions, or that proton interactions with synchrotron radiation produce gamma

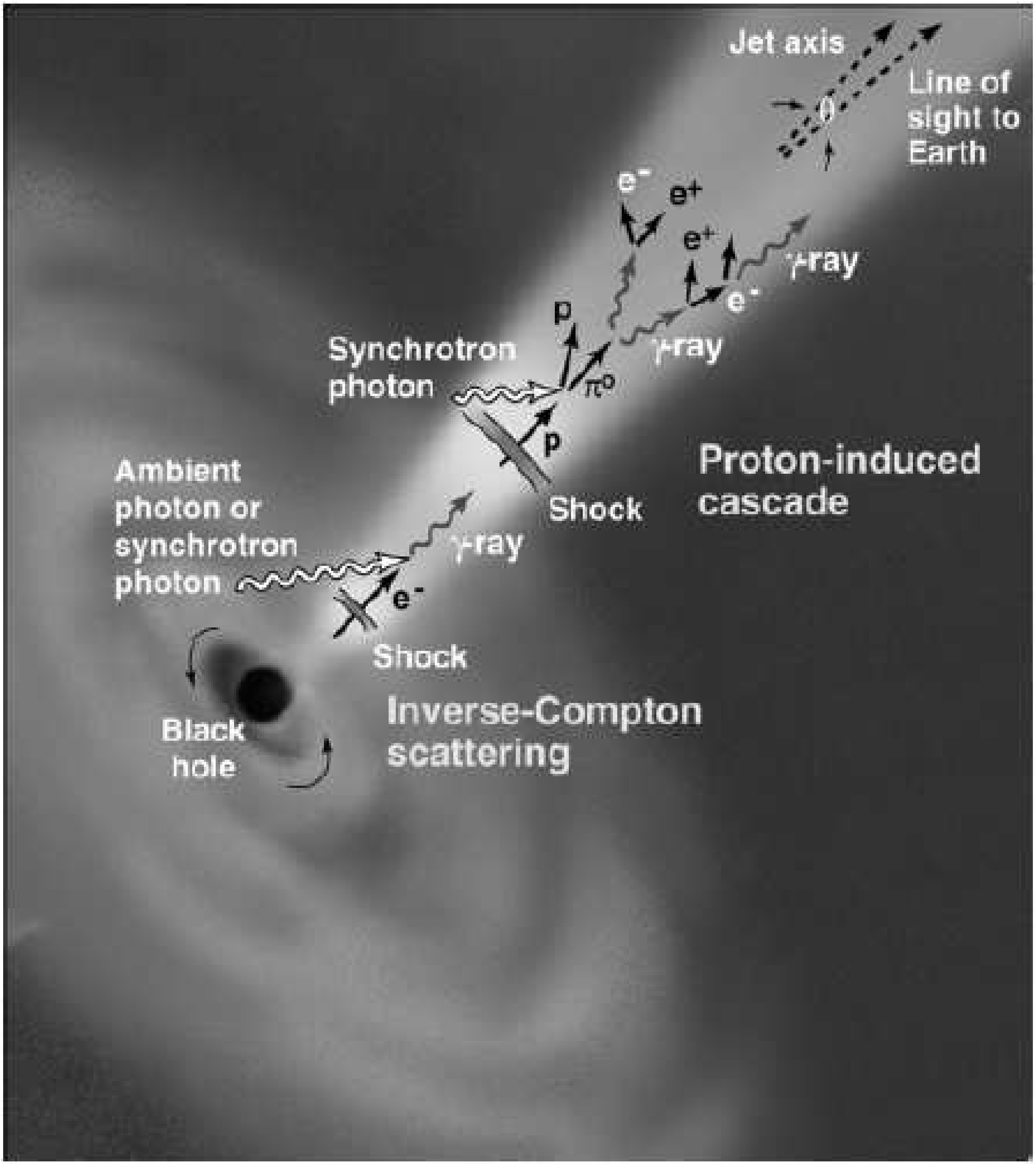

Figure 4.2 Illustration depicting the hadronic and leptonic production methods of TeV gamma rays in AGN.

rays and electrons that in turn initiate pair cascades. Both of these models suffer from the fact that they are very inefficient. The latter can be improved by increasing the magnetic field to $\gg 1$ G, but with such field strengths the synchrotron losses become a much more efficient mechanism for TeV gamma-ray production.

One of the motivating factors behind the proton-synchrotron model is that it could describe the relative stability of the shape of Markarian 501's (another TeV producing BL Lac) spectrum despite dramatic changes in its overall flux (53). However, this spectral stability assumes that synchrotron losses are the dominant source of energy loss. In order for this condition to be met and to allow for the sub-hour scale variability in Markarian 421, one would require an unreasonably large ($\gg 100$ G) magnetic field strength. If, on the other hand, particle escape or adiabatic cooling are allowed to dominate, then the spectrum of Markarian 421 in its most rapid flares can be fit with a more moderate magnetic field of ~ 100 G. In this model, spectral stability is no longer expected, which agrees with the spectral hardening that has been observed (see section 4.1.2).

In addition to the large magnetic field strengths, the proton-synchrotron model also requires the existence of a very energetic population of protons, with energies on the order of 10^{19} eV. Such accelration may be possible through shocks in the jet, but would push this mechanism to its limit. However, if protons are indeed being accelerated to such high energies, it might also be able to explain the origin of ultra-high-energy cosmic rays (55), which is a strong reason why the hadronic models are still of such interest despite the apparent success of the leptonic models.

The physical source characteristic that determines whether the SSC or proton-synchrotron model will be the dominant source of TeV radiation is the magnetic field strength. The typical field strength in SSC models is about 0.1 G, as compared to the ~ 100 G of the proton-synchrotron model. This can lead to an empirical method of distinguishing between the models, since in both the x-ray synchrotron photons are produced by electrons in a field of about 0.1 G. Thus in the proton-synchrotron model, the TeV and x-ray emissions come from different regions within the jet and the time correlation between flares at these two energies is not expected to be as tight as with the SSC model. Such a distinction will require many more simultaneous x-ray and gamma-ray observations of Markarian 421 to be made than have been done to date.

4.1.4 The Extragalactic Background Light

When looking at the transparency of the universe to TeV photons, the most important interaction to consider is that of two photons colliding to produce an electron-positron pair. The cross section for this process is given by (56)

$$\begin{aligned} \sigma(q) &= \frac{3}{8}\sigma_T f(q) && (4.3) \\ f(q) &= q\left[\left(1+q-\frac{q^2}{2}\right)\ln\frac{1+\sqrt{1-q}}{1-\sqrt{1-q}} - (1+q)\sqrt{1-q}\right] && (4.4) \\ q &= \frac{m_e^2}{E\varepsilon}\frac{2}{1-\cos(\theta)}. && (4.5) \end{aligned}$$

The parameter σ_T is the classical Thomson cross section, m_e is the electron mass, θ is the collision angle, and E and ε are the energies of the two photons. The function $f(q)$ reaches its maximum at $q = 0.508$, which means that the cross-section for a head-on collision is maximized for a TeV photon when the other photon has an energy of about 0.5 eV. Consequently, infrared photons are the dominant source of absorption for TeV photons.

The diffuse infrared background is important from a cosmological point of view because it contains much of the radiated energy produced by structure formation since the epoch of decoupling (57). Infrared photons are produced either directly or through the absorption and re-emission of shorter wavelength photons by dust clouds. Unfortunately, direct measurements of this radiation are extremely difficult due to the high foreground from sources within the solar system.

From one point of view, the large amount of uncertainty in the infrared background (commonly referred to as the extragalactic background light, or EBL, at $z = 0$) is a problem for TeV astronomers since it makes it difficult to disentangle absorption effects from the intrinsic spectra of sources. On the other hand, it provides an exciting challenge as studying the EBL's effect on TeV spectra may be the only way of obtaining a precise measurement of its intensity.

To see how this sort of indirect measurement might be accomplished, we first calculate the amount of absorption for TeV photons from any given model of the EBL following the procedure of reference (56). If we let $dn(\varepsilon)/d\varepsilon$ be the number of infrared photons per unit energy, per unit volume, then the absorption probability per unit pathlength for a photon of energy E is given by

$$\frac{d\tau}{dl} = \frac{3}{4}\sigma_T \int d\varepsilon \int_{x_o}^{1} dx x f\left(\frac{m_e^2}{xE\varepsilon}\right)\frac{dn(\varepsilon)}{d\varepsilon}, \tag{4.6}$$

$$x_o = \frac{m_e^2}{E\varepsilon}. \tag{4.7}$$

Making a substitution of variables in the second integral, we then have

$$\frac{d\tau}{dl} = \frac{3}{8}\sigma_T \int_{m_e^2/E}^{\infty} d\varepsilon \frac{dn(\varepsilon)}{d\varepsilon} F\left(\frac{m_e^2}{E\varepsilon}\right), \tag{4.8}$$

$$F(x) = 2x^2 \int_{x}^{1} dq q^{-3} f(q). \tag{4.9}$$

The final step is to integrate over the distance between the earth and the source at redshift z, which yields

$$\tau(E,z) = \frac{3\sigma_T c}{8H_o}\int_0^z dz' \frac{1+z'}{\sqrt{(1+z')\Omega_m + \Omega_\lambda/(1+z')^2}} \tag{4.10}$$

$$\int_{m_e^2/(1+z')^2 E}^{\infty} d\varepsilon \frac{dn(\varepsilon)}{d\varepsilon} F\left(\frac{m_e^2}{(1+z')^2 E\varepsilon}\right).$$

In this work we use the values $H_o = 0.71$ km s^{-1} Mpc^{-1} for the Hubble parameter, $\Omega_m = 0.27$ for the fraction of the critical density in matter, and $\Omega_\lambda = 0.73$ for the fraction of the critical density in dark energy. Once the absorption probability is known, the fraction of surviving photons at a given energy is simply $\exp[-\tau(E,z)]$.

As mentioned before, the density of the EBL is largely unknown, so we use the results of the semianalytic model found in reference (58). In this calculation, analytic models are used to calculate galaxy evolution and other processes that lead to the production and absorption of infrared radiation, while parameters like star formation rates and metallicity yields are set empirically using data from local galaxies. The resulting density distribution can be seen in figure 4.3. The most stringent upper limits on the EBL have been made by the HESS experiment by looking at the TeV gamma-ray signal from blazars at redshifts of $z = 0.165$ and $z = 0.186$ (59). These upper limits are in agreement with the model calculations used in this work.

4.2 Calculating the Energy Spectrum

4.2.1 Gamma-ray Selection Criteria

The efficiency of the standard gamma-ray selection criteria discussed in section 2.4 is highly energy dependent. Since sources tend to have spectra which fall off rapidly with

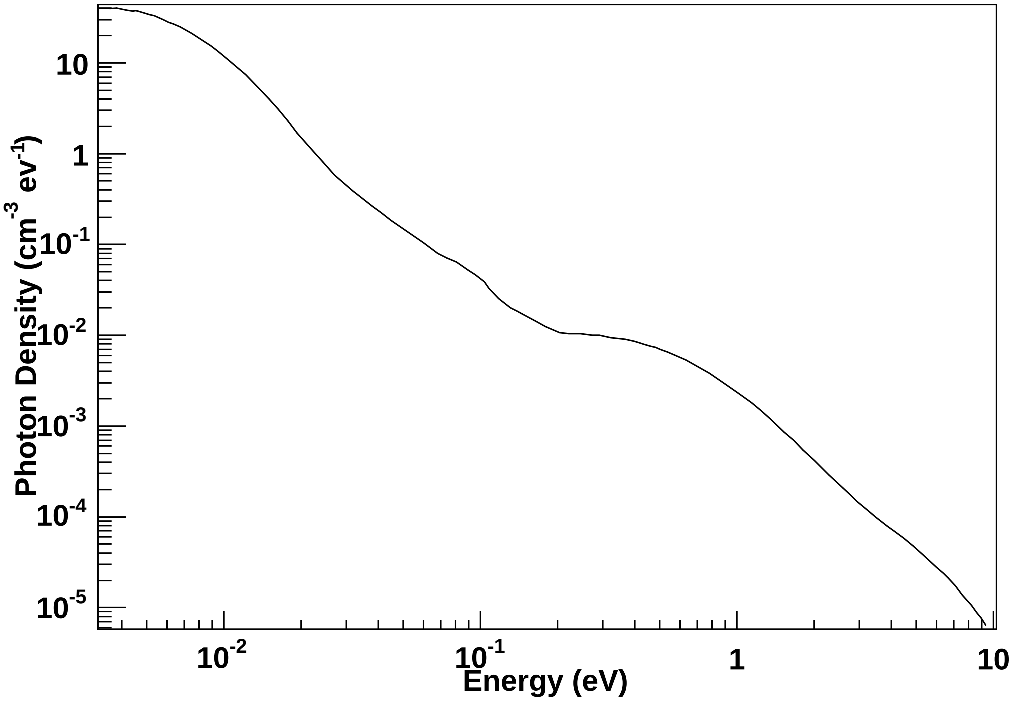

Figure 4.3 The density of the extragalactic background light as calculated by the semianalytic model in reference (58).

energy (generally power laws with a spectral index of ~ 2.5), this energy dependence is of little consequence for source detection. The selection criteria can simply be optimized to be most effective just above the detector's energy threshold where most of the gamma rays will be. In the study of energy spectra, however, it is desirable to have a detector response that is independent of energy to minimize the distortion of the spectrum. In addition, the spectral features one is interested in are often located at the higher energies (e.g. determining whether there is a cut-off in the spectrum) so it is crucial to detect as many higher energy photons as possible.

Consequently, a modified set of selection criteria that is applicable over a wider range of energies has been developed (60). The basic idea is to use the fact that the total amount of Čerenkov light produced in a shower is proportional to the energy of the primary particle. Thus, one would expect the *Size* parameter, which gives the total number of signal counts in a shower image, to provide a rough approximation of the primary particle's energy. A natural way to select gamma rays in a manner that is efficient over a larger energy range, then, would be to allow the criteria to vary with *Size*.

Simulations show that the parameters *Width* and *Length* have a roughly linear relationship with the logarithm of *Size* (Fig. 4.4). Thus, the criteria

$$|Width - m_w \ln(Size) - b_w| \leq \Delta_w, \text{and} \quad (4.11)$$

$$|Length - m_l \ln(Size) - b_l| \leq \Delta_l \quad (4.12)$$

are used as the requirements for the *Width* and *Length* parameters when selecting gamma-ray like events. Here m_i and b_i are determined from fits to simulations. The parameters Δ_i are determined from both real data and simulations in the following manner. A quality factor $Q = F_{on}/\sqrt{F_{off}}$ is defined, where F_{on} is the fraction of

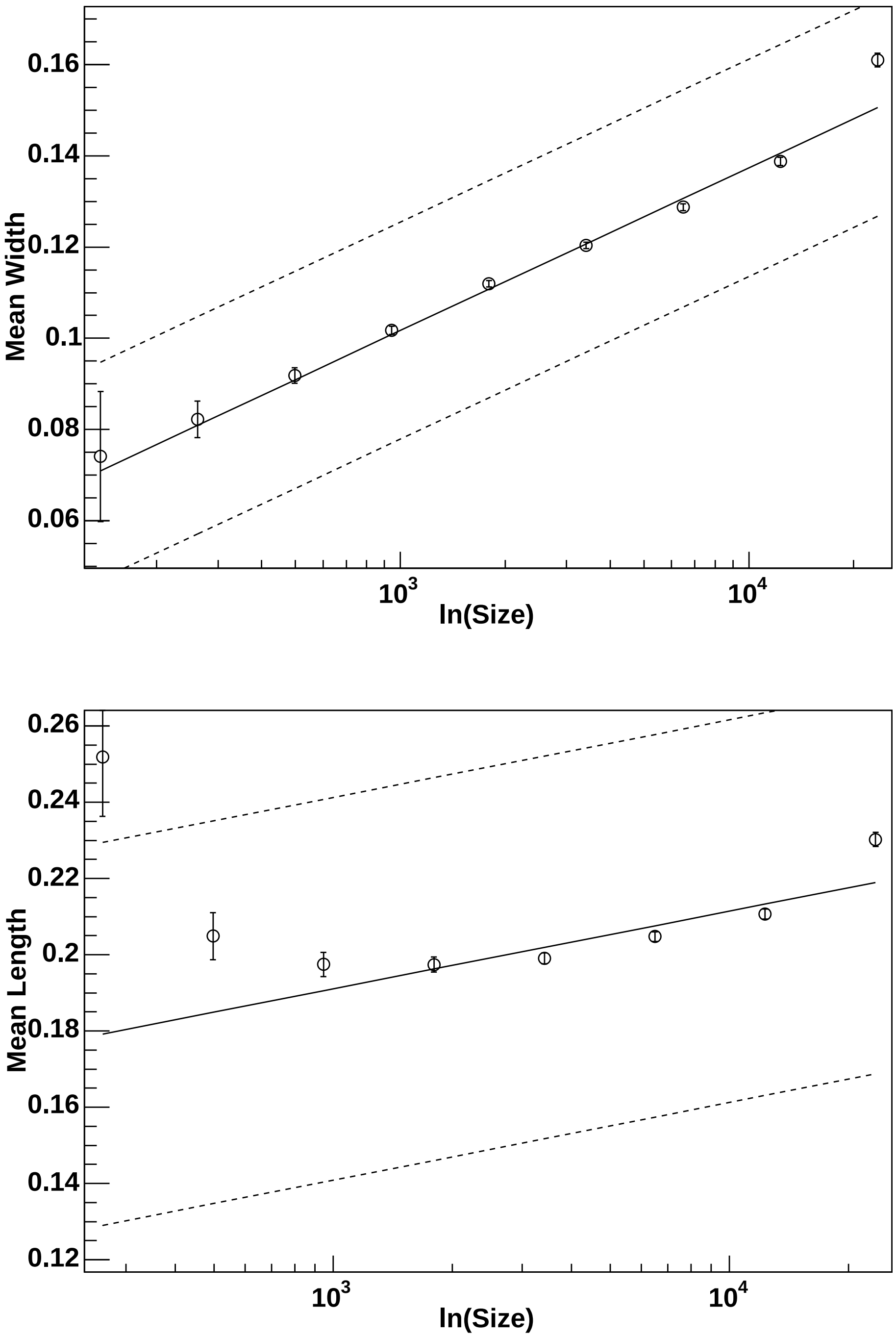

Figure 4.4 Plots of the *Width* and *Length* parameters of simulated events versus ln(*Size*). The solid lines give the fits to the data, and the dashed lines give the range of values accepted as being gamma-ray like.

simulated gamma-ray showers that survive the selection criteria, and F_{off} is the fraction of background events that survive. Actual off-source data are used for the background events. A grid search is then made through the parameters Δ_w and Δ_l to find the combination of values that maximizes Q. The resulting selection criteria found through this procedure, along with the standard selection criteria, are summarized in table 4.1. Assuming a power-law source spectrum with spectral index of 1.0, which yields an equal number of counts per logarithmic energy bin, the *Size*-dependent selection criteria have $Q = 5.0$ and the standard analysis has $Q = 3.4$. If a source spectral index of 2.5 is used, then the Q factors are 4.6 and 4.0 for the *Size*-dependent and standard analyses, respectively.

Table 4.1 Both the *Size* dependent and standard gamma-ray selection criteria used in this work.

Standard Selection Criteria	*Size*-dependent Selection Criteria
$0.05° < Width < 0.12°$	$\lvert Width - 0.0155\ln(Size) + 0.00540\rvert \leq 0.0238$
$0.13° < Length < 0.25°$	$\lvert Length - 0.00884\ln(Size) - 0.130\rvert \leq 0.0503$
$0.40 < Dist < 1.00$	$0.40 < Dist < 1.00$
$Max1 \geq 30$	$Max1 \geq 30$
$Max2 \geq 30$	$Max2 \geq 30$
$Length/Size \leq 0.0004$	$Length/Size \leq 0.0004$
$\alpha \leq 15°$	$\alpha \leq 15°$

Figure 4.5 compares the effective differential collection areas versus energy for both the *Size*-dependent and standard selection criteria. It can be seen that above about 800 GeV, the *Size*-dependent analysis produces a larger collection area than the standard analysis. This removal of the fall-off in collection area at higher energies is precisely the effect that we desired from the *Size*-dependent analysis.

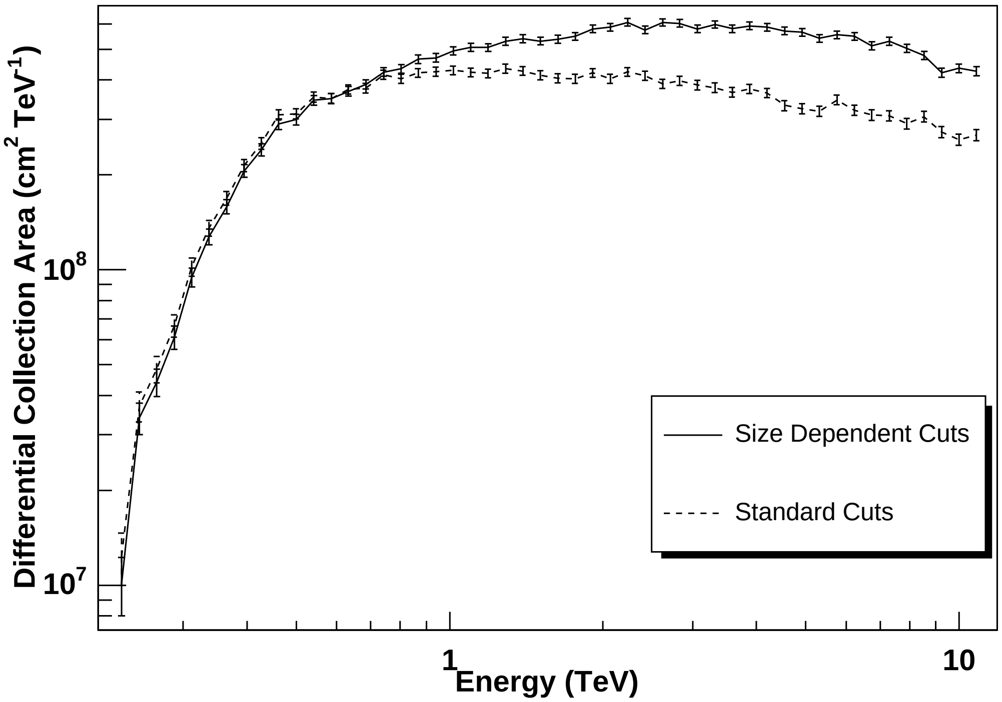

Figure 4.5 Plots of the differential collection area versus energy for both the standard gamma-ray selection criteria and the *Size*-dependent selection criteria.

4.2.2 Energy Estimation

Once gamma-ray like events have been selected, a method is needed to estimate the energy of these events from the measured parameters. Again, we follow the methods of reference (60). The amount of light from a given shower that falls on the detector depends on two factors: the total amount of light produced by the shower, which is directly related to the total energy of the primary particle, and the distance of the shower from the detector. Consequently, it is reasonable to estimate a shower's energy using a function of the parameters *Size*, which corresponds to the total light collected, and *Distance*, which corresponds to the impact parameter of the shower.

From simulations, it has been seen that the energy estimator

$$\tilde{x} = A_0(Distance)^3 + A_1 y^2 + A_2(Distance)^2 + A_3 y(Distance) + A_4 y + A_5(Distance) + A_6 \tag{4.13}$$

works well. Here, $\tilde{x}$ is the logarithm of the estimated energy, $\tilde{E}$, and $y = \ln(Size)$. The parameters A_i are found through optimizations with simulated data such that they minimize

$$\varepsilon^2 = \sum(\tilde{x} - x)^2, \tag{4.14}$$

where x is the logarithm of the actual simulated energy. This procedure can be carried out analytically by solving the set of seven linear equations:

$$\frac{\partial \varepsilon^2}{\partial A_i} = 0. \tag{4.15}$$

Note that due to the $i = 6$ equation, the bias, defined by $\sum(\tilde{x} - x)$, is automatically set to zero.

There is a choice as to what input spectrum to use for optimizing the data. Power-law spectra with spectral indices of 1.0 and 2.5 are used, and the results are given in table 4.2. Plots of $(\tilde{x} - x)$ are given in figure 4.6. As can be seen, the softer input spectrum produces estimation parameters that are more accurate in the 100s of GeV range, whereas the parameters derived with a spectral index of 1.0 are most accurate in the range of a few TeV. Since we are interested in features at higher energies, the parameters derived from the harder spectrum will be used in this work.

Table 4.2 Energy estimation parameters as defined in equation 4.13. Values derived using an input spectrum of 1.0 and 2.5 are given.

Spectral Index:	1.0	2.5
A_0	45.3	41.0
A_1	-0.0215	0.0165
A_2	-86.1	-79.9
A_3	-0.137	0.169
A_4	1.26	0.437
A_5	54.3	49.4
A_6	-18.8	-14.7

From the standard deviation of $\tilde{x}$ in each energy bin, the energy resolution of this technique can be found. Figure 4.7 shows the energy resolution as a function of energy using both the energy estimator derived with an input spectrum of 1.0 and the one derived with a spectrum of 2.5. Although the 2.5 index estimator yields a better energy resolution below 1 TeV, it becomes rapidly worse above this energy. The 1.0 index estimator, on the other hand, has a relatively uniform energy resolution with respect to energy.

4.2.3 Spectral Deconvolution

The energy spectrum obtained by simply applying the energy estimator discussed in the previous section to the measured signal will be distorted by the finite energy

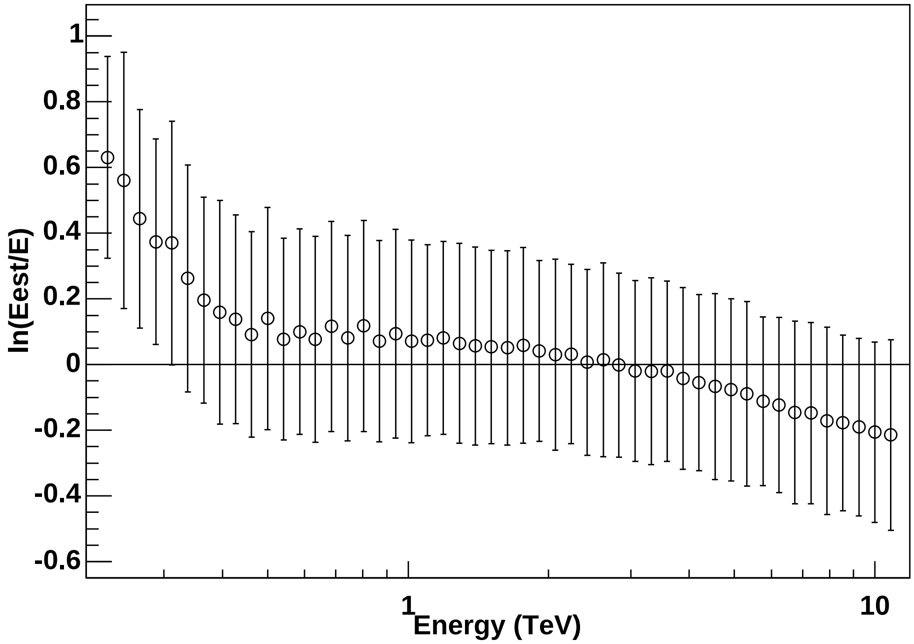

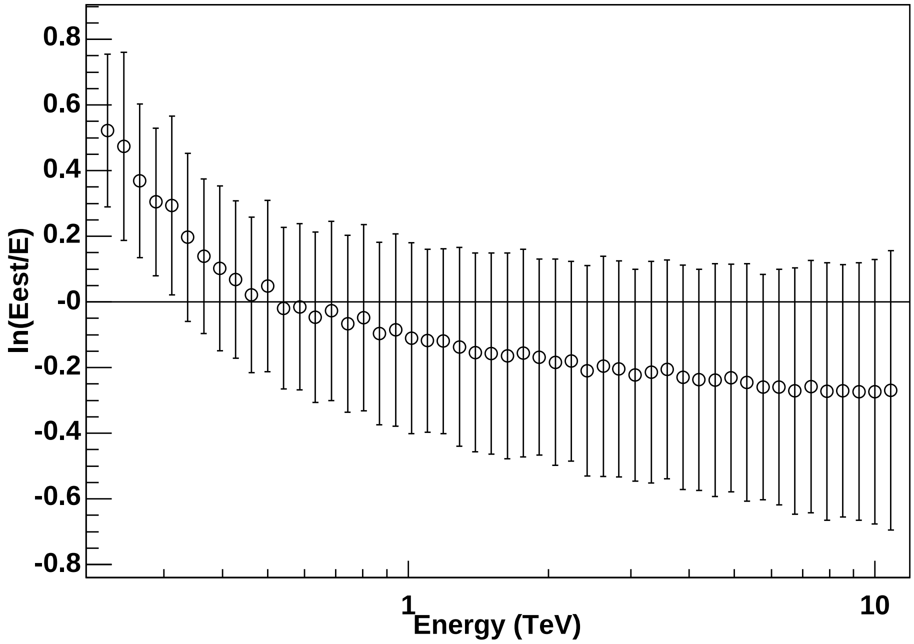

Figure 4.6 Plots of the error in the energy estimator, $\tilde{x} - x$, versus energy. The upper plot uses estimation parameters optimized with an input spectral index of 1.0, and the lower plot uses an input spectral index of 2.5. The error bars give the energy resolution for each energy bin.

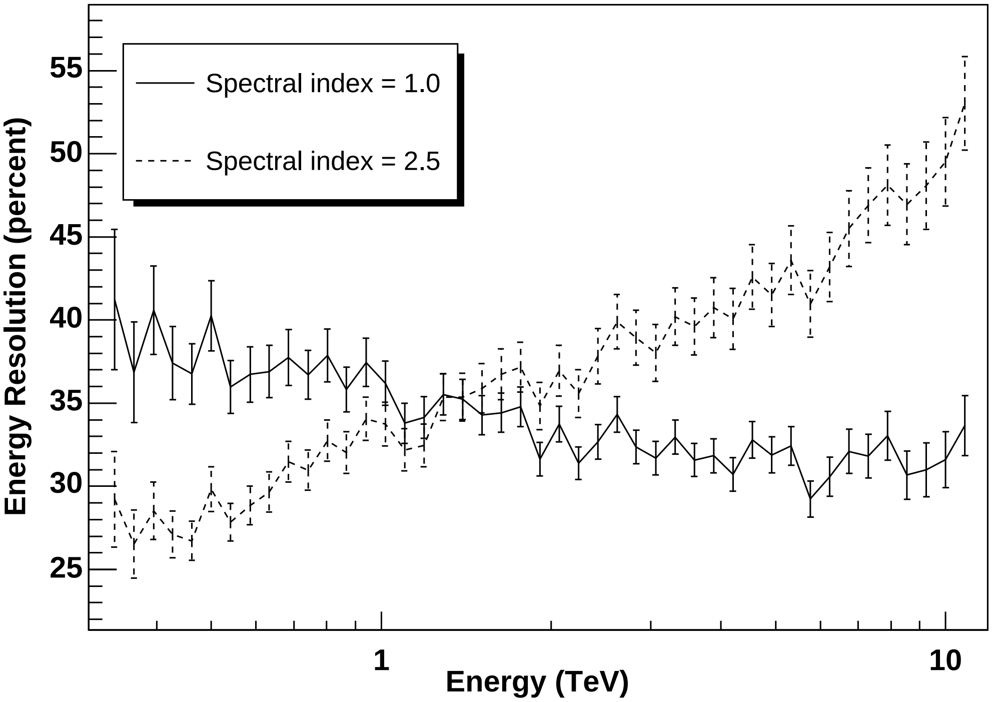

Figure 4.7 The energy resolution versus energy is given in the above plot for both the estimators derived with an input spectral index of 1.0 and 2.5.

resolution of the technique. Using our knowledge of how the energy estimator affects simulated data of a known energy, we would like to be able to regain the actual energy spectrum from the measured spectrum. What we want to know is the gamma-ray flux per unit energy, $d^2N/dEdA$. We define

$$n_i = \int_{E_i}^{E_{i+1}} dE A(E) \frac{d^2N}{dEdA}, \tag{4.16}$$

where $A(E)$ is the telescope's collection area as a function of energy. Then we let $\tilde{n}_i$ be the number of gamma-rays measured in the i^{th} energy bin using the energy estimator. Our problem can then be thought of as finding the matrix M_{ij} such that

$$n_i = M_{ij}\tilde{n}_j. \tag{4.17}$$

The matrix element M_{ij} is the probability that an event measured to be in the j^{th} bin has an actual energy belonging to the i^{th} bin. The complication in this procedure arises from the fact that M_{ij} depends on the actual energy spectrum, which is, of course, unknown. If the energy bins are small enough that the energy spectrum does not change appreciably over their width, then this dependence will be negligible. However, we are limited in how small we can make these bins by the number of observed events — if the number of events per bin becomes too small then the statistical uncertainties will become large. Consequently, we use two different sets of energy bins: a larger set of bins for the actual data, and a finer set of bins for the simulated data.

We will denote the wider bins with Latin indices (n_i) and the narrower bins with Greek indices (n_α). The narrow bins are chosen to be small enough that $n_\alpha \approx A(E_\alpha)(E_{\alpha+1} - E_\alpha)d^2N/dEdA$. Our strategy will be to first calculate the probability of an event having an actual energy in the α^{th} bin given that it is measured with an estimated energy in the β^{th} bin, $P(E_\alpha|\tilde{E}_\beta)$. From this we will calculate the corresponding probabilities for the wider energy bins, $P(E_i|\tilde{E}_j)$ which is equal to M_{ij}.

To find $P(E_\alpha|\tilde{E}_\beta)$ we use simulated data and apply the gamma-ray selection criteria and energy estimator to it. Following our earlier notation, we call the number of events passing the selection criteria with a simulated energy in the α^{th} bin S_α, and the number of events with estimated energy in the β^{th} bin $\tilde{S}_\beta$. The number of events with simulated energy in the α^{th} bin and estimated energy in the β^{th} bin is defined as $N(E_\alpha, \tilde{E}_\beta)$. Then

$$P(E_\alpha|\tilde{E}_\beta) = \frac{N(E_\alpha, \tilde{E}_\beta) n_\alpha / S_\alpha}{\sum_\gamma N(E_\gamma, \tilde{E}_\beta) n_\gamma / S_\gamma}. \tag{4.18}$$

We can then use the fact that

$$P(E_\alpha|\tilde{E}_j) = \sum_{\beta \in j} P(E_\alpha|\tilde{E}_\beta) P(\tilde{E}_\beta|\tilde{E}_j) \tag{4.19}$$

and sum over the index α to find M_{ij}. Substituting $\tilde{n}_\beta / \tilde{n}_j$ for $P(\tilde{E}_\beta|\tilde{E}_j)$, we have

$$M_{ij} = \frac{1}{\tilde{n}_j} \sum_{\alpha \in i} \frac{n_\alpha}{S_\alpha} \sum_{\beta \in j} \frac{N(E_\alpha, \tilde{E}_\beta) \tilde{n}_\beta}{\sum_\gamma N(E_\gamma, \tilde{E}_\beta) n_\gamma / S_\gamma}. \tag{4.20}$$

The method for deconvolving the energy spectrum proceeds by making the initial guess that $n_i = \tilde{n}_i$ and calculating M_{ij}. A new set of n_i are then found by performing the multiplication $M_{ij}\tilde{n}_j$, and M_{ij} is recalculated. This procedure is repeated until the percent change in n_i between iterations falls below some threshold.

Equation 4.20 depends on n_α rather than n_i, so in order for the above process to be employed, a method must be developed to calculate the n_α's from the n_i's. This is done by assuming a functional form for $d^2n/dEdA$ and fitting it to the n_i's. The fit function is then used to calculate the n_α's. The validity of the assumed functional formed can be checked at the end by computing the χ^2 of the fit and making sure it has an acceptable value. If not, then a new functional form must be assumed and the process repeated.

Two different functional forms are used in this work: a simple power law, and a power law with an exponential cutoff. These are given by:

$$\frac{d^2N(E)}{dEdA} = AE^{-\alpha}, \text{and} \tag{4.21}$$

$$\frac{d^2N(E)}{dEdA} = AE^{-\alpha}\text{exp}\left(-\frac{E}{E_o}\right), \tag{4.22}$$

where A, α, and E_o are fit parameters. The parameter α is referred to as the spectral index, and E_o is the cutoff energy. Note that these last two parameters are highly correlated. In fact, near any given energy, E, a Taylor expansion shows that the differential spectrum depends only on the combination $\alpha + E/E_o$. Consequently, the parameter $\alpha + E_*/E_o$ will be used in place of α when giving results for spectral fits, where E_* is adjusted for each data set to give the maximum amount of decorrelation. The effectiveness of this procedure can be seen in figure 4.9.

4.2.4 Testing the Method

Two methods are used for testing the energy spectrum calculation technique described in the previous section. The first is simulating the telescope's response to various input energy spectra and seeing whether the initial spectra can be reconstructed. The second is calculating the spectrum for a source that has already been extensively studied using other techniques.

For the test against simulated data, two sets of simulations are run: one with a spectral index of 2.5 and one with a spectral index of 3.0. Events are randomly removed from these files to produces spectra with various energy cutoffs E_o as defined in equation 4.22. The resulting files each contain about $6,000$ events that pass the gamma-ray selection criteria. Real off-source data are then added to the simulated data to produce the simulated on-source data. Another set of off-source data taken at similar times and zenith angles to the previous set are used as the background data for the analysis. About ten hours of off-source data are used in each case resulting in a data set with a gamma-ray rate of approximately 9 min^{-1}, which corresponds to the rate of Markarian 421 when in a moderately high flux state.

For all of the simulated spectra, we are able to accurately reconstruct the input spectral parameters. Figure 4.8 compares the input and reconstructed differential spectra for two cases, which can be seen to be in good agreement. The one-sigma contours for the fit parameters for α and E_o for these same simulations are shown in figure 4.9. This figure also shows how replacing the parameter α with $\alpha + (1\ \mathrm{TeV})/E_o$ reduces the correlation with E_o, as discussed at the end of section 4.2.3.

A second test of this method for determining the spectral parameters can be made by fitting actual data taken of the Crab Nebula. As mentioned earlier, the Crab Nebula is used as a standard candle because of both the strength and stability of its TeV gamma-ray emissions. Past measurements of this source have indicated that its spectrum is well described by a power law. Specific values for its spectral index include $2.49 \pm 0.06_{stat} \pm 0.04_{syst}$ (61) and $2.74 \pm 0.08_{stat} \pm 0.05_{syst}$ (46). Looking at data taken during the 2003-2004 season, a spectral index of $2.64 \pm 0.08_{stat}$ is found, which is consistent with the previous results.

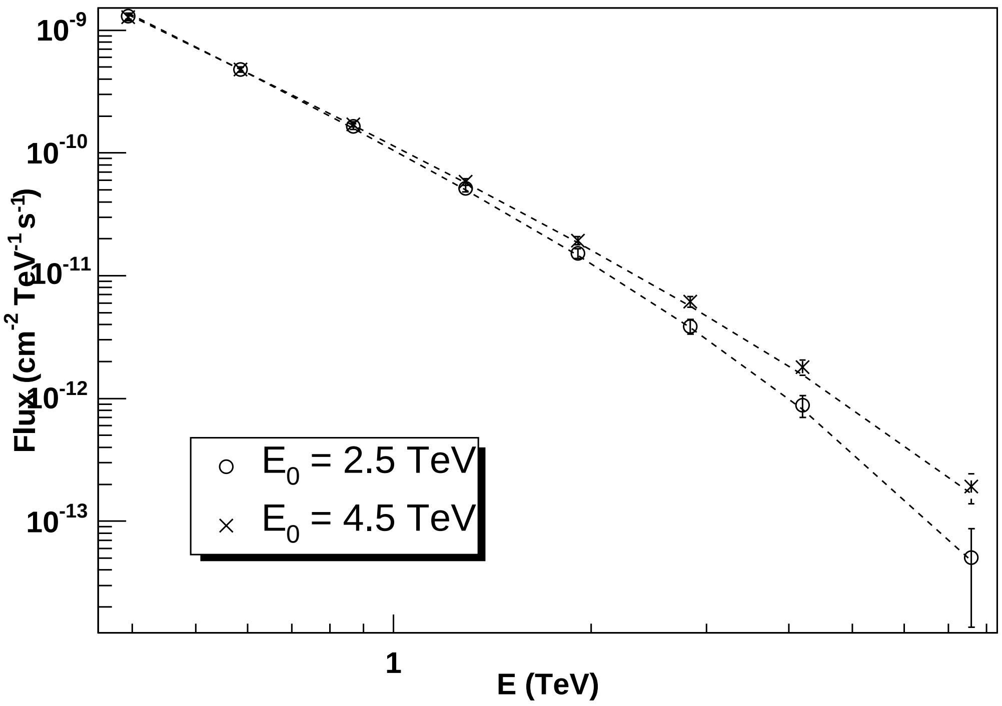

Figure 4.8 The dashed lines show the input spectra for two different simulations, and the ∘s and ×s mark the reconstructed spectra. Cutoff energies of 2.5 TeV and 4.5 TeV are used, both with a spectral index of 2.5.

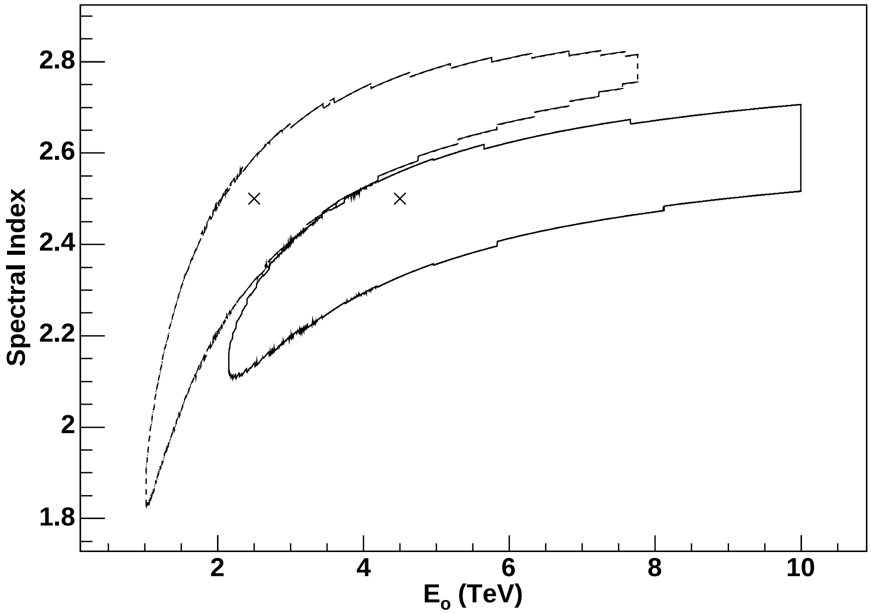

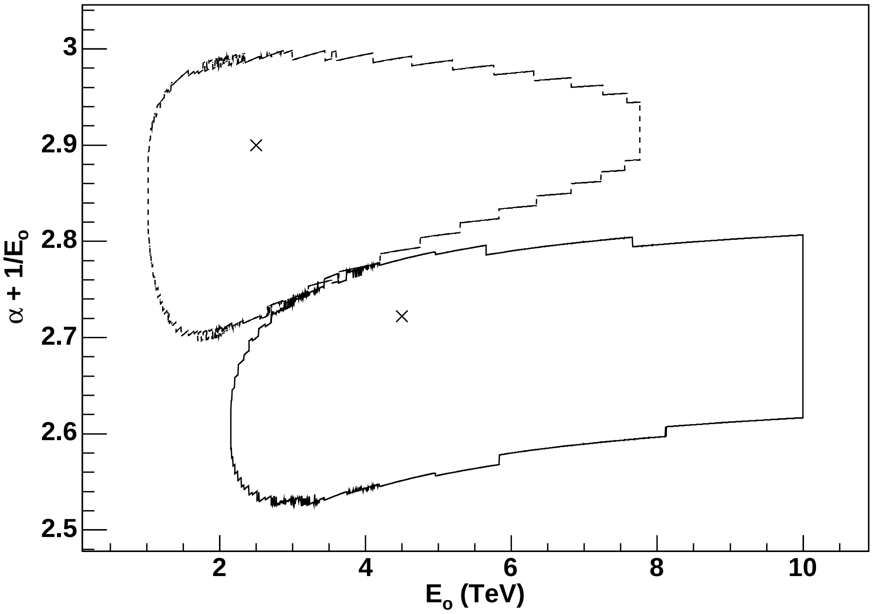

Figure 4.9 One-sigma confidence contours to fits to simulated data. The ×s mark the input spectral parameters. The only difference between the upper and lower figures is the coordinates used to plot the contours. It is clear that the parameter $\alpha + (1\ \text{TeV})/E_o$ is less correlated with E_o than is the parameter α, as discussed at the end of section 4.2.3.

4.3 Rate Normalization

There are a number of different factors that can affect the measured gamma-ray rate besides variations in the source. The primary ones are changes in atmospheric conditions, degradation of the telescope optics, and the source zenith angle. In order to be able to study intrinsic source variations, a technique has been developed to correct for these factors using the fact that the cosmic ray spectrum remains constant with time at the energies we observe (62).

The first step is to create a histogram of the *Size* parameter for all the events before selecting out the gamma-rays. Since cosmic rays dominate the background by such a large margin, this is essentially the same as creating a histogram of cosmic-ray events only. An arbitrary data run is then selected as a benchmark to which all the other runs will be normalized. The throughput factor F for each run is calculated by creating a histogram of $F \times Size$ and adjusting F to minimize the χ^2 difference between that histogram and the $Size$ histogram for the benchmark file after normalizing the histograms for any relative difference in observation time (Fig. 4.10).

If the benchmark run and the run to be corrected are both from the same zenith angle, then applying the correction is straightforward. Assuming a source with differential spectral index β, the observed rate is proportional to $F^{\beta-1}$. As the zenith angle changes, this relationship changes as well due to the same factors discussed in section 3.2.6 that cause the effective collection area and energy threshold to change. From figure 4.11 it can be seen that the cross-sectional area of the Čerenkov light pool is proportional to $\sec^2\theta$, where θ is the zenith angle. The effects of the resulting increase in collection area and dilution of luminosity on the expected throughput can be calculated as follows. Assuming the *Size* distribution has a differential spectral

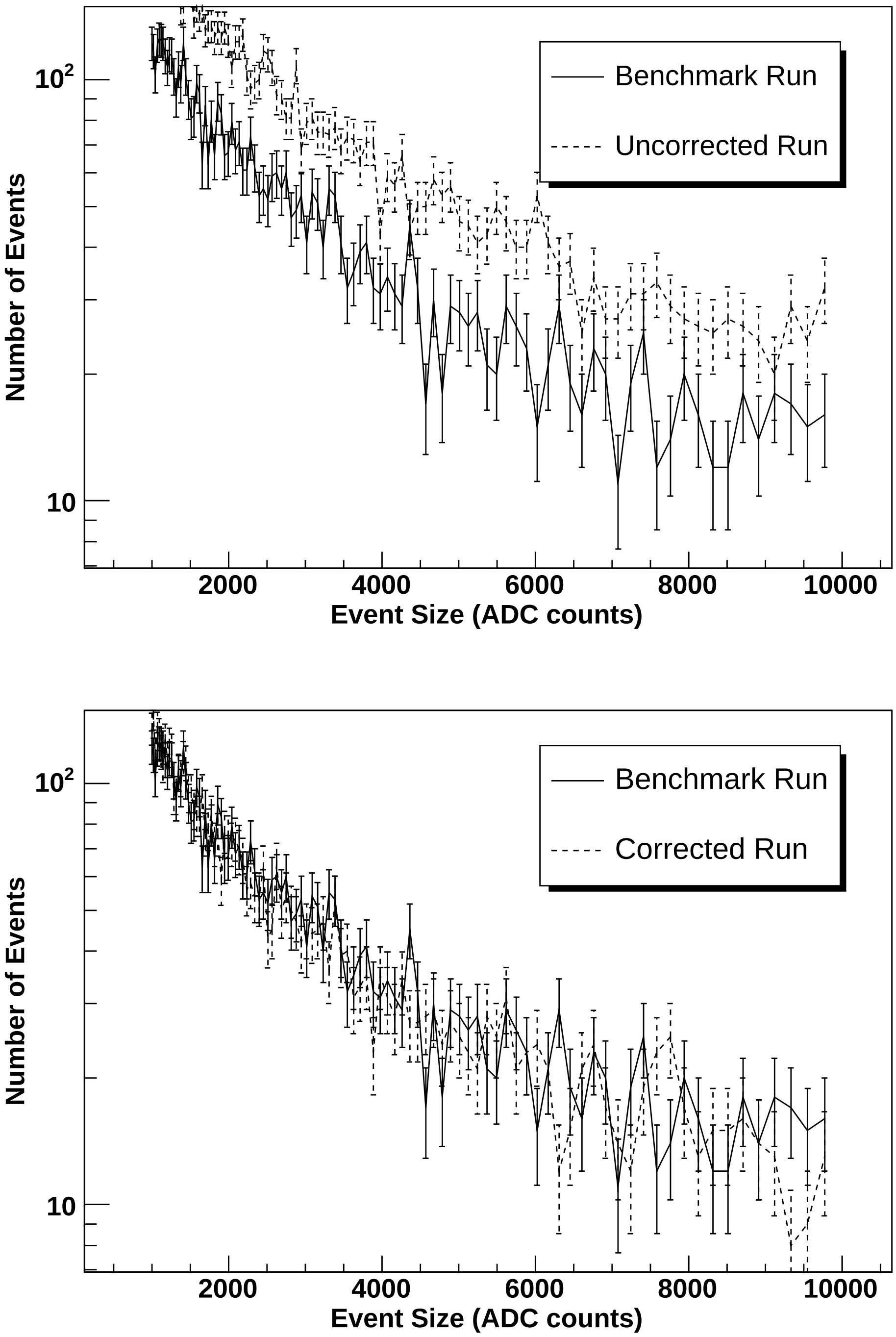

Figure 4.10 The upper plot compares histograms of the *Size* parameter for two particularly poorly matched data files. The lower plot shows the same two runs after a throughput factor of 0.568 has been applied to one of the files.

index of Γ, then the number of events expected in the i^{th} histogram bin is

$$n_i(\theta) = \int_{E_i \sec^2(\theta)}^{E_{i+1}\sec^2(\theta)} dE A \sec^2(\theta) E^{-\Gamma} = (\cos^2(\theta))^{\Gamma-2} n_i(0), \tag{4.23}$$

where A is the normalization of the power law. Applying a throughput correction of F shifts the spectrum so that the number of counts per bin increases by a factor of $F^{\Gamma-1}$. Equating the change in counts from the change in zenith angle, $\cos^2(\theta))^{\Gamma-2}$, to the change resulting from an effective throughput, $F(\theta)^{\Gamma-1}$, we find

$$F(\theta) = \cos^2(\theta)^{(\Gamma-2)/(\Gamma-1)}. \tag{4.24}$$

So to correct for differences in throughput, we need to multiply the rate by $[F_M/F(\theta)]^{\beta-1}$, where F_M is the measured throughput relative to the benchmark file. The measured rate will also change by a factor of $\sec^2(\theta)$ due to the increased collection area, and by a factor of $(\sec^2(\theta))^{1-\beta}$ due to the increased energy threshold for a total change of $(\sec^2(\theta))^{2-\beta}$. Taking into account the effects of both throughput and zenith angle, the corrected rate is

$$r_c = \left(\frac{\cos^2(\theta_B)}{\cos^2(\theta)}\right)^{\beta-2} \left(\frac{F_M}{F(\theta)}\right)^{\beta-1} r. \tag{4.25}$$

The measured rate is denoted by r, and the zenith angle of the benchmark file is θ_B.

One way to test this correction is to apply it to a source that is believed to be steady over time. For TeV astronomy the best candidate is the Crab Nebula. Here we use data taken from September through November 2000 and find that the χ^2 fit to a constant rate drops from 65.12 to 20.87 with 25 degrees of freedom when the above correction method is applied (Fig. 4.12). Thus, without the corrections the

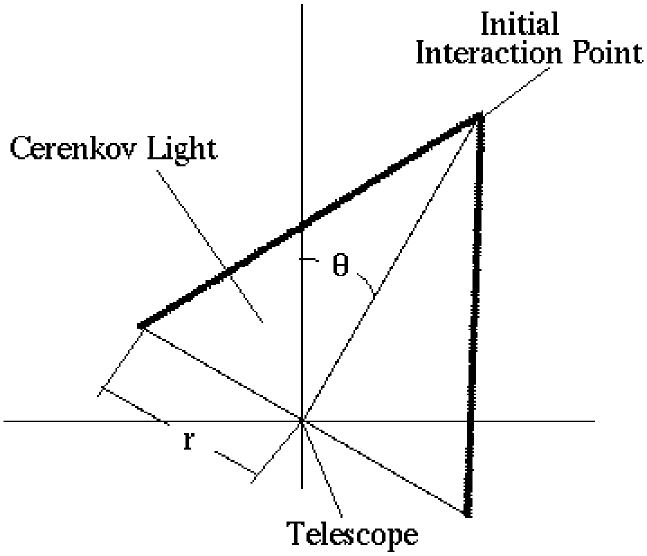

Figure 4.11 This diagram shows the relevant geometry for calculating the zenith angle dependence of the telescope's collection area.

claim that the source has a steady rate would have not been well supported, whereas with the corrections the Crab Nebula is shown to indeed be consistent with having a constant rate. This example shows not only the effectiveness of the throughput corrections but also the necessity of their use when studying rate variability.

To account for the larger instrumental drifts between different observing seasons, fluxes are normalized to the flux of the Crab Nebula as measured that same season. Since the spectral shape of Markarian 421 varies over time, the value of the normalized flux will depend on the energy range over which the flux is measured. In this work, we integrate over all energies above 400 GeV, since this is around the energy threshold of the detector.

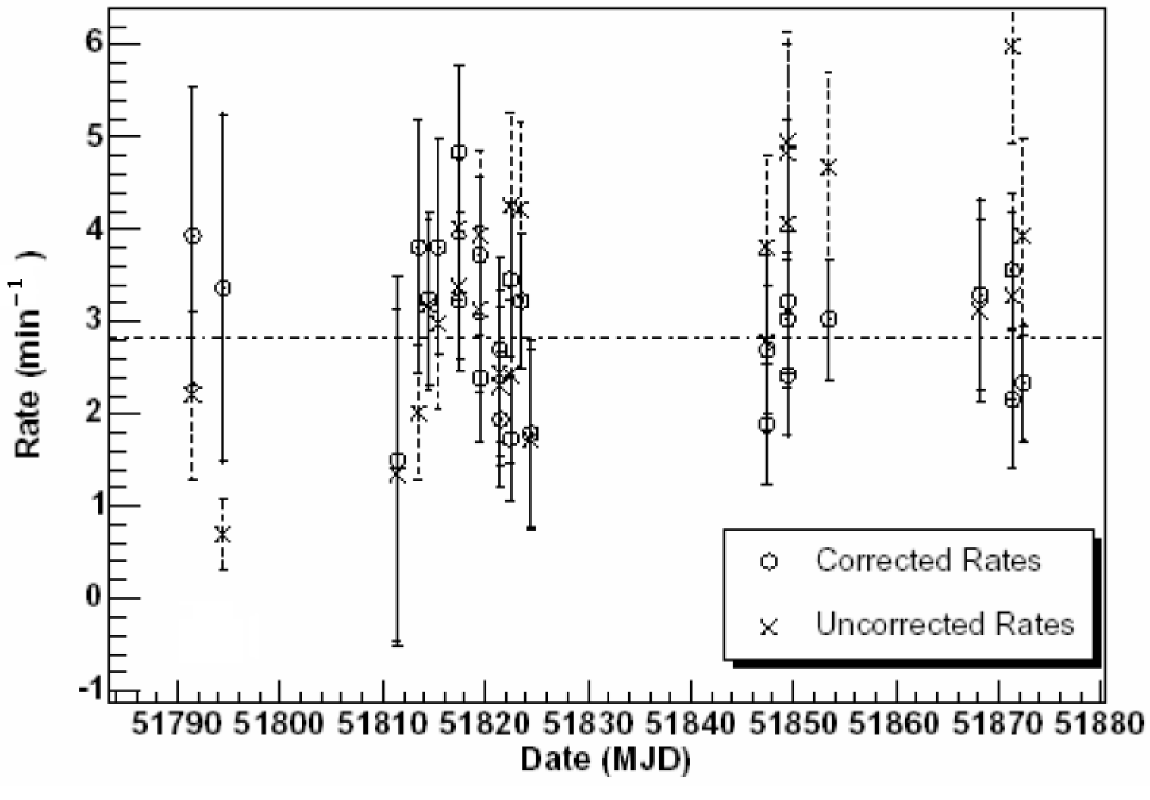

Figure 4.12 The rate versus time for the Crab Nebula both with and without the throughput correction discussed in the text applied.

4.4 Finding Background Data

When sources are in a highly active state observations are often made in TRACKING mode to maximize the on-source time. The TRACKING analysis discussed in section 2.4 works well for calculating the rates for strong sources. However, this technique cannot be used for calculating energy spectra because the energy estimator discussed in section 4.2.2 is dependent on the parameter α. In order to avoid having to discard all the TRACKING data, suitably matched off-source data files taken for other sources are found so that the Markarian 421 data can be treated as ON/OFF data.

Several different characteristics of the background data are compared to those of the on-source data in order to minimize any systematic errors resulting from poorly matched data. The first two factors are the date and zenith angle at which the data were taken. The relative sky quality is checked by calculating the relative throughputs (section 4.3) and by comparing the number of counts in the off-source region of the α histogram (from 20° to 65°). Finally the pedestal variances are compared and preference is given to background files with variances less than that of the on-source files so that in the data padding stage noise is added primarily to the background data (see section 2.4).

For each of these parameters, a distance D_i between the two files is defined (see table 4.3). The total distance between any two files is just

$$D^2 = \sum_i D_i^2. \tag{4.26}$$

A different background data file is selected for each on-source file matching them so as to make the sum of the distances between all the on-source/off-source pairs as small as possible. This optimization is carried out in two steps. First a greedy algorithm is used, where at each step the remaining on-source/off-source pair that has the smallest relative distance between them are paired together and then removed from the list of available files. After a background file has been found for every on-source file, a Metropolis algorithm is used to improve this initial guess. The Metropolis algorithm proceeds by randomly swapping the background files for two on-source files and recalculating the total distance. If the distance is lowered, the swap is automatically kept. Otherwise, the swap is kept with a probability of

$$P = \frac{1}{D}\exp\left(\frac{-\Delta D}{D}\right), \tag{4.27}$$

where D is the old total distance and ΔD is the change in the total distance. The reason for not immediately rejecting all swaps that increase the total distance is to avoid becoming trapped in a local minimum that is not the global minimum.

Table 4.3 Parameters used to quantify how well matched two data files are.

	Parameter	Definition	ϵ_i
D_0	Modified Julian Day	$(\mathrm{MJD}_{on} - \mathrm{MJD}_{off})/\epsilon_0$	30 days
D_1	Zenith Angle	$(\mathrm{ZA}_{on} - \mathrm{ZA}_{off})/\epsilon_1$	5.0°
D_2	Relative Throughput	$(F-1)/\epsilon_2$	0.05
D_3	Off-source Difference	$(N_{on} - N_{off})/\sqrt{N_{on}+N_{off}}/\epsilon_3$ (N_{on} and N_{off} are counts with $20^\circ \leq \alpha \leq 65^\circ$.)	2.5
D_4	Pedestal Variance	$(\sigma_{off}/\sigma_{on} - 1)/\epsilon_4$, if $\sigma_{off} > \sigma_{on}$ 0, if $\sigma_{off} \leq \sigma_{on}$	1.0

Once suitable background data have been found, analysis proceeds the same as with the standard ON/OFF analysis with one exception. Instead of weighting the background file by the relative observation time to the on-source file, it is weighted by the ratio of the number of counts in both files with $20° \leq \alpha \leq 65°$.

This method can be tested by comparing it with the standard ON/OFF analysis. Using 26 runs of Crab Nebula data for which concurrent off-source data have been taken, the above procedure is used to find a second set of background data. The rates for each run are then calculated using each set of background. A χ^2 of 24.23 with 25 degrees of freedom is found when comparing these rates, which is consistent with statistical fluctuations. Thus, the above procedure is capable of finding off-source data that reproduce the ON/OFF analysis rates to within the statistical uncertainties.

4.5 Results

4.5.1 Rate Variability

The data used for this study were collected over four different observation periods during the 2003-2004 observing season. The last three periods each correspond to observations made over a single month between full moons. For the first period, multiple months are combined since the source rate was low and, consequently, data were taken less frequently. Figure 4.13 shows the gamma-ray rate of Markarian 421 as a function of time. A constant fit to these rates is rejected at well beyond the 99.9% confidence level ($\chi^2 = 1,928$ with 201 degrees of freedom), indicating clear evidence for variablity over this time span.

The flux levels and variability in the flux for Markarian 421 for the four observing periods are given in table 4.4. During the first period the source is in a relatively quiet state, with an average flux slightly below that of the Crab Nebula. The second period sees an increase in the flux, building to a level of 2.85 times the Crab Nebula in the third period. There is a dramatic drop in the rate the last two days of the third

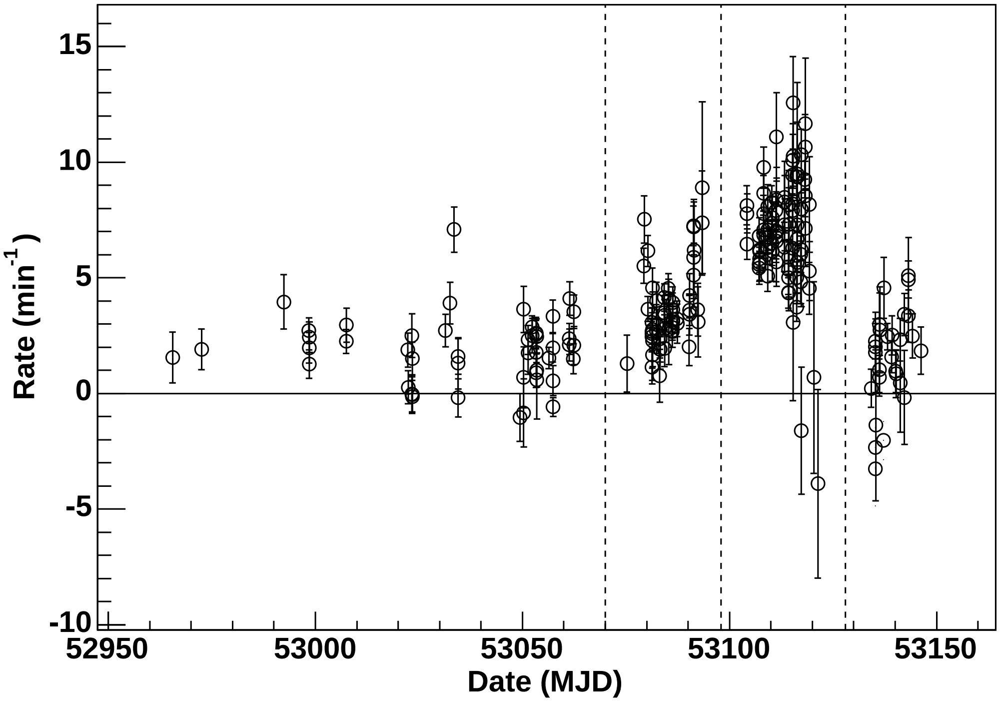

Figure 4.13 Rate versus modified Julian day for Markarian 421 in the spring of 2004. The vertical lines indicate the periods into which the data are divided for analysis.

period. When observations began again in the fourth period, Markarian 421 was in a much quieter state, with emissions at only about two thirds of the Crab Nebula. A constant function is fit to the rates during each period, and the χ^2 per degrees of freedom of these fits is taken as a simple measure of the variability over that time. This number remains fairly stable throughout the season, ranging from 2.90 to 3.75.

Table 4.4 Average flux and variability in the flux of Markarian 421 over four different periods during the 2003-2004 observing season. Fluxes are normalized to the Crab Nebula flux above 400 GeV. The χ^2 refers to a fit to a constant function, and DOF gives the number of degrees of freedom of the fit.

Period	Dates	Flux (Crabs)	χ^2/DOF	DOF
1	Nov. 11, 2003 - Feb. 27, 2004	0.96	3.49	48
2	Mar. 11 - 29, 2004	1.48	2.90	49
3	Apr. 9 - 26, 2004	2.85	3.19	75
4	May 9 - 21, 2004	0.66	3.75	26

4.5.2 Spectral Fits

The energy spectra for each of the four periods in the 2003-2004 season are fit with a power law with an exponential cutoff (equation 4.22). The best fit parameters for each period are given in table 4.5, and the one sigma uncertainty contours are shown in figure 4.14, where the spectral index α has been replaced by $\alpha + (1\text{ TeV})/E_o$ as discussed in section 4.2.3. The trend of spectral hardening (decreasing $\alpha+(1\text{ TeV})/E_o$) can be seen in the first three periods as the rate increases. The fourth period does not appear as soft as the first despite its lower flux, although the limited statistics make it difficult to be too precise about this last period. Note, given the precision of the current measurements it is impossible to say whether the observed spectral changes are due to changes in α or E_o, or a combination of both. Another important factor to notice is that the upper limit on E_o for the second and third periods is finite. Thus, these spectra are inconsistent with a simple power-law with no cutoff.

Table 4.5 Best fit parameters for the differential energy spectrum of Markarian 421 during the four observing periods in 2004. The parameters refer to a power law with exponential cutoff as defined in equation 4.22. DOF gives the number of degrees of freedom of the fit.

Period	A (cm^{-2} s^{-1} TeV^{-1})	α	E_o (TeV)	χ^2/DOF	DOF
1	2.74×10^{-11}	2.75	5.02	0.833	5
2	6.00×10^{-11}	2.34	2.18	0.287	5
3	13.58×10^{-11}	2.10	2.30	0.140	5
4	1.97×10^{-11}	2.63	10.24	0.738	4

To investigate more precisely how the spectral shape varies with the source flux, we compare the 2004 flare with a larger flare that occurred in 2001. For this earlier flare, a parabolic fit to the spectral index versus flux has been made (48):

$$\alpha(\phi) = 2.66 - 0.123\phi + 0.0056\phi^2, \tag{4.28}$$

where ϕ is the ratio of Markarian 421's flux to that of the Crab Nebula. As a further test of our methods, we calculate our own fits to the 2001 data. Since the original 2001 fit was made by sorting the data by the measured rates, we also sort the data by rates as well as by observing periods when fitting the spectral parameters. If a single mechanism is responsible for all the observed flares, then all data with the same rates should share the same spectral features, justifying the use of rates to separate the data. In this case we might still expect to see a well defined spectral shape versus flux relationship in the data sorted by dates if the variation in rates between date bins is greater than the variation within each bin.

The dates of the observing periods are given in table 4.6. Tables 4.7 and 4.8

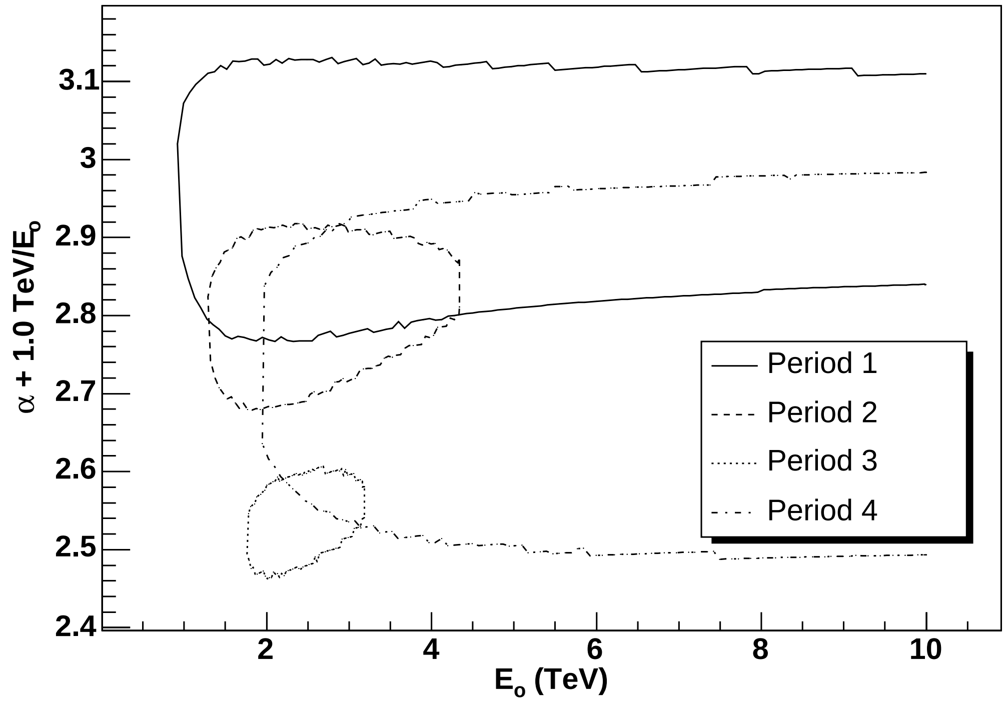

Figure 4.14 One sigma contours for the fits to the spectral parameters for the four observing periods in the 2003-2004 season.

give the best fit parameters for the rate and date binned data, respectively, and the uncertainty contours of these fits are given in figure 4.15. When these new parameters are compared with the fit in equation 4.28, the resulting χ^2s are not good (17.7 with 5 degrees of freedom for the rate binned data and 51.8 with 4 degrees of freedom for the date binned data) and there is an apparent vertical offset between the new fits and the old. One likely cause of this is the large systematic uncertainty in the cutoff-energy fits. Such a systematic shift can be accounted for by allowing the constant term in the fit to vary. Changing this term from 2.66 to 2.60 results in much improved χ^2s of 6.3 with 4 degrees of freedom and 18.2 with 3 degrees of freedom for the data binned by rate and date, respectively (Fig. 4.16). A fit to the spectral parameters calculated in this work for the rate binned data yields:

$$\alpha(\phi) + (1.3\text{TeV})/E_o = 2.96 - 0.178\phi + 0.0142\phi^2. \tag{4.29}$$

This gives a χ^2 of 2.03 with 2 degrees of freedom for the rate binned data and 6.88 with 4 degrees of freedom for the date binned data.

Table 4.6 Dates for the observing periods used for the 2000-2001 season along with the average flux of Markarian 421 for each period. Fluxes are normalized to the Crab Nebula flux above 400 GeV.

Period	Dates	Flux (Crabs)
1	Nov. 28, 2000 - Jan. 4, 2001	0.84
2	Jan. 20 - Feb. 4, 2001	2.75
3	Feb. 17 - Feb. 27, 2001	4.10
4	Mar. 15 - Apr. 1, 2001	3.48

The same procedure is repeated for the 2004 data to see whether the relations in equations 4.28 and 4.29 still hold three years later. The fit parameters and uncertainty contours for the rate binned data are given in table 4.9 and figure 4.17. For the date

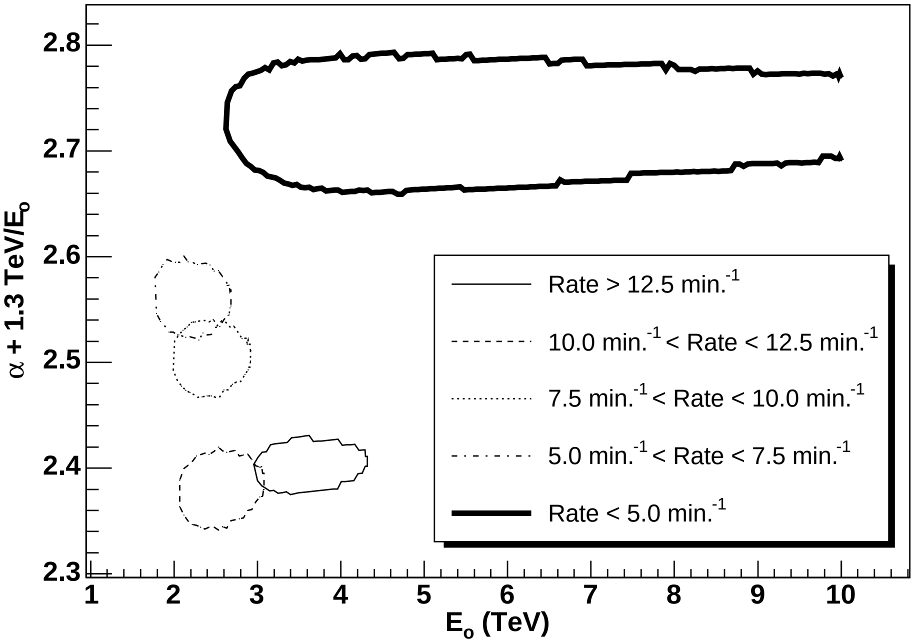

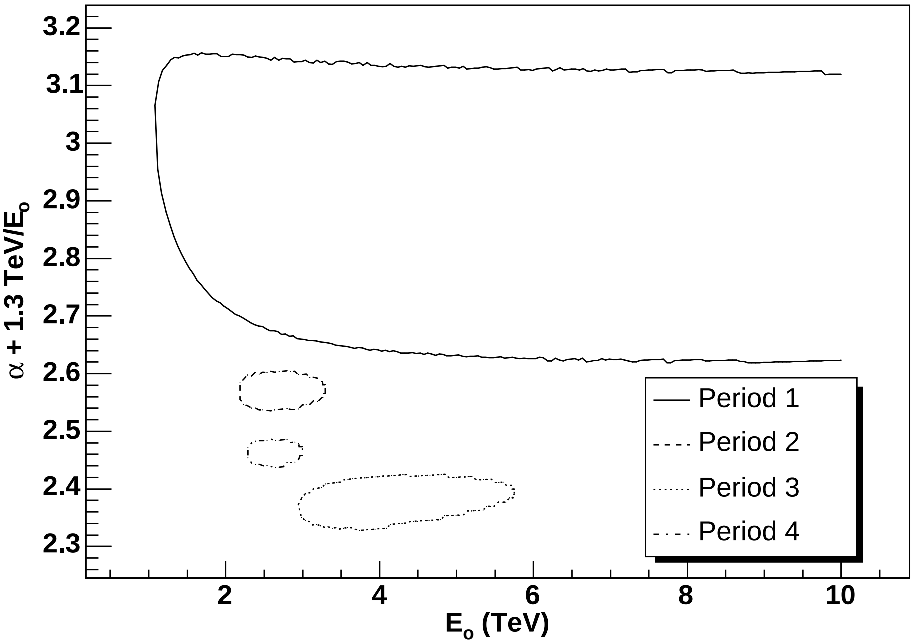

Figure 4.15 One sigma contours for the fits to the spectral parameters for the 2000-2001 season. In the upper plot the data have been sorted by the gamma-ray rate, and in the lower one they have been sorted by observation date (see table 4.6).

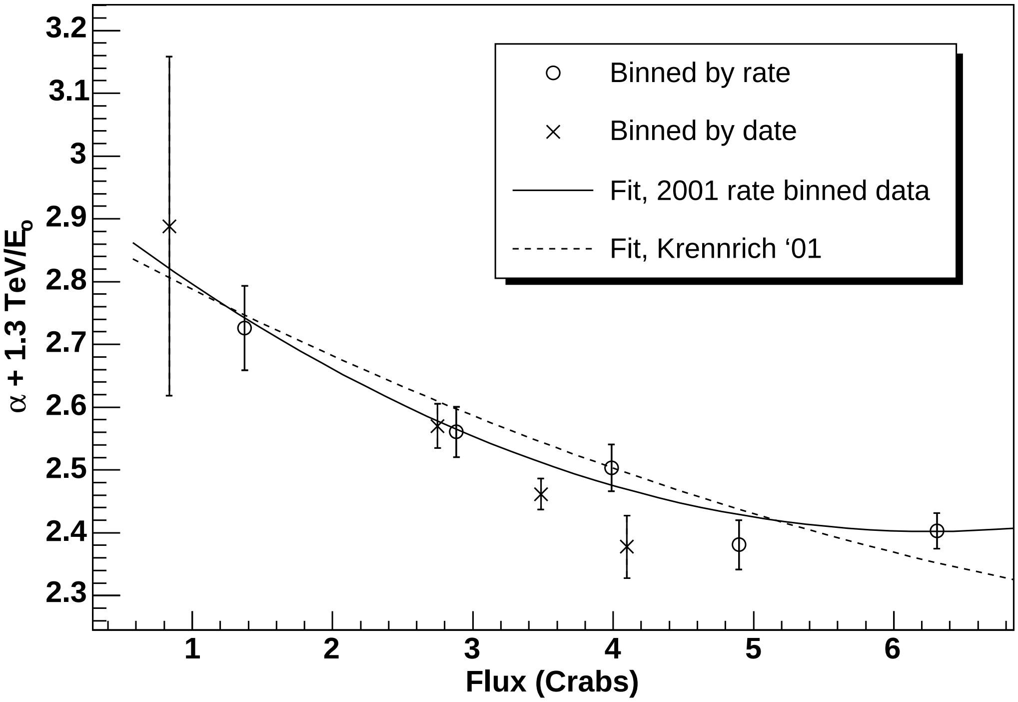

Figure 4.16 Plots of $\alpha + (1.3\ \mathrm{TeV})/E_o$ versus flux for the 2000-2001 season. The 2001 fit has been shifted vertically to account for possible systematic errors (see text).

Table 4.7 Best fit parameters for the differential energy spectrum of Markarian 421 for the 2000-2001 observing season when sorted by gamma-ray rates. DOF gives the number of degrees of freedom of the fit.

Rate	A (cm^{-2} s^{-1} TeV^{-1})	α	E_o (TeV)	χ^2/DOF	DOF
$r > 12.5$ min^{-1}	29.69×10^{-11}	2.03	3.53	0.164	5
$10.0 < r < 12.5$ min^{-1}	25.77×10^{-11}	1.85	2.45	0.784	5
$7.5 < r < 10.0$ min^{-1}	21.18×10^{-11}	1.95	2.36	0.083	5
$5.0 < r < 7.5$ min^{-1}	16.41×10^{-11}	1.97	2.20	0.602	5
$r < 5.0$ min^{-1}	5.11×10^{-11}	2.44	4.66	0.931	5

Table 4.8 Best fit parameters for the differential energy spectrum of Markarian 421 for the 2000-2001 observing season when sorted into the observing periods given by the dates in table 4.6. DOF gives the number of degrees of freedom of the fit.

Period	A (cm^{-2} s^{-1} TeV^{-1})	α	E_o (TeV)	χ^2/DOF	DOF
1	2.89×10^{-11}	2.65	6.15	0.245	5
2	14.07×10^{-11}	2.08	2.67	0.560	5
3	20.51×10^{-11}	2.03	3.73	1.273	5
4	19.69×10^{-11}	1.96	2.59	1.245	5

binned data they are given above in table 4.5 and figure 4.14. Note, $\alpha + (1.0\text{ TeV})/E_o$ is used rather than $\alpha + (1.3\text{ TeV})/E_o$ as is used for the 2001 data. This difference is accounted for in fits to equation 4.29 by again leaving the constant term as a free parameter, which is done anyway to compensate for systematic changes between seasons. The 2004 data are in good agreement with the 2001 data, yielding χ^2s of 5.70 with 4 degrees of freedom and 1.36 with 3 degrees of freedom for the rate and date bin data when compared with equation 4.29 (Fig. 4.18).

Given the agreement between the 2001 and 2004 results, it seems that the relationship between spectral shape and flux on the time scale of months is relatively stable, over the period of a couple of years, at least. Another interesting question is whether the mechanism for flares on shorter time scales is the same as for that at longer time

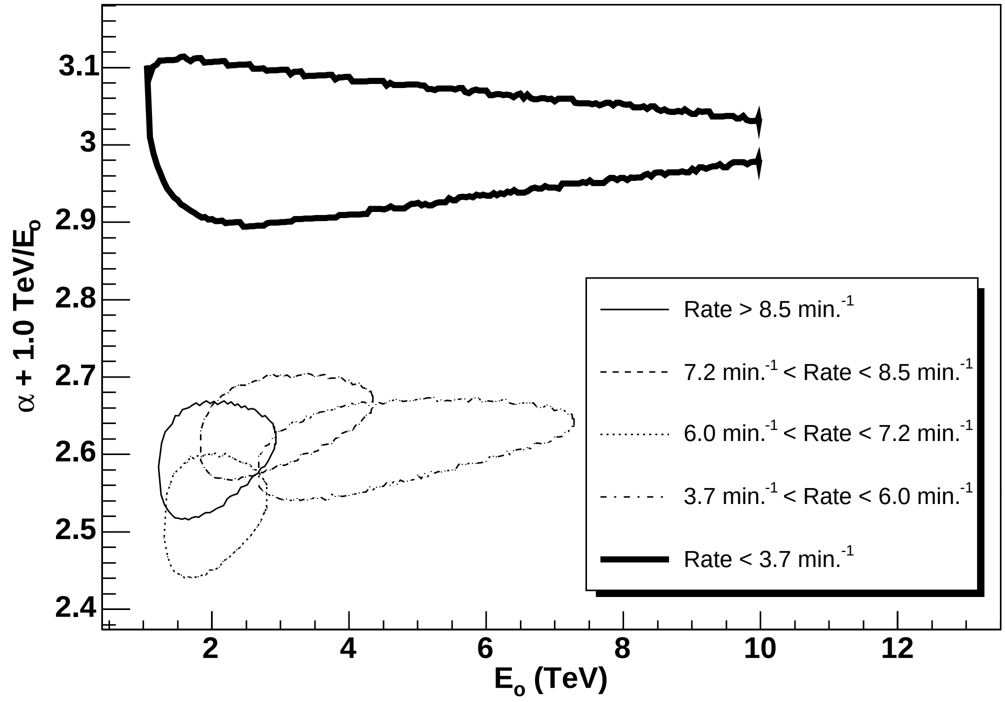

Figure 4.17 One sigma contours for the fits to the spectral parameters for data binned by gamma-ray rates in the 2003-2004 season.

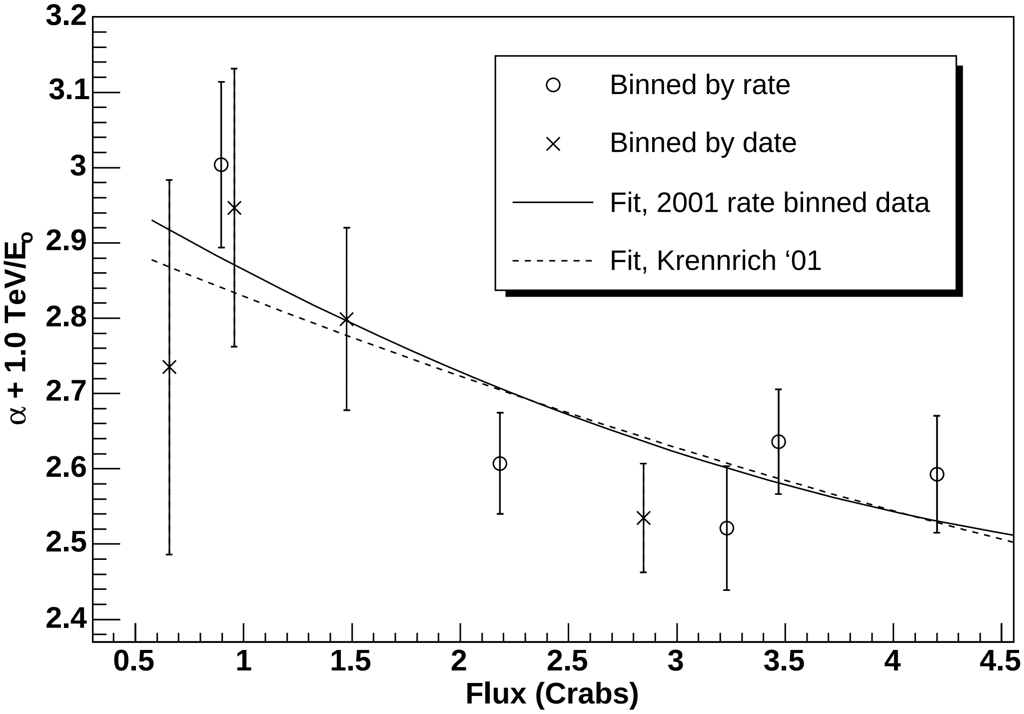

Figure 4.18 Plots of $\alpha + (1.0\ \text{TeV})/E_o$ versus flux for the 2003-2004 season. The fits has been shifted vertically to account for possible systematic errors (see text).

Table 4.9 Best fit parameters for the differential energy spectrum of Markarian 421 for the 2003-2004 observing season when sorted by gamma-ray rates. DOF gives the number of degrees of freedom of the fit.

Rate	A (cm^{-2} s^{-1} TeV^{-1})	α	E_o (TeV)	χ^2/DOF	DOF
$r > 8.54$ min^{-1}	18.66×10^{-11}	2.08	1.96	0.301	5
$7.20 < r < 8.54$ min^{-1}	12.87×10^{-11}	2.27	2.71	0.150	5
$6.01 < r < 7.20$ min^{-1}	15.23×10^{-11}	1.98	1.85	0.185	5
$3.66 < r < 6.01$ min^{-1}	7.34×10^{-11}	2.32	3.62	1.09	5
$r < 3.66$ min^{-1}	3.06×10^{-11}	2.57	2.40	0.116	5

scales. One test that can be made of this is whether the spectral shape versus flux relations hold when the data from a shorter time scale are binned together. Since the third period of 2004 has the highest average flux and most observation time for that season, we focus on it to look for day-scale changes in flux and spectral shape. As before, we bin the data by both date (see table 4.10) and rate, fit the spectral parameters (tables 4.11 and 4.12, and Fig. 4.19), and compare with equation 4.29. From figure 4.20, it can be seen that the previous spectral shape versus flux relation does not provide a good fit to the data. The χ^2 values for the rate and date binned data, respectively, are 18.35 with 4 degrees of freedom and 13.35 with 4 degrees of freedom. This discrepancy suggests that there may be a flaring mechanism acting on day time scales that differs from the one acting on month scales. Note, from the date binned data it is clear that the spectral shape still varies over time (for instance between the first three periods), but these changes are no longer correlated with the flux in the same way as the data averaged over month scales are.

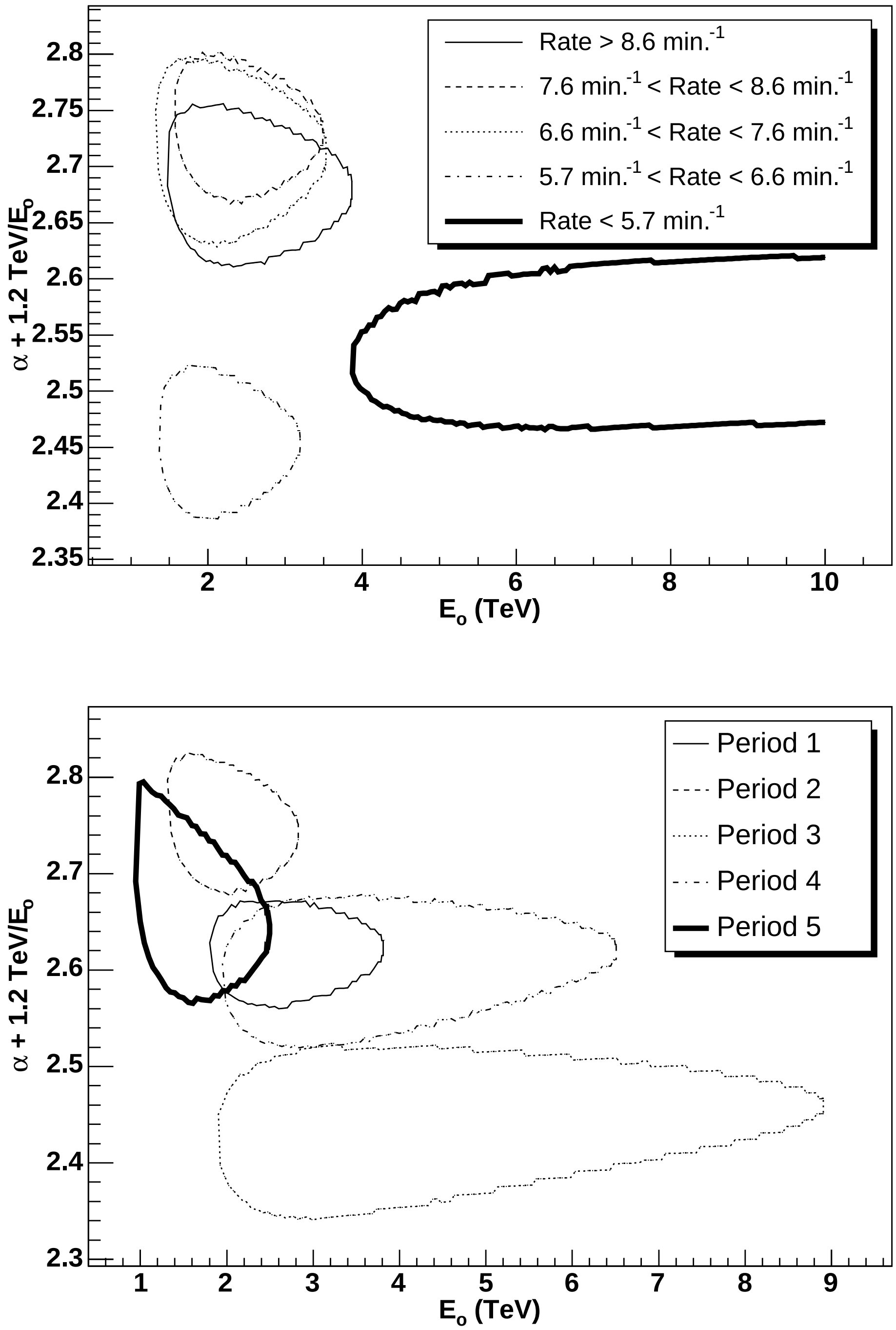

Figure 4.19 One sigma contours for the fits to the spectral parameters for subdivisions of the third observing period in the 2003-2004 season. In the upper plot the data have been sorted by the gamma-ray rate, and in the lower one they have been sorted by observation date (see table 4.6).

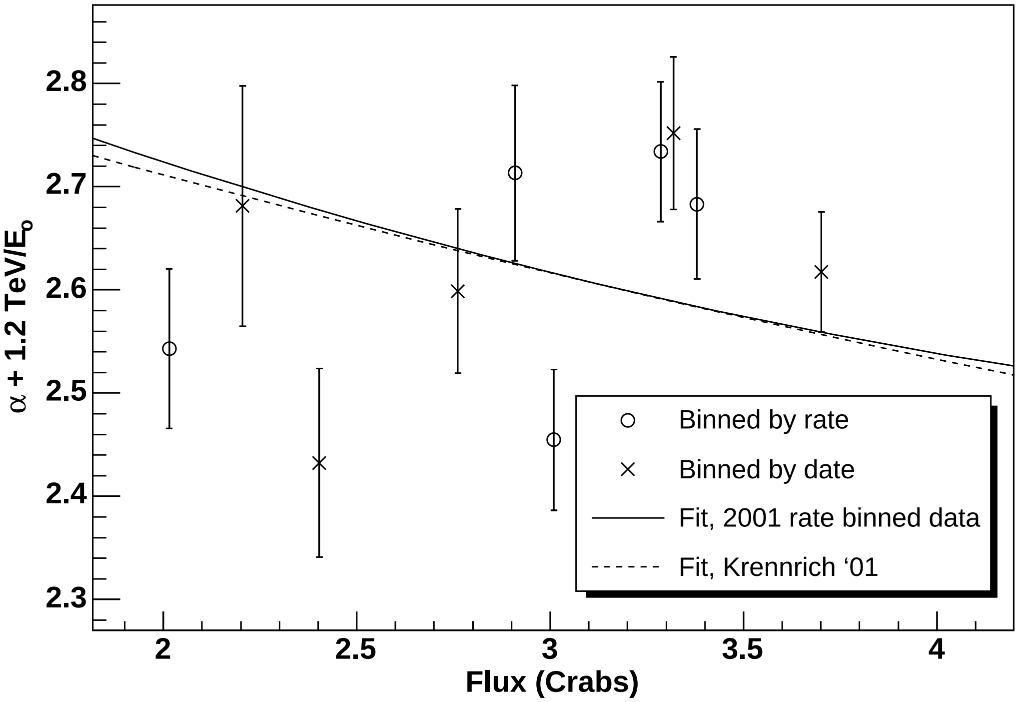

Figure 4.20 Plots of α+(1.2 TeV)/E_o versus flux for subdivisions of the third observing period in the 2003-2004 season. The fits has been shifted vertically to account for possible systematic errors (see text).

Table 4.10 Subdivision of dates within the third period of the 2003-2004 season along with the average flux of Markarian 421 for each subdivision. Fluxes are normalized to the Crab Nebula flux above 400 GeV.

Period	Dates	Flux (Crabs)
1	Apr. 9 - 13	3.70
2	Apr. 14 - 16	3.32
3	Apr. 16 - 20	2.40
4	Apr. 21	2.76
5	Apr. 22 - 25	2.20

Table 4.11 Best fit parameters for the differential energy spectrum of Markarian 421 for April of 2004 with data sorted by gamma-ray rates. DOF gives the number of degrees of freedom of the fit.

Rate	A (cm^{-2} s^{-1} TeV^{-1})	α	E_o (TeV)	χ^2/DOF	DOF
$r > 8.6$ min^{-1}	16.80×10^{-11}	2.18	2.43	0.337	5
$7.6 < r < 8.6$ min^{-1}	14.22×10^{-11}	2.21	2.28	0.340	5
$6.6 < r < 7.6$ min^{-1}	14.23×10^{-11}	2.14	2.11	0.128	5
$5.7 < r < 6.6$ min^{-1}	15.25×10^{-11}	1.81	1.88	0.477	4
$r < 5.7$ min^{-1}	6.72×10^{-11}	2.42	9.64	0.566	5

4.5.3 Cutoff Properties

In addition to looking at the overall steepness of the spectrum, we can also study the cutoff feature characterized by the parameter E_o. As mentioned in section 4.1.2, it is currently viewed as unlikely that this cutoff is purely a result of absorption by the EBL (see section 4.1.4). A simple test of this hypothesis is to check for variations in E_o over time. If E_o were seen to change, then this would be a clear indication that its cause is internal rather than external. Figure 4.21 shows a plot of the cutoff energy versus source flux. A constant fit to the data yields a value of 2.40 TeV with a $\chi^2 = 2.4$ for 4 degrees of freedom. Thus, there is no evidence for variability, although the large error bars do not allow us to eliminate the possibility that E_o is changing.

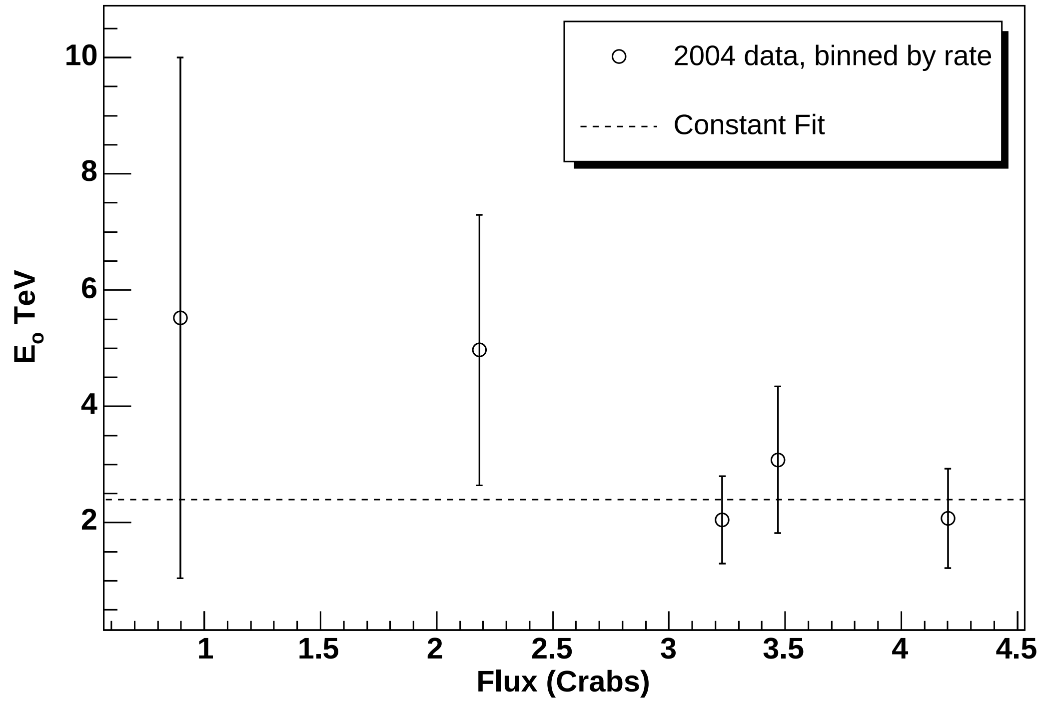

Figure 4.21 Plots of the cutoff energy versus flux for Markarian 421 for the 2003-2004 season. The data have been sorted by gamma-ray rate.

Table 4.12 Best fit parameters for the differential energy spectrum of Markarian 421 for April of 2004 with data sorted into the observing periods given by the dates in table 4.10. DOF gives the number of degrees of freedom of the fit.

Period	A (cm^{-2} s^{-1} TeV^{-1})	α	E_o (TeV)	χ^2/DOF	DOF
1	14.69×10^{-11}	2.14	2.51	0.076	5
2	15.14×10^{-11}	2.09	1.81	0.191	5
3	10.25×10^{-11}	2.02	2.96	0.992	5
4	12.24×10^{-11}	2.23	3.25	0.177	5
5	15.76×10^{-11}	1.88	1.55	0.376	5

Despite the large uncertainties, we can still test the hypothesis that the cutoff is purely a product of absorption by the EBL. First, we can compare the amount of attenuation predicted by equation 4.10 to the observed exponential cutoff. Assuming the data shown in figure 4.21 do indeed represent a constant cutoff, we can compute the 95% confidence statistical upper limit on E_o to be 3.38 TeV. To estimate the systematic uncertainty we vary the gain in the simulations used to calculate the energy spectrum by 20% and refit the data. Doing this shows that E_o can vary by up to approximately 1.5 TeV, which we will take as the systematic uncertainty. Adding this to the statistical uncertainty yields an upper limit on the cutoff energy of less than 5 TeV. Figure 4.22 compares the theoretical absorption by the EBL with the functional form $\exp[-E/(5.0\ \mathrm{TeV})]$. Above 2 TeV the EBL calculation producess far less absorption than what is shown by the exponential cutoff. This indicates that something else in addition to the EBL is responsible for the observed cutoff.

A more precise method of making this test is by using a power law convolved with the theoretical EBL attenuation rather than a power law with an exponential cutoff as the assumed functional form when performing the spectral deconvolution (section 4.2.3). The results of this procedure are shown in table 4.13. The χ^2 per degree of freedom for all but the lowest rate data are unacceptably high (compare

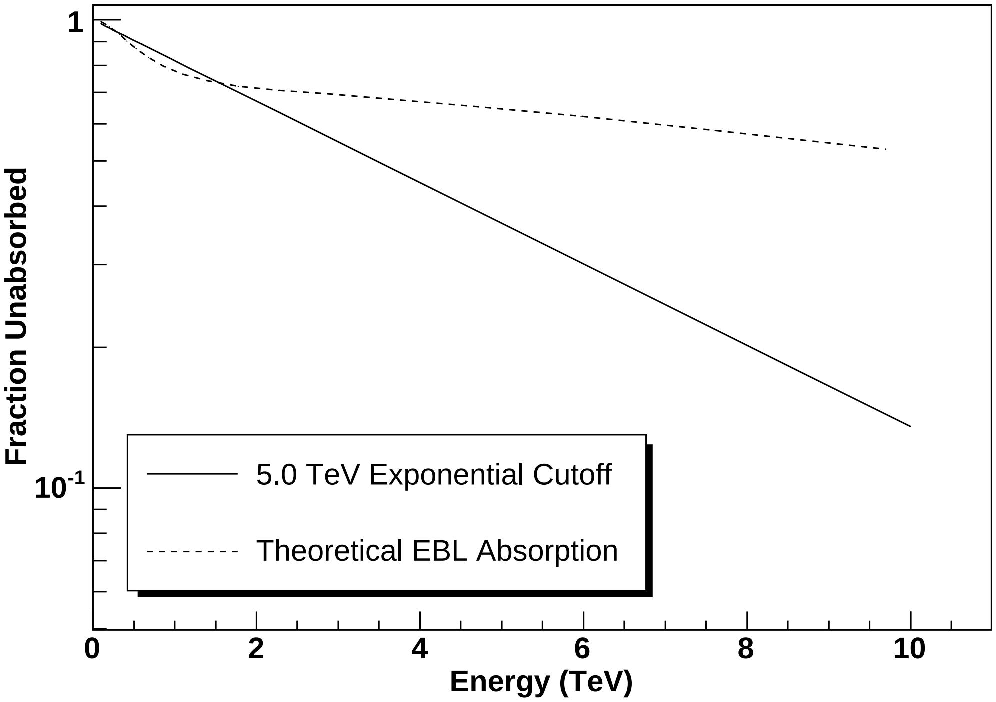

Figure 4.22 The survival probability of photons versus photon energy predicted by an exponential cutoff at 5.0 TeV and by EBL absorption.

with table 4.9) indicating that the chosen functional form is a bad one. The good fit to the lowest rate data is most likely caused by the softer spectrum and overall lower rate which leads to greater statistical uncertainty in the higher energy bins where the EBL prediction is most inadequate. Figure 4.23 shows the measured differential spectra compared with the fits for two of the rate bins. These poor fits are further evidence that the cutoff in Markarian 421's spectrum is intrinsic rather than being caused by the EBL alone.

Table 4.13 Best fit parameters for the differential energy spectrum of Markarian 421 for the 2003-2004 observing season assuming a simple power law spectrum attenuated by the semianalitc EBL calculation. DOF gives the number of degrees of freedom of the fit.

Rate	A (cm^{-2} s^{-1} TeV^{-1})	α	χ^2/DOF	DOF
$r > 8.54$ min^{-1}	12.11×10^{-11}	2.58	4.683	6
$7.20 < r < 8.54$ min^{-1}	9.97×10^{-11}	2.60	3.67	6
$6.01 < r < 7.20$ min^{-1}	9.24×10^{-11}	2.57	14.08	6
$3.66 < r < 6.01$ min^{-1}	6.42×10^{-11}	2.56	3.27	6
$r < 3.66$ min^{-1}	2.34×10^{-11}	2.86	0.90	6

4.6 Discussion

While there have been previous studies of the Whipple 10-m telescope's observations of the 2004 flare of Markarian 421 (45), they limited themselves only to data taken simultaneously with x-ray observations. Thus, this work represents the first analysis of the entire Whipple data set for Markarian 421 during the 2003-2004 season. Although this flare did not produce rates as high as those seen in some previous ones, it still provides some interesting constraints on the production mechanism of TeV photons in this source.

The relationship between spectral shape and flux observed in the 2001 flare (48)

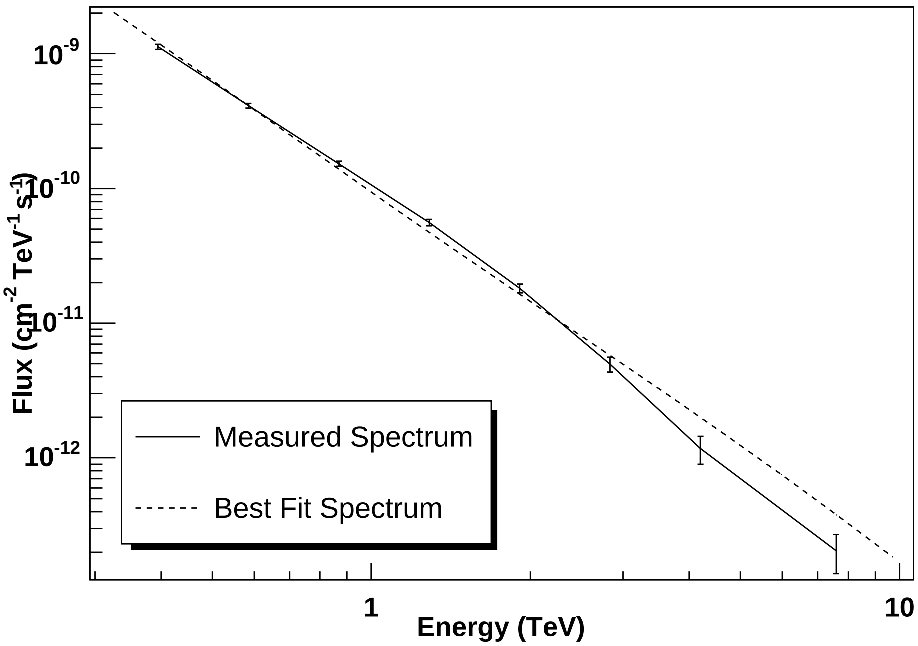

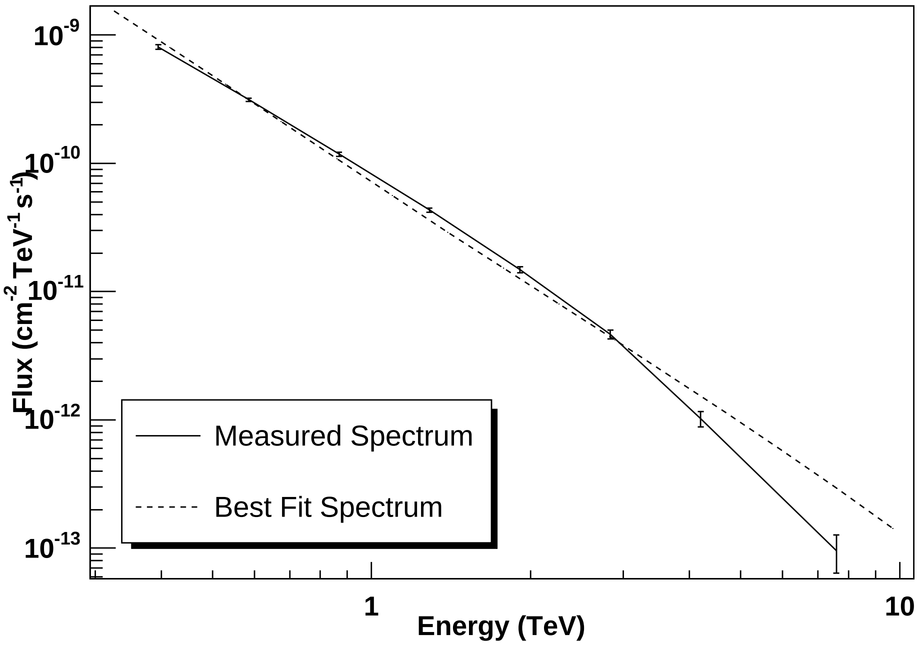

Figure 4.23 The observed differential spectra of Markarian 421 compared to fits assuming a power law with EBL absorption. The upper plot is for data with gamma-ray rates > 8.54 min^{-1}, and the lower plot is for 6.01 min^{-1} $<$ rate $<$ 7.20 min^{-1}.

has been shown to be consistent with the 2004 data as well, suggesting that the flaring mechanism is stable over the timescale of years (section 4.5.2). However, when this relationship is tested on flux changes that occur on day rather than month time scales, it is found to no longer adequately describe the data. Consequently, it appears that a different mechanism must be operating to produce TeV gamma-ray rate changes on these shorter time scales.

Recent work on constraining the EBL, both theoretical and observational, have indicated that it is less intense than previously thought (58; 59). Comparing the observed spectrum of Markarian 421 with that of a pure power law convolved with the theoretical absorption from the EBL show that it is not dense enough to explain the observed cutoff (section 4.5.3). It therefore seems that the intrinsic spectrum of Markarian 421 cannot be explained by a pure power law. One possible explanation is that there is a cutoff in the spectrum of whatever particles are responsible for the production of TeV photons. Another explanation could be some form of absorption occurring within the source itself. Although the statistics in this study are not sufficient to determine whether or not the cutoff energy in Markarian 421 changes over time, the fact that its cause is likely to be intrinsic to the source rather than a slowly varying field like the EBL indicates the possibility for the future discovery of changes on short timescales.

With the advent of the stereoscopic imaging of Čerenkov showers by experiments such as HESS and VERITAS, higher quality data on TeV blazars has been coming, and continues to come, in. These new-generation instruments may have the power to finally resolve the question of what mechanism produces TeV photons in blazars. One exciting prospect of such an understanding is the ability to use TeV blazars as cosmological tools, as has already begun with the limits that have been placed on the

EBL density. If we can understand blazar spectra well enough to predict what the intrinsic spectra should look like, then our ability to measure the cosmological effects on those spectra will increase dramatically.

APPENDIX A

FINDING THE MINIMUM BOUNDING RADIUS FOR $N > 3$ POINTS

In this appendix we sketch a proof of the conjecture made in section 3.2.4 about the bounding radius for a group of $n > 3$ points. Here, the bounding radius is defined as the smallest possible radius of a circle that can contain a set of n points. The conjecture is that *the smallest bounding radius for $n > 3$ points is the largest bounding radius for any subset of 3 points.*

We can always find a circle that contains all n points by increasing its radius to an arbitrarily large size. We then proceed to continuously decrease the radius. By moving the center of the circle continuously, it is straight forward to continue this process until two of the n points lie on this circle. Since we have three degrees of freedom to work with (the x and y coordinates of the center of the circle and its radius), and only two are required to make the circle intersect the two points, we can use the third degree of freedom to continue to decrease the radius. If there were only two points, it would be possible to keep shrinking the radius until the two points lay on the endpoints of a diameter of the circle. For $n > 2$, this process will only have to stop sooner if a third point at first comes into contact with the circle. If this does not happen, the resulting circle will be the minimum circle that bounds the obtuse triangle formed by the two points on its diameter and any of the other points in its interior. If a third point is intersected, the circle will circumscribe a triangle. We can assume that this triangle is acute, since otherwise we could continue to shrink and move the circle until the two points with the greatest distance between them lie on a diameter. Thus, all n points can be contained by the minimum bounding circle for one of the subsets of three points.

APPENDIX B

RAW DATA FOR TEV BURST SEARCH

This appendix contains the raw data for the TeV gamma-ray burst search discussed in chapter 3. The measured and expected background counts for bursts of size $n = 2$ through 7, along with the observation times, are given in the following three tables. Each table corresponds to a different camera configuration, and they are further subdivided by burst length and zenith angle (ZA). The label "low" corresponds to ZA $< 20°$, "med" corresponds to $20° \leq$ ZA $< 40°$, and "high" corresponds to ZA $\geq 40°$.

Table B.1 Raw PBH search data for Jan. 1998 - July 1999.

Δt	ZA	n:	2	3	4	5	6	7	time (s)
1s	high	meas:	71,206.0	1,546.0	17.5	1.0	0.0	0	210,368
		bkgd:	71,637.4	1,647.8	17.8	0.2	0.0	0.0	
	med	meas:	125,279.0	1,844.0	9.0	0.0	0.0	0	907,506
		bkgd:	124,876.7	1,843.4	16.8	0.1	0.0	0.0	
	low	meas:	57,319.5	629.3	5.0	0.0	0.0	0.0	827,740
		bkgd:	56,919.9	619.5	4.8	0.0	0.0	0.0	
3s	high	meas:	96,033.5	7,927.0	287.5	11.2	0.0	0.0	229,434
		bkgd:	95,892.0	7,914.0	309.2	10.4	0.5	0.0	
	med	meas:	327,922.0	15,573.6	421.0	10.0	2.7	0.0	979,603
		bkgd:	327,712.1	15,504.4	389.6	9.3	0.5	0.1	
	low	meas:	154,222.5	5,534.3	121.8	1.0	0.0	0.0	859,420
		bkgd:	153,575.7	5,418.9	98.4	1.3	0.1	0.0	
5s	high	meas:	157,555.0	22,047.3	1,288.0	41.4	1.0	0.0	186,161
		bkgd:	157,508.5	22,011.0	1,337.7	53.4	1.2	0.2	
	med	meas:	402,671.0	33,970.4	1,464.0	29.0	0.0	0.0	888,731
		bkgd:	401,604.5	33,978.1	1,408.2	45.0	0.7	0.0	
	low	meas:	213,873.0	13,541.3	464.5	7.0	0.0	0.0	836,753
		bkgd:	213,373.0	13,172.2	431.6	9.0	0.2	0.0	

Table B.2 Raw PBH search data for Sept. 1999 - July 2000.

Δt	ZA	n:	2	3	4	5	6	7	time (s)
1s	high	meas:	89,723.0	4,251.7	118.5	1.0	0.0	0.0	213,299
		bkgd:	89,901.9	4,263.4	114.0	3.8	0.1	0.0	
	med	meas:	147,176.0	5,576.3	115.8	1.0	0.0	0.0	556,517
		bkgd:	147,147.9	5,585.2	115.7	2.1	0.0	0.0	
	low	meas:	3,186.5	53.0	0.0	0.0	0.0	0	375,665
		bkgd:	3,154.2	47.7	0.5	0.0	0.0	0.0	
3s	high	meas:	146,745.5	26,292.9	2,068.0	119.0	7.2	0.0	213,305
		bkgd:	147,058.6	26,052.1	2,145.3	126.6	6.1	0.1	
	med	meas:	283,941.5	39,051.0	2,527.3	140.0	2.0	0.0	578,128
		bkgd:	284,073.3	38,887.0	2,575.0	122.3	4.3	0.1	
	low	meas:	183,511.0	23,876.3	1,573.3	70.2	3.0	0.0	385,636
		bkgd:	183,675.8	23,824.6	1,478.9	69.4	2.6	0.0	
5s	high	meas:	152,100.0	55,704.8	8,436.3	833.2	64.0	7	229,955
		bkgd:	152,084.4	55,547.4	8,475.6	849.2	66.7	4.6	
	med	meas:	303,539.0	80,858.0	9,430.3	760.2	44.5	2.0	591,445
		bkgd:	303,845.0	80,382.3	9,549.5	787.1	49.0	2.0	
	low	meas:	195,556.0	49,303.9	5,602.3	447.6	31.0	0.0	385,636
		bkgd:	195,695.7	49,291.5	5,518.8	423.2	24.8	0.9	

Table B.3 Raw PBH search data for Sept. 2000 - July 2003.

Δt	ZA	n:	2	3	4	5	6	7	time (s)
1s	high	meas:	57,281.0	1,624.7	20.3	0.0	0.0	0.0	565,257
		bkgd:	57,448.3	1,590.54	33.7	3.2	0.6	3.1	
	med	meas:	158,055.5	3,719.7	43.3	0.0	0.0	0.0	2,217,903
		bkgd:	157,784.1	3,771.3	61.6	1.7	0.0	0.1	
	low	meas:	103,795.0	2,369.7	43.5	2.0	0.0	0.0	1,812,615
		bkgd:	103,669.2	2,289.4	34.3	1.8	0.1	0.0	
3s	high	meas:	120,677.0	11,448.3	490.5	19.0	0.0	0.0	566,913
		bkgd:	120,357.6	11,484.7	574.8	24.8	1.8	0.3	
	med	meas:	344,471.5	28,143.0	1,215.5	42.8	1.0	0.0	2,234,834
		bkgd:	344,721.2	28,098.3	1,241.8	46.7	2.0	3.6	
	low	meas:	232,787.0	16,953.0	733.5	30.8	0.0	0.0	1,812,049
		bkgd:	232,185.8	17,081.9	723.1	29.5	1.1	0.1	
5s	high	meas:	139,977.5	25,094.0	2,076.0	120.8	2.2	2.1	560,263
		bkgd:	140,041.6	25,097.1	2,117.5	136.9	6.0	0.6	
	med	meas:	415,501.0	62,568.6	4,639.5	252.2	16.0	1.0	2,175,660
		bkgd:	414,630.2	62,809.7	4,723.9	278.0	17.5	1.6	
	low	meas:	289,666.5	38,844.6	2,714.5	173.8	6.5	1.0	1,780,874
		bkgd:	288,918.2	38,767.1	2,767.5	166.5	10.6	0.9	

APPENDIX C

COLLECTION AREA VERSUS ENERGY

Collection areas versus energy for the three different camera configurations calculated at various zenith angles.

Table C.1 Collection Area vs. Energy and Zenith Angle. Areas are in 10^8 cm^2.

Jan. 1998 - July 1999

Energy (TeV)	ZA $\leq 20°$	$20° <$ ZA $\leq 40°$	$40° <$ ZA
0.5	2.60 ± 0.23	0.71 ± 0.13	0.10 ± 0.06
1.0	4.80 ± 0.31	6.41 ± 0.40	1.64 ± 0.23
2.0	5.92 ± 0.35	9.10 ± 0.48	10.67 ± 0.60
5.0	4.33 ± 0.35	11.89 ± 0.65	23.01 ± 0.89
7.5	4.24 ± 0.35	11.81 ± 0.64	28.29 ± 0.98

Sept. 1999 - July 2000

Energy (TeV)	ZA $\leq 20°$	$20° <$ ZA $\leq 40°$	$40° <$ ZA
0.5	4.10 ± 0.13	4.87 ± 0.35	1.74 ± 0.46
1.0	4.72 ± 0.14	6.77 ± 0.41	9.35 ± 0.57
2.0	5.33 ± 0.15	8.56 ± 0.47	13.10 ± 0.67
5.0	6.08 ± 0.16	9.35 ± 0.49	15.91 ± 0.74
7.5	6.48 ± 0.16	10.01 ± 0.50	17.93 ± 0.78

Sept. 2000 - July 2003

Energy (TeV)	ZA $\leq 20°$	$20° <$ ZA $\leq 40°$	$40° <$ ZA
0.5	3.54 ± 0.12	3.29 ± 0.29	0.27 ± 0.10
1.0	3.85 ± 0.13	5.75 ± 0.38	6.88 ± 0.49
2.0	3.90 ± 0.13	6.79 ± 0.41	10.71 ± 0.61
5.0	3.93 ± 0.13	6.26 ± 0.40	11.91 ± 0.64
7.5	3.82 ± 0.13	6.84 ± 0.42	11.77 ± 0.63

REFERENCES

(1) T. C. Weekes et al. *Ap. J.*, 342:379, 1989.

(2) C. Fitchel. *Astronomy and Astrophysics Supplemental*, 120:23, 1996.

(3) J.M. Davies and E.S. Cotton. *Journal of Solar Energy, Science and Engineering*, 1(2):16, 1957.

(4) S.M. Bradbury et al. In *Proc. 26th Int. Cosmic-Ray Conf. (Salt Lake City)*, volume 5, 1999.

(5) M.F. Cawley et al. *Experimental Astronomy*, 1:173, 1990.

(6) A. M. Hillas. In *Proc. 19th Int. Cosmic-Ray Conf. (La Jolla).*, 1985.

(7) J. D. Beckenstein. *Phys. Rev. D*, 7:2333, 1973.

(8) S. W. Hawking. *Commun. Math. Phys.*, 25:152, 1972.

(9) S. W. Hawking. *Commun. Math. Phys.*, 43:199, 1975.

(10) S. W. Hawking. *Nature*, 248:30, 1974.

(11) F. Halzen et al. *Nature*, 353:807, 1991.

(12) J.M. Bonnet-Bidaud and G. Chardin. *Phys. Rep.*, 170:325, 1988.

(13) D. N. Page. *Phys. Rev.*, D13:198, 1976.

(14) S.A. Teukolsky and W.H. Press. *Ap. J.*, 193:443, 1974.

(15) W. Kinnersley. *J. Math. Phys.*, 10:1195, 1969.

(16) J. H. MacGibbon. *Phys. Rev. Lett.*, 76:3474, 1996.

(17) R. Hagedorn. *Nuovo Cim.*, LVIX, No. 4:1027, 1968.

(18) K. Huang and S. Weinberg. *Phys. Rev. Lett.*, 25:895, 1970.

(19) B. J. Carr and S. W. Hawking. *MNRAS*, 168:399, 1974.

(20) B. J. Carr. *Quantum Gravity*, 631:301, 2003.

(21) A. M. Beloborodov. *Ap. J.*, 618:L13, 2004.

(22) R. J. Protheroe and T. Stanev. *Phys. Rev. Lett.*, 77:3708, 1996.

(23) R. W. Lessard et al. *Astroparticle Physics*, 15:1, 2001.

(24) M. Kertzman and G. H. Sembroski. *NIM*, A343:629, 1994.

(25) V. Connaughton et al. *Astropart. Phys.*, 8:179, 1998.

(26) D. E. Alexandreas et al. *Phys. Rev. Lett.*, 71:2524, 1993.

(27) M. Amenomori et al. In *Proc. 24th Int. Cosmic-Ray Conf. (Rome)*, volume 2, 1995.

(28) A. Barrau, G. Boudoul, and L. Derome. In *Proc. 28th Int. Cosmic-Ray Conf. (Tsukuba).*, 2003.

(29) A. Barrau et al. *Phys. Lett. B*, 551:218, 2003.

(30) J. Chisholm. 2005. arXiv:astro-ph/0509141v1.

(31) F. A. Aharonian et al. *Nature*, 432:75, 2004.

(32) M. Punch et al. *Nature*, 358:477, 1992.

(33) D. Petry et al. *A&A*, 311:L13, 1996.

(34) A.J. Barth, L.C. Ho, and W.L.W. Sargent. *Astrophysical Journal*, 583:134, 2003.

(35) F.N. Owen et al. *Astrophysical Journal*, 83:685, 1978.

(36) J. Maza, P.G. Martin, and J.R.P. Angel. *Astrophysical Journal*, 224:368, 1978.

(37) R. F. Mushotzky et al. *Astrophysical Journal*, 232:L17, 1979.

(38) P. F. Michelson. *IAU Circ.*, 5470:1, 1992.

(39) R. Antonucci. *Annu. Rev. Astron. Astrophys.*, 31:473, 1993.

(40) J.A. Gaidos et al. *Nature*, 383:319, 1996.

(41) M.J. Rees. *Nature*, 211:468, 1966.

(42) B.G. Piner and P.G. Edwards. *Astrophysical Journal*, 600:115, 2004.

(43) G. Henri and L. Sauge. *astro-ph/0511610v1*, 2005.

(44) J. Buckley et al. *Astrophysical Journal*, 472:L9, 1996.

(45) M. Blazejowski et al. *Astrophysical Journal*, 630:130, 2005.

(46) F. Krennrich et al. *Astrophysical Journal*, 560:L45, 2001.

(47) F. Aharonian et al. *Astron. and Astrophys.*, 95:437, 2005.

(48) F. Krennrich et al. *Astrophysical Journal*, 575:L9, 2002.

(49) A.P. Marscher and W.K. Gear. *Astrophysical Journal*, 298:114, 1985.

(50) L. Maraschi, G. Ghisellini, and A. Celotti. *Astrophysical Journal*, 397:L5, 1992.

(51) H. Krawczynski et al. *Astrophysical Journal*, 601:151, 2004.

(52) W. Cui et al. In *Proc. International Symposium on High Energy Gamma-Ray Astronomy*, volume 745, page 455, 2004.

(53) F.A. Aharonian. *New Astronomy*, 5:377, 2000.

(54) A. Mucke et al. *Astroparticle Physics*, 18:593, 2003.

(55) P. G. Tinyakov and I. I. Tkachev. *JETP Lett.*, 74:445, 2001.

(56) V. V. Vassiliev. *Astropart. Phys.*, 12:217, 2000.

(57) M. G. Hauser and E. Dwek. *Ann. Rev. of Astron. and Astrophys.*, 39:249, 2001.

(58) J. R. Primack, J. S. Bullock, and R. S. Somerville. In *Proc. Gamma 2004 Symposium on High Energy Gamma Ray Astronomy (Heidelberg)*, 2004.

(59) F. Aharonian et al. *astro-ph/0508073v1*, 2005.

(60) G. Mohanty et al. *Astroparticle Physics*, 9:15, 1997.

(61) A. M. Hillas et al. *Astrophysical Journal*, 503:744, 1988.

(62) S. LeBohec and J. Holder. *Astropart. Phys.*, 19:221, 2003.